INFORMATION TO USERS

This manuscript has been reproduced from the microfilm master. UMI films the text directly from the original or copy submitted. Thus, some thesis and dissertation copies are in typewriter face, while others may be from any type of computer printer.

The quality of this reproduction is dependent upon the quality of the copy submitted. Broken or indistinct print, colored or poor quality illustrations and photographs, print bleedthrough, substandard margins, and improper alignment can adversely affect reproduction.

In the unlikely event that the author did not send UMI a complete manuscript and there are missing pages, these will be noted. Also, if unauthorized copyright material had to be removed, a note will indicate the deletion.

Oversize materials (e.g., maps, drawings, charts) are reproduced by sectioning the original, beginning at the upper left-hand corner and continuing from left to right in equal sections with small overlaps.

Photographs included in the original manuscript have been reproduced xerographically in this copy. Higher quality 6" x 9" black and white photographic prints are available for any photographs or illustrations appearing in this copy for an additional charge. Contact UMI directly to order.

Bell & Howell Information and Learning
300 North Zeeb Road, Ann Arbor, MI 48106-1346 USA
800-521-0600

DISSERTATION

IMPACT OF BIOMASS BURNING AEROSOLS ON THE CLEAR-SKY SHORTWAVE RADIATIVE FLUXES

Submitted by
Xiang Li
Department of Atmospheric Science

In partial fulfillment of the requirements
For the Degree of Doctor Of Philosophy
Colorado State University
Fort Collins, Colorado
Summer 2000

Bell & Howell Information and Learning Company
300 North Zeeb Road
P.O. Box 1346
Ann Arbor, MI 48106-1346

COLORADO STATE UNIVERSITY

June 15, 2000

WE HEREBY RECOMMEND THAT THE DISSERTATION PREPARED UNDER OUR SUPERVISION BY XIANG LI ENTITLED IMPACT OF BIOMASS BURNING AEROSOLS ON THE CLEAR-SKY SHORTWAVE RADIATIVE FLUXES BE ACCEPTED AS FULFILLING IN PART REQUIREMENTS FOR THE DEGREE OF DOCTOR OF PHILOSOPHY.

Committee on Graduate Work

M. R. Azimi-Sadjadi

Dan A. Randall

Co-Advisor

Ronald M Welch

Co-Advisor

S. A. Rutledge

Department Head

ABSTRACT

IMPACT OF BIOMASS BURNING AEROSOLS ON THE CLEAR-SKY SHORTWAVE RADIATIVE FLUXES

Aerosol radiative forcing is recognized as a key climate change component, and biomass burning is one of the largest sources of anthropogenic tropospheric aerosols. Biomass burning aerosols have both a direct radiative impact by scattering and absorbing solar radiation and an indirect radiative impact by serving as cloud condensation nuclei. Although our knowledge of the optical properties of smoke aerosols has been significantly improved during the past decade through field experiments, there still exists large uncertainty in both direct and indirect smoke radiative forcings at the Top-of-Atmosphere (TOA) and at the surface.

Using satellite measurements, direct shortwave radiative forcings of smoke aerosols are estimated both at the TOA and at the surface. Optical thickness (τ) and single scattering albedo (ω_0) are the two most important optical parameters of smoke aerosols in determining their radiative impact. A look-up table approach is applied to retrieve these parameters using Advanced Very High

Resolution Radiometer (AVHRR) imagery from the NOAA platform. Using NOAA-14 AVHRR visible reflectances and ground-based τ measurements, the ω_0 values of smoke aerosols are estimated for selected days during both the Smoke, Clouds and Radiation-Brazil (SCAR-B) experiment held in Brazil during 1995 and for selected days during the Zambian International Biomass Burning Emission Experiment (ZIBBEE) held in Africa in 1997. The retrieved average values of ω_0 at a wavelength of 0.64 μm range between 0.83 to 0.91, which are in good agreement with *in situ* measurements and previous studies. Using the retrieved ω_0 and observed τ values, surface downward shortwave irradiances (DSWI) are calculated over 4 sites in South America and Africa and are compared with the ground-based DSWI measurements. Comparisons show that for 10 out of 14 cases, the root mean square (RMS) errors between model calculations and observed DSWIs are within 30 Wm^{-2}, with the largest error of 51 Wm^{-2}. The results indicate that when ground-based values of aerosol τ are available, reasonable estimates of ω_0 can be retrieved from AVHRR imagery which, in turn, then can be used to characterize biomass burning aerosols in radiative transfer calculations.

The Angular Distribution Model (ADM), which is used to convert the measured solar radiances into fluxes at the TOA, is a key component to obtain accurate estimates of TOA fluxes. In this study, an ADM for smoke aerosols is calculated using a discrete ordinate radiative transfer model. Using collocated Visible and Infrared Scanner (VIRS) data and the Cloud and Earth Radiant

Energy System (CERES) scanner data from the Tropical Rainfall Measuring Mission (TRMM) platform, instantaneous TOA shortwave (SW) fluxes are estimated using the new smoke ADM and compared with the SW fluxes from the CERES product for selected days over biomass burning regions in South America in 1998. The RMS error between the CERES SW fluxes and fluxes using the smoke ADM is 13 Wm^{-2}. The new smoke ADM developed as part of this study can be used to estimate the radiative impact of biomass burning aerosols using satellite imagery.

Surface SW fluxes can be estimated from the TOA observed SW fluxes using the radiative transfer model. In this study, a δ-four stream radiative transfer model has been modified to account for the biomass burning aerosols so that it can be used over biomass burning regions. Using *in situ* measurements of aerosol optical properties and ground-based measurements of aerosol optical thicknesses during the SCAR-B experiment, surface DSWI values in the presence of biomass-burning aerosols are calculated. These DSWI values are compared with broadband pyranometer measurements made at the surface. The results show that when near-coincident measurements of ω_0 and τ are available, the root mean square errors between the measured and calculated DSWIs for daytime data are within 20 Wm^{-2}. However, when assumptions about ω_0 have to be made, the differences can be as large as 95 Wm^{-2}. The results show that τ and ω_0 are the two most important parameters that affect DSWI calculations.

Finally, one month of VIRS and CERES data in August 1998 over biomass burning regions in South America and Africa have been processed to study the instantaneous and diurnally-averaged smoke radiative forcings both at the TOA and at the surface. The smoke τ values are retrieved from the VIRS visible channel images assuming the ω_0 values of smoke aerosols. The TOA SW fluxes are calculated using the smoke ADM developed in this study, and the surface SW fluxes are calculated using the δ-four stream radiative transfer model. From the number of smoke pixels identified and from the retrieved smoke optical thicknesses, it is noted that the biomass burning season over South America is stronger than that over Africa in 1998. Analysis shows that when τ (0.64 μm) is 1.0, the direct instantaneous TOA Shortwave Aerosol Radiative Forcing (SWARF) is about –50 Wm^{-2} and the surface downward SWARF is about 210 Wm^{-2}. The TOA SWARF per τ ranges from –35 Wm^{-2} to –50 Wm^{-2}. For a τ value of 1.0 and TOA clear-sky albedo of 0.16, the diurnally-mean direct TOA SWARF ranges from –7 Wm^{-2} to –20 Wm^{-2}, and the diurnally-mean surface downward SWARF ranges from 80 Wm^{-2} to 100 Wm^{-2} for ω_0 values ranging from 0.80 to 0.90. The results from one month of data indicate that smoke aerosols have significant cooling effect at both the TOA and the surface.

Xiang Li
Department of Atmospheric Science
Colorado State University
Fort Collins, CO 80523
Summer, 2000

ACKNOWLEGEMENT

I would like to express my most sincere gratitude toward my advisors, Dr. Ronald Welch and Dr. Thomas Vonder Haar, for their patience, guidance and encouragement in my dissertation work. Appreciation is also extended to my committee members, Dr. David Randall, Dr. Thomas McKee, and Dr. Mahmood Azimi-Sadjadi. I would also like to thank Dr. Sunder Christopher for his many suggestions and help during my study.

Special thanks to Ms. Joyce Chou, for sharing programs and for some data processing. Thanks to Dr. Kwo-Sen Kuo and Todd Berendes for providing calibration programs, to Denise Berendes for keeping my machine "healthy" so that I could finish my work, and to Dr. Qingyuan Han for valuable suggestions and "questions".

My family gave me so much support towards the completion of this dissertation. To my wife, Min Wang for the deep understanding, big support and encouragement throughout my six years of study. To my daughter Grace, and son Joey, you gave me so much spiritual support. Thanks to my parents and parents-in-law, for motivating me to finish my degree.

Finally, thank God and my Lord Jesus.

This research was supported by NASA Clouds and Earth's Radiant Energy System Scientific Investigation (NAS1-98131) and NASA's Earth System Science Fellowship program (ESS/98-0000-0115).

TABLE OF CONTENTS

CHAPTER 1

INTRODUCTION

Biomass burning is considered to be one of the major sources of trace gas species and tropospheric aerosol particles (Crutzen et al. 1979). These aerosols play a significant role in atmospheric chemistry (Andreae 1991), earth radiation budget (Penner et al. 1992; Hobbs et al. 1997) and climate (IPCC 1995). Widely prevalent in the tropics, anthropogenic biomass burning has expanded drastically in the last 15 years due to increased deforestation practices in Brazil's Amazon Basin, as well as due to the clearing of land for shifting cultivation in South America, Southeast Asia and Africa (Seiler and Crutzen 1980). It is estimated that 114 Tg of smoke is released into atmosphere yearly through biomass burning, out of which 80% is in the tropical regions (Penner et al. 1992; Hao and Liu 1994).

Smoke aerosols from biomass burning can significantly modify the earth's radiation budget (Penner et al. 1992; Hobbs et al. 1997; Christopher et al. 1996). Smoke aerosols, mainly composed of organic matters and black carbon (Martins

et al. 1998), reflect and absorb solar radiation and therefore have a direct radiative effect. They also serve as cloud condensation nuclei (CCN) and have an indirect radiative effect by modulating cloud properties. The direct smoke shortwave (SW) Aerosol Radiative Forcing (SWARF) at the top-of-atmosphere (TOA), defined as the difference of TOA SW fluxes between clear sky and smoke conditions, is a measure of direct aerosol SW radiative impact due to biomass burning events. For example, a negative value of SWARF implies that less solar radiation is available at the surface, thereby producing a "cooling effect". Previous studies (Penner et al. 1992; Hobbs et al. 1997) indicate that biomass burning aerosols have cooling effect on the Earth's system.

The radiative impact of biomass burning aerosols is mainly determined by their optical properties as well as their global spatial and temporal distributions. Important parameters include the rate of biomass burning, the lifetime of smoke, the fraction of burned material that goes into smoke, the surface albedo, the fractional cloud cover, the fraction of smoke that is distributed between land and ocean, and the optical properties of aerosols, including single scattering albedo, optical depth, and extinction coefficients. Using these parameters, the direct TOA SWARF of smoke aerosols can be estimated using a simple radiative transfer equation (Penner et al. 1992; Hobbs et al. 1997). However, due to the uncertainty in smoke aerosol characteristics, the estimate of direct TOA SWARF for smoke aerosols is uncertain. Estimated global-mean values of TOA SWARF due to biomass burning aerosols are -0.8 Wm^{-2} (Penner et al. 1992) and -0.3

Wm^{-2} (Hobbs et al. 1997), respectively. The TOA SWARF difference between the Penner et al. (1992) and Hobbs et al. (1997) estimates is the result of assuming different values of the scattering and absorption efficiencies and the humidification factor of biomass burning aerosols.

Over biomass burning regions, smoke aerosols are absorptive in the shortwave part of the electro-magnetic spectrum, where optical thickness (τ) and single scattering albedo (ω_0) are the two most important optical parameters in affecting the radiative balance (Lenoble 1991). Aerosol optical properties can be obtained from *in situ* measurements (Reid et al. 1998a,b), retrieved from ground-based measurements (Holben et al. 1996; Eck et al. 1998), and retrieved from spaceborne measurements (Chu et al. 1998; Liousse et al. 1997). Although the *in situ* and ground-based measurements are necessary to validate and carefully study the radiative effects of aerosols, satellite remote sensing of aerosol optical properties is the key for obtaining global estimates of aerosol distribution and aerosol radiative forcing. Due to the uncertainty of surface albedos caused by non-uniform land surfaces, most of the retrievals of aerosol optical thickness and single scattering albedo using visible channel of satellite observations have been limited to ocean and dark land surfaces (Husar et al. 1997; Stowe and Ignatov 1997; Kaufman and Sendra 1988). Global distributions of UV-absorbing aerosols also are obtained using measured differences between the 340 nm and the 380 nm radiances from the Nimbus 7 Total Ozone Mapping Spectrometer (TOMS) (Herman et al. 1997; Hsu et al. 1996).

Satellite measurements provide a more straightforward approach for estimating regional and global TOA SWARF values for smoke aerosols. Using the combination of Advanced Very High Resolution Radiometer (AVHRR) and Earth Radiation Budget Experiment (ERBE) (Barkstrom, 1984) measurements, the instantaneous direct TOA SWARFs for smoke aerosols were estimated over South America by Christopher et al. (1996, 1998). The instantaneous SWARF values can be as high as $-70\ Wm^{-2}$, depending on the aerosol concentrations.

Measurements from the ERBE instruments on board NOAA polar-orbiting satellites and from the Earth Radiation Budget Satellite (ERBS) have provided important data sets for understanding the Earth Radiation Budget. This effort of measuring TOA radiative fluxes continues through the subsequent Cloud and Earth's Radiant Energy System (CERES) instruments on board the Tropical Rainfall Measuring Mission (TRMM) platform and the recently launched Earth Observing System (EOS) Terra satellite. In both the ERBE and the CERES scanner products, broadband shortwave (SW) (0.2 – 5.0 μm) and longwave (LW) (5.0 – 50 μm) radiances were measured by the scanners. The measured radiances then were converted to SW and LW fluxes using Angular Distribution Models (ADM), which relate the TOA radiances at a specific solar and observing geometry to the TOA fluxes under various surface and atmospheric conditions. There are a total of 12 ERBE ADMs, derived by combining 5 surface types (ocean, land, snow, desert, mixed, or coastal) with 4 cloud conditions (clear,

partly cloudy, mostly cloudy, and overcast) (Green 1987). Although the TOA radiances were accurately measured with careful calibration procedures, the accuracy of ERBE TOA fluxes were affected by the accuracy of ERBE ADMs, as well as the scene identification, which determines the proper ERBE ADM to be used. Suttles et al. (1992) showed that the estimated SW albedo systematically increases with increasing viewing zenith angle, and LW fluxes decrease with increasing viewing zenith angle due to limitations in the ERBE ADM. The limited number of ERBE ADMs also limits the accuracy of converted ERBE fluxes. To overcome these problems, the CERES team is developing a new generation of CERES ADMs (Green et al. 1995). It is expected that increased accuracy of CERES cloud property determination and the new ADMs can reduce the uncertainty in the flux conversion by a factor of 3 to 4 (Wielicki et al. 1995). However, note that in both the ERBE and the CERES projects, the angular distribution model for smoke is not available. Lacking proper scene categories, smoke aerosols are usually classified as either clear or partly cloudy in the ERBE and CERES products. Due to strong absorption of smoke aerosols on solar radiation and differences in particle size distributions between clouds and smoke, the ADMs for clouds and smoke could be significantly different. This may cause uncertainties in the estimation of TOA SW fluxes over biomass burning regions in the ERBE and the CERES products. The development of an ADM for smoke aerosols may improve the accuracy of CERES SW fluxes over biomass burning regions.

While the TOA radiative energy fluxes are important climatic variables, equally important are the downward surface fluxes which drive the surface energy balance. The surface radiative fluxes either can be measured by the instruments on the surface (Gilgen et al. 1993), or estimated from the satellite measurements using radiative transfer theory (Pinker and Laszlo 1992; Whitlock et al. 1993; Zhang and Rossow 1995; Charlock and Alberta 1996). Although surface observations can provide accurate estimates of the surface fluxes, global estimates of surface radiative fluxes can only be obtained through satellite measurements. The solar radiation interacts with clouds, aerosols, and molecules before reaching the earth. It is typical to use radiative transfer models (Pinker and Laszlo 1992; Zhang and Rossow 1995) or model-derived relationships between the TOA and surface SW fluxes (Li et al 1993) to estimate the Solar Surface Radiation Budget (SSRB) from satellite observations. In general, the satellite-estimated global surface SW radiation budget is in reasonably good agreement with the observed surface radiation budget, with the root-mean-square (RMS) errors of monthly mean surface insolation being within 30 Wm^{-2} (Li et al. 1995); this RMS error may be reduced to about 5 Wm^{-2} if the number of surface observations is increased (Li et al. 1995). However, large discrepancies of up to 30 Wm^{-2} for zonal means of monthly average surface insolation exist over regions where absorbing aerosols (i.e. biomass burning aerosols) are present (Li 1998). Comparisons of monthly-mean downward surface SW irradiances from the Global Energy and Water cycle Experiment (GEWEX) Surface Radiation Budget (SRB) satellite-derived data product with

monthly-mean ground-based measurements of downward surface SW irradiances show significant differences of 40-80 Wm^{-2} over equatorial Africa where extensive savanna fires take place (Konzelmann et al. 1996). On the global average, the difference is within 20 Wm^{-2} (Whitlock et al. 1993). These large differences are probably due to the improper treatment of the aerosol radiative parameters in model radiative transfer calculations. The aerosols in the GEWEX SRB SW radiative transfer model (Pinker and Laszlo, 1992) are assumed to be either marine or continental types. The reason that biomass burning aerosols have not been properly considered in the models is that little information has been available concerning their optical properties. A better treatment of the absorbing aerosols in the radiative transfer models is key to the improvement of the SSRB estimation over biomass burning regions.

The knowledge of biomass burning events and optical properties of biomass burning aerosols has been improved gradually through a number of intensive field experiments, including the Biomass Burning Airborne and Spaceborne Experiment-Amazon and Brazil (BASE-A and –B) (Kaufman et al. 1992; Ward et al. 1991) and the Smoke, Cloud and Radiation-Brazil (SCAR-B) (Kaufman et al. 1998). One goal of the SCAR-B experiment was to measure and understand the biomass burning aerosols and their microphysical and optical properties (Kaufman et al. 1998). From the SCAR-B experiment, it was found that the smoke particles, within an hour of release from biomass burning in Brazil, can be treated as spherical for estimating the physical and optical

properties (Martin et al. 1998). The particle size distributions are bimodal (the dominant accumulation mode and coarse mode) and can be represented as two lognormals with volume radius of accumulation mode of 0.13±0.02 μm (Remer et al. 1998). The smoke aerosols are mainly composed of black carbon and organic matters (Reid et al. 1998a), and most of the ω_0 values at 0.55 μm obtained from the *in situ* measurements from the University of Washington (UW) C131-A aircraft range between 0.8 and 0.9 (Reid et al. 1998b). The aerosol optical thicknesses are obtained from the surface Sunphotometer measurements (Holben et al. 1996). The smoke aerosols are hygroscopic with the ratio of the light-scattering coefficient at a Relative Humidity (RH) of 80% to that at an RH of 30% ranged from 1.01 to 1.51, with an average value of 1.16 (Kotchenruther and Hobbs 1998). From the UW 131-A measurements, the wavelength-dependent aerosol optical properties (extinction coefficient σ_e, ω_0 and asymmetry factor g) are derived using Mie theory, assuming smoke aerosols as black carbon cores covered by organic shells (Ross et al 1998). Through these results, improved understanding of the radiative impact of biomass burning aerosols is expected.

The main objective of this research is to study the radiative impact of biomass burning aerosols and, in particular, to estimate the instantaneous aerosol shortwave radiative forcings at both the TOA and at surface using satellite measurements. Identifying the smoke pixels from satellite images is the first step to achieve this goal. A simple thresholding smoke detection algorithm is developed in this study to separate smoke pixels from clear-sky pixels and

cloud pixels in satellite images. A table look-up approach is developed to retrieve the aerosol optical properties (τ and ω_0) of the detected smoke pixels from AVHRR and Visible and Infrared Scanner (VIRS) images. These are the key parameters in estimating the SW radiative fluxes, especially at the surface over a biomass burning region. Using the optical properties obtained during SCAR-B, the angular distribution model for smoke aerosols is calculated using a discrete-ordinate radiative transfer model. The ADM is a function of τ and ω_0 of smoke aerosols, surface albedo, and sun-satellite viewing geometry and is used to convert the measured TOA SW radiances by CERES scanner on the TRMM platform into TOA SW fluxes which are used to estimate the TOA SWARF of smoke aerosols. To my knowledge, this is one of the first attempts to estimate the ADM for smoke aerosols. A δ-four stream radiative transfer model (Fu and Liou 1993), used by the CERES Surface and Atmospheric Radiation Budget (SARB) team to calculate the surface and atmospheric radiative fluxes, is modified in this study to account for the effect of smoke aerosols in the shortwave radiative transfer. The modified δ-four stream model is extensively used in the estimation of surface SW fluxes and surface aerosol radiative forcing. Finally, the radiative impact of smoke aerosols at both the TOA and at surface is investigated for the 1998 burning season over both South America and Africa by collocating the CERES and VIRS data sets from the TRMM platform. For the collocated smoke samples, τ values are retrieved using VIRS channel 1 albedos assuming a typical ω_0 value for smoke aerosols obtained during SCAR-B. The TOA SW fluxes are obtained from the measured CERES

SW radiances using the smoke ADM. The surface SW fluxes also are calculated using the δ-four stream model. With these data sets, the SWARF of smoke aerosols at both the TOA and at surface is estimated. Figure A.1 in Appendix A shows a schematic diagram illustrating the objectives for and models used in this study.

In chapter 2, the data sets used in this study are introduced, including both satellite measurements and surface measurements. Chapter 3 introduces the two radiative transfer models used in this study: the SBDART model and δ-four stream model. The methodology applied in this study is presented in Chapter 4, including smoke detection from VIRS channels, satellite retrieval of optical properties for smoke aerosols, estimation of the angular distribution model for smoke aerosols, and modification of δ-four stream model. Chapter 5 presents the results and discussions in this study. Chapter 6 presents the conclusions and summary of this study, and chapter 7 presents potential future work.

CHAPTER 2

DATA

This dissertation work utilizes data sets both from satellite measurements and from surface and aircraft measurements. The satellite data sets include the Advanced Very High Resolution Radiometer (AVHRR), the Visible and Infrared Scanner (VIRS) and the Cloud and Earth Radiant Energy System (CERES) data. The surface and aircraft data sets include aerosol microphysical properties obtained from the measurements from several instruments on board the University of Washington Convair 131-A (UW C-131A) research aircraft, aerosol optical thicknesses from ground-based sunphotometer measurements, and Downward Shortwave Irradiance (DSWI) measurements from broadband Eppley pyranometers at the surface. All of the three surface data sets are obtained during SCAR-B. The data products from the Atmospheric Radiation Measurement (ARM) project are also used to validate a broadband radiative transfer model. Descriptions of these data sets are presented in the following subsections.

2.1 NOAA-14 AVHRR LAC data

The AVHRR data are obtained from the sensors mounted on the National Oceanic and Atmospheric Administration (NOAA) series operational polar orbiting satellites. The satellite data used in this study are the AVHRR Local Area Coverage (LAC) data from the NOAA-14 satellite. The AVHRR sensor is a scanning radiometer which provides measurements at five visible and infrared channels. The spatial resolution of AVHRR LAC data is about 1.1 km at nadir. Channel 1 is the visible channel at 0.58-0.68 μm. Channels 2 and 3 are the near-infrared channels at 0.72-1.1 μm and 3.5-3.9 μm, respectively, and channels 4 and 5 are the thermal infrared channels at 10.5-11.5 μm and 11.5-12.5 μm, respectively.

The digital counts measured by the channel 1 and channel 2 sensors have been converted into TOA albedos through calibration procedures (Kidwell 1998). However, the calibration coefficients need to be recomputed due to sensor degradation (Rao and Chen 1996, 1999) because the variability of calibration coefficients causes uncertainty in the computed albedos. It has been estimated that, due to sensor degradation, the uncertainty of NOAA 11 AVHRR channel 1 albedoes is on the order of ±8% (Liousse et al. 1997). In this study, the degradation in AVHRR channel 1 is accounted for as outlined in Rao and Chen (1999).

A total of 52 AVHRR (NOAA-14) LAC images have been processed from August 15 to September 17 in 1995 over South America along with a total of 20 AVHRR LAC images from August 20 to September 10 in 1997 over Africa. These data were used to retrieve the single scattering albedo of smoke aerosols over the sites where the sunphotometers were located. The AVHRR data are collocated with the sunphotometer measurements. For a collocated sample, the time difference between the AVHRR measurement and the sunphotometer measurement is less than 15 minutes, and the spatial difference between the satellite observation and the sunphotometer measurement is less than 0.02° in latitude and longitude. The results of this study are shown in Chapter 5.

2.2 Level 1B VIRS data

The VIRS sensor is a scanning radiometer aboard the TRMM platform. The VIRS measures reflected solar and emitted terrestrial radiation in five spectral channels. The central wavelengths of the five channels are 0.63, 1.61, 3.75, 10.8, and 12.0 μm, respectively, with spatial resolution of 2.11 km at nadir (Kummerow et al. 1998). In this study, version 4 of the VIRS Level 1B data product is used. The Level 1B data set contains calibrated radiances measured from the five channels of the instrument. The channel 1 and 2 radiances are converted to albedos, and the channel 3, 4 and 5 radiances are converted to brightness temperatures. Since the measured radiances in the 3.75 μm channel

contain contributions from both solar and thermal components, a sixth channel (channel 3 reflectance) is created by removing the thermal emission part using the 10.8 channel μm channel information (Kaufman and Nakajima 1993). The VIRS radiometer is calibrated using ground testing and in-flight data. In-flight calibration of channels 1 and 2 is accomplished via an onboard solar diffuser and by using the moon as a calibration source (Keiffer and Wildey 1996), and calibration of channels 3, 4 and 5 is accomplished via an onboard blackbody and a space view (Kummerow et al. 1998).

In this study, one month of VIRS data in August 1998 over South America and Africa have been used to estimate radiative forcings of smoke aerosols at both the TOA and at the surface over South America and Africa. The results are shown in Chapter 5.

2.3 CERES ES8 ERBE-like data

The CERES scanner on the TRMM platform is a broadband instrument (Wielicki et al., 1996) that measures the total (0.3 – 50 μm), SW (0.3 – 5.0 μm) and LW (5.0 – 50.0 μm) radiances. The spatial resolution of a CERES footprint is about 10 km at nadir. The measured radiances are converted to fluxes using ADMs (Suttles et al. 1988, 1989) developed as part of the ERBE project; the fluxes are called the CERES ES-8 ERBE-like product. In this study, the Level-2

CERES ES-8 ERBE-like data set is used. The CERES scanner has two scanning modes: the normal cross-track scanning mode, and the rotational scanning mode. In this study, only CERES ES8 ERBE-like data from the cross-track scanning mode are used.

2.4 Data set from collocation of VIRS and CERES

The VIRS data product includes measurements at five narrow spectral channels with a spatial resolution of about 2 km at nadir. It can be used to identify smoke pixels and to retrieve optical properties of smoke aerosols. On the other hand, the CERES data product provides TOA radiative fluxes at a reduced spatial resolution. The two data sets are collocated. In this study, for a VIRS pixel and a CERES footprint to be considered collocated, the geographical difference between the VIRS pixel and the center of the CERES footprint must be less than 0.02°, similar to the procedure used by Li and Leighton (1991). Both the spatial resolution of a CERES footprint and the spatial resolution of a VIRS pixel change with scanning angle. For example, at nadir, the spatial resolution of a CERES footprint is 8 km in the across-track and 16 km in the along-track direction; at a scan angle of 63° towards the edge of the swath, the spatial resolution increases to 116 km and 16 km in the across and along direction, respectively (Green et al. 1995). The collocation procedure accounts for the

change of the CERES and VIRS pixel sizes with scanning angle. The collocated samples with viewing zenith angle of less than 60° are used.

2.5 Aerosol optical thickness from sunphotometer measurements

Total column smoke optical thicknesses (τ) have been estimated by Holben et al (1996) for SCAR-B using the measured direct sun measurements from the automated ground-based sun-sky scanning spectral radiometer (sunphotometer) at several sites. Direct sun measurements were made at 340, 380, 440, 500, 670, 870, and 1020 nm, and these data were converted to τ and Angstrom wavelength exponent (α), and measurements at 940 nm were inverted to precipitable water (*PW*) (Holben et al. 1998). Definitions of aerosol optical thickness and single-scattering albedo (ω_0) are given in Appendix B. The τ values were carefully checked for cloud contamination by removing all values of the wavelength exponent which were below 1 (since cirrus clouds commonly have values ranging between 0-0.5). An additional check was made by examining the temporal variability of τ. An average of three observations (triplet) was made at 30-second intervals, which are then converted to 15-minute averages. For each observation a triplet percentage variation was first computed. Assuming that the variability of clouds is larger than those of aerosols, all data with a variability of >2% was eliminated (Holben et al. 1996).

2.6 University of Washington (UW) C-131A *in situ* measurements

During SCAR-B, the UW C-131A research aircraft made twenty-nine flights in Brazil (~90 flight hours), and a wide variety of data were collected (Hobbs 1996). Of particular importance to this study are 1) vertical profiles of temperature and water vapor, 2) derived values of the single-scattering albedo (ω_0), and 3) vertical profiles of light-scattering and light-absorption coefficients of smoke aerosols. These vertical profiles were used to parameterize the characteristics of smoke aerosols in a radiative transfer model. The light-scattering coefficient was measured with a three-wavelength (λ=450, 550, and 700 nm) integrating nephelometer, and the light absorption coefficient was measured at a wavelength of 550 nm (Reid et al. 1998a) using two methods. Teflon filters were exposed to measured volumes of ambient air and the results were analyzed using the Integrating Plate Method. In the second technique, ambient air was pumped through a filter, and the attenuation of light was measured with a Particle and Soot Absorption Photometer (PSAP). The measured light scattering was further corrected to the ambient relative humidity (Kotchenruther and Hobbs 1998). The ratio of the light scattering and light extinction coefficients provided single-scattering albedo values. Aerosol size distributions were measured continuously with a suite of three optical particle spectrometer probes mounted externally on the aircraft. The smoke particles were approximated as spheres (Martins et al. 1998) consisting of a refractory,

absorbing core of black carbon surrounded by a non-absorbing shell of unspecified organic compounds and sulfates (Ross et al. 1998). Using Mie calculations, the measured particle size distributions and estimates of the bulk chemical composition were used to obtain the mass concentrations of particles and their scattering and absorption coefficients (Reid et al. 1998a). These values were then compared to the direct measurements made simultaneously on board the aircraft using the filters, integrating nephelometer, and absorption photometer. The calculated light scattering and mass concentrations were within 20% of the directly measured values. Further details of the techniques can be found in Reid et al (1998a) and Kotchenruther and Hobbs (1998).

2.7 Eppley Pyranometer measurements

Precision Spectral Pyranometer (PSP) instruments were used in SCAR-B to measure the incident total (direct plus diffuse) irradiance on a horizontal surface on the ground (Eck et al. 1998). These instruments measured the downward shortwave irradiances (DSWI) between 0.28 to 2.8 μm. The Eppley Laboratory calibrated the instruments which were within ±1 % of the World Radiation Reference. In addition, two PSP pyranometers operated side by side on the roof of the Instituto Nacional de Pesquisas Espacias (INPE) laboratory in Cuiaba, Brazil for 5 h (sampled at 1-min intervals) on August 27, 1995. The

DSWI values measured by these two instruments in this time period agreed with each other to within 1.3%.

During SCAR-B, the temporal variability of the measurements was taken at 1 minute or 5 minute intervals, depending upon the location. High frequency temporal variation, or decreasing (increasing) irradiance with decreasing (increasing) solar zenith angle, was identified as being due to clouds. During this time, the incident Photosynthetically Active Radiation (PAR) between 0.4-0.7 μm also was measured. Since the ratio of PAR to total irradiance is influenced by the presence of both aerosols and clouds, cloud contamination was detectable by evaluating the time series of the PAR to total irradiance ratio. Higher values of the ratio represent cloud conditions due to absorption by water vapor in the near infrared, and lower values of the ratio represents high aerosol loading due to higher aerosol optical depths at shorter wavelengths (Pinker and Laszlo 1992a). A third test for cloud contamination was made by examining the wavelength variation of the aerosol optical thickness. For biomass burning aerosols in Brazil, the Angstrom wavelength exponent typically varies from 1.6 to 2.0, with values lower than 1.6 resulting from cloud contamination due to the large size of water droplets and ice crystals in clouds (Holben et al. 1996). When all three of these cloud-screening tests were passed for at least a 1-h interval, the data were identified as being cloud free. Further details can be found in Eck et al. (1998).

2.8 Surface and satellite measurements from the ARM project

The ARM project, supported by the U.S. Department of Energy (DOE), is one of the largest global change research programs. It focuses on obtaining field measurements and developing models to better understand the processes that control solar and thermal radiative transfer in the atmosphere and at the earth's surface (URL http:/www.arm.gov). More than 400 million measurements of radiation and other meteorological parameters from several dozen types of instruments are generated in the ARM project and are available to scientists.

There are three field experiment sites in the ARM project. In this study, the data products from the South Great Plains (SGP) Cloud and Radiation Testbeds (CART) site were used. Two data products were used in this study. The first one is the sgpswaradC1 product, which provided "best estimate" shortwave radiation data products derived from the surface instrument measurements, including broadband surface albedo, surface spectral albedos, broadband downward solar flux, net surface solar flux, solar zenith angle, etc. The temporal resolution for this data product is one minute. The second data product used was the sgpmwrprofC1 product, including the retrieved atmospheric temperature, pressure, and water vapor profiles, which were derived from the

satellite microwave measurements. The temporal resolution for this data product is one hour.

These data products, combined with the sunphotometer measurements over ARM CART site in April and May 1998, were used in the validation of a δ-four stream radiative transfer model under clear-sky conditions, as will be discussed in Chapter 3.

CHAPTER 3

RADIATIVE TRANSFER MODELS

In this study, two radiative transfer models, the Santa Barbara Discrete Ordinate (DISORT) Atmospheric Radiative Transfer (SBDART) model and the δ-four stream broadband model, were used in the retrieval of optical properties of smoke aerosols, in the estimation of angular distribution models for smoke aerosols, and in the estimation of surface SW radiative fluxes over biomass burning regions. These two models have been extensively used in the atmospheric radiative transfer calculations. The following sections briefly introduce the two radiative transfer models. The surface downward SW irradiances (DSWI) under clear-sky conditions are calculated using the two models and the results are compared. This serves as a cross validation for the two models. Using the ARM data products over SGP CART site located in Oklahoma and Kansas, the surface DSWIs are estimated using the δ-four stream model and are compared with the measured surface fluxes at the site. The results from model calculations are in good agreement with the surface observations.

3.1 SBDART model

The SBDART algorithm(Ricchiazzi et al. 1998) is a plane-parallel radiative transfer code based on the discrete ordinate radiative transfer code of Stamnes et al. (1988) and the LOWTRAN 7 gaseous transmission model (Pierluissi and Marogoudakis 1986). It can be used to simulate plane-parallel radiative transfer in clear and cloudy conditions within the earth's atmosphere and is designed to solve a wide variety of radiative transfer problems encountered in satellite remote sensing and earth radiation budget studies (Ricchiazzi et al. 1998). This model has been used to study the surface solar radiation flux and cloud radiative forcing (Gautier and Landsfeld 1997) and to estimate cloud optical thicknesses and surface albedos over Antarctica (Ricchiazzi and Gautier 1995).

The major radiative transfer components, including Rayleigh scattering, gaseous absorption, cloud and aerosol scattering and absorption, are included in the SBDART model. Molecular absorption is based on the low resolution band models developed for the LOWTRAN 7 atmospheric transmission code (Pierluissi and Marogoudakis 1986). In order to use gases transmission functions in the DISORT scheme, the band models are approximated with a three-term exponential fit (Wiscombe and Evans 1977). The scattering effect of cloud droplets is parameterized with the results from Mie calculations assuming spherical cloud droplets having a log-normal size distribution and an effective radii (r_{eff}) in the range of 2 to 128 μm; the scattering effect of ice clouds is

parameterized as the spherical ice grains of a fixed size distribution with r_{eff} of 106 μm (Ricchiazzi et al. 1998). The radiative effect of several boundary layer and upper level atmosphere aerosol types are contained in the SBDART. Users can select rural, urban, or maritime aerosols at the boundary layer and fresh and aged volcanic, meteoric and tropical background aerosols in the upper atmosphere (Ricchiazzi et al. 1998). The SBDART also allows the user to define an aerosol type by specifying the wavelength dependent aerosol optical properties, including optical thickness, single scattering albedo and asymmetry factor. In this study, the smoke aerosol type is defined in the SBDART model using optical properties obtained during SCAR-B.

In the SBDART model, six basic surface types -- ocean water, lake water, clear water, vegetation, snow and sand -- are used to parameterize the spectral reflectivity of the surface (Ricchiazzi et al. 1998). The spectral reflectivity of a large variety of surface conditions can be well approximated with the combination of these basic surface types. The user can also specify the surface reflectivity. Currently, the SBDART model assumes that surfaces reflect radiation isotropically. Six standard atmospheric profiles, the tropical, mid-latitude summer, mid-latitude winter, sub-arctic summer, sub-arctic winter, and US62 (McClatchey et al 1972), are adopted in the SBDART model. Users can use a specific atmospheric profile. More detailed description of the SBDART model is given by Ricchiazzi et al. (1998).

3.2 δ-four stream model

The δ-four stream model (Fu and Liou 1993) is a broadband plane-parallel radiative transfer model that can be used to calculate fluxes at the TOA, at the surface, and in the atmosphere. In this model, gaseous absorption and emission are treated using the correlated-*k* distribution technique (Fu and Liou 1992). The model accounts for the radiative effects of H_2O, CO_2, O_3, O_2, CH_4, and N_2O; Rayleigh scattering; liquid cloud droplets and hexagonal ice crystals. The cloud scattering effect is treated in both the SW spectrum and the LW spectrums. There are six spectral intervals (0.2-0.7 μm, 0.7-1.3 μm, 1.3-1.9 μm, 1.9-2.5 μm, 2.5-3.5 μm, 3.5-4.0 μm) in the SW spectrum (0.2-4.0 μm); and 12 spectral intervals in the LW spectrum (2200-1 cm^{-1}). In the radiative transfer calculations, the surface albedo is required as an input variable for each SW interval, and emissitivity is required as an input variable for each LW interval. Continuum absorption of H_2O at 280-1250 cm^{-1} (Roberts et al. 1976) is included in the model. For the principal atmospheric gases, this model matches a line-by-line simulation of fluxes to within 0.05% for SW; 0.2% for LW, excepting O_3; and about 2% for LW flux due to O_3. The amount of CO_2, CH_4 and N_2O are fixed to be 330, 1.6 and 0.28 ppmv, respectively (Charlock and Alberta 1996). The δ-four stream model agrees with adding-doubling calculations to within 5% for flux calculations and is a considerable improvement over a two-stream model (Liou et al. 1988).

The δ-four stream model was used to estimate the SW and LW radiation budget at both the TOA and at the surface over the ARM CART site. Comparisons of model estimated SW fluxes with surface fluxes indicate that the model underestimates atmospheric absorption and overestimates surface insolation (Charlock and Alberta 1996). The biases of surface downward SW fluxes are 33 Wm^{-2} and 46 Wm^{-2} for clear and cloudy conditions, respectively. The biases for the atmospheric absorption are -33 Wm^{-2} and -55 Wm^{-2} for clear and cloudy conditions, respectively (Charlock and Alberta 1996). Using the δ-four stream model, the radiative forcing of dust aerosols and its sensitivity to key variables was investigated (Liao and Senifeld 1998). Although some aerosol types are characterized in this model, to our knowledge the smoke aerosols have not been characterized. Therefore, this model is not suitable to estimate the TOA and surface radiation budgets over biomass burning regions. Modifying this model to incorporate the radiative effect of smoke aerosols is one of the key areas in this study.

3.3 Comparison of SBDART and δ-four stream model

Under clear-sky conditions, the surface downward SW irradiances are calculated using both the SBDART and the δ-four stream models and the results are compared. This comparison serves as a cross validation of the two radiative transfer models. Through the comparison, the discrepancy of the two models in

the simulation of atmospheric radiative transfer can be obtained, although the absolute accuracies of both the models are still not known.

Since the δ-four stream model outputs the SW fluxes only for the six spectral intervals described in Section 3.2, for the sake of comparison the TOA and surface SW fluxes are also calculated for these six bands using the SBDART model. The TOA and surface SW fluxes are calculated at nadir for solar zenith angles of 0° and 60°, with broadband surface albedo of 0.05 in all six spectral bands. The standard tropical profiles (McClatchey et al. 1972) are assumed. The equivalent incoming solar irradiances at the TOA for the six SW bands have been parameterized in the δ-four stream model. The TOA solar spectra required as the input in SBDART is from the LOWTRAN version 7 (Kneizys et al. 1983). The standard tropical profiles (McClatchey et al. 1972) are used in the model calculation.

Tables 3.1 and 3.2 show the results of downward and upward SW fluxes at both the TOA and at the surface for solar zenith angles of 0° and 60°, respectively. The comparison is made for each of the six SW bands and the whole solar spectral band (0.2 – 4.0 μm). Note that the SBDART actually outputs SW fluxes at 0.26-0.7 μm, corresponding to band 1 of the δ-four stream model. Due to the slight difference of the incoming solar spectra used in SBDART and in the δ-four stream model, the TOA downward solar fluxes at the six bands as well as the total solar fluxes also are slightly different. As a result, the TOA upward

Table 3.1. Comparison of the surface DSWIs under clear-sky condition using SBDART and δ-four stream model. surface albedo: 0.05, solar zenith angle: 0°, units: Wm^{-2}

Spectral interval	Model with incoming solar spectrum curve	TOA downward SW flux	TOA upward SW flux	Surface downward SW flux	Surface upward SW flux
0.2-0.7 (μm)	δ-four stream	***631.32***	***73.53***	***552.60***	***27.63***
	SBDART (curve 1)	636.27	72.84	559.42	27.97
	Scaled for curve 1	***631.32***	***72.57***	***555.07***	***27.75***
0.7-1.3 (μm)	δ-four stream	***493.43***	***21.87***	***411.79***	***20.59***
	SBDART (curve 1)	483.07	21.03	398.25	19.91
	Scaled for curve 1	***493.43***	***21.48***	***406.79***	***20.34***
1.3-1.9 (μm)	δ-four stream	***152.68***	***3.31***	***75.03***	***3.75***
	SBDART (curve 1)	153.25	3.10	71.72	3.59
	Scaled for curve 1	***152.68***	***3.09***	***71.45***	***3.58***
1.9-2.5 (μm)	δ-four stream	***49.65***	***1.47***	***34.22***	***1.71***
	SBDART (curve 1)	51.93	1.30	32.74	1.64
	Scaled for curve 1	***49.65***	***1.24***	***31.30***	***1.57***
2.5-3.5 (μm)	δ-four stream	***32.30***	***0.11***	***4.04***	***0.18***
	SBDART (curve 1)	28.57	0.06	2.55	0.13
	Scaled for curve 1	***32.30***	***0.07***	***2.88***	***0.15***
3.5-4.0 (μm)	δ-four stream	***5.91***	***0.21***	***4.97***	***0.25***
	SBDART (curve 1)	5.72	0.16	4.21	0.21
	Scaled for curve 1	***5.91***	***0.17***	***4.35***	***0.22***
0.2-4.0 (μm)	δ-four stream	***1365.29***	***99.91***	***1082.65***	***54.11***
	SBDART (curve 1)	1358.81	98.53	1072.2	53.45
	Scaled for curve 1	***1365.29***	***99.00***	***1077.3***	***53.70***

Table 3.2 Comparison of the surface DSWIs under clear-sky condition using SBDART and δ-four stream model. surface albedo: 0.05, solar zenith angle: 60°, units: Wm^{-2}

Spectral interval	Model with incoming solar spectrum curve	TOA downward SW flux	TOA upward SW flux	Surface downward SW flux	Surface upward SW flux
0.2-0.7 (μm)	δ-four stream	***631.32***	***73.53***	***552.60***	***27.63***
	SBDART (curve 1)	636.27	72.84	559.42	27.97
	Scaled for curve 1	***631.32***	***72.57***	***555.07***	***27.75***
0.7-1.3 (μm)	δ-four stream	***493.43***	***21.87***	***411.79***	***20.59***
	SBDART (curve 1)	483.07	21.03	398.25	19.91
	Scaled for curve 1	***493.43***	***21.48***	***406.79***	***20.34***
1.3-1.9 (μm)	δ-four stream	***152.68***	***3.31***	***75.03***	***3.75***
	SBDART (curve 1)	153.25	3.10	71.72	3.59
	Scaled for curve 1	***152.68***	***3.09***	***71.45***	***3.58***
1.9-2.5 (μm)	δ-four stream	***49.65***	***1.47***	***34.22***	***1.71***
	SBDART (curve 1)	51.93	1.30	32.74	1.64
	Scaled for curve 1	***49.65***	***1.24***	***31.30***	***1.57***
2.5-3.5 (μm)	δ-four stream	***32.30***	***0.11***	***4.04***	***0.18***
	SBDART (curve 1)	28.57	0.06	2.55	0.13
	Scaled for curve 1	***32.30***	***0.07***	***2.88***	***0.15***
3.5-4.0 (μm)	δ-four stream	***5.91***	***0.21***	***4.97***	***0.25***
	SBDART (curve 1)	5.72	0.16	4.21	0.21
	Scaled for curve 1	***5.91***	***0.17***	***4.35***	***0.22***
0.2-4.0 (μm)	δ-four stream	***1365.29***	***99.91***	***1082.65***	***54.11***
	SBDART (curve 1)	1358.81	98.53	1072.2	53.45
	Scaled for curve 1	***1365.29***	***99.00***	***1077.3***	***53.70***

flux and the surface downward and upward fluxes will be slightly biased. To facilitate comparisons, the TOA upward flux, surface downward and upward fluxes are scaled in the SBDART calculations so that the TOA downward solar flux equals that from the δ-four stream model.

From Table 3.1, it is seen that for 0.2-0.7 μm band and 0.7 – 1.3 μm band, the relative difference between the δ-four stream model and the SBDART using any of the incoming solar spectrum is within 1.5% for TOA upward flux, surface downward flux and surface upward flux. The solar energy within these two bands counts for 82% of the total solar energy. Over the other 4 bands, the relative difference can reach about 5%, but the available incoming solar energy is less. Including the whole solar spectrum, the relative difference is within 1% for TOA upward flux, surface downward flux and surface upward flux. This comparison indicates that the two radiative transfer models agree well with each other in the simulation of atmospheric radiative transfer processes under clear-sky conditions.

3.4 Validation of the δ-four stream model

In this study, the data products over the ARM CART site in April and May 1998 are used to validate the δ-four stream model under clear-sky conditions. Besides the two data products, the *sgpswaradC1 product* and the *sgpmwrprofC1*

product, as described in Section 2.8, and the sunphotometer measurements over the ARM CART site also are used.

The sgpmwrprofC1 data product provides vertical temperature and water vapor profiles over the site for every hour. The aerosol optical thickness derived from the sunphotometer measurement is provided every 15 minutes. The aerosol τ values used in the study are obtained after careful cloud screening procedures, as described in Section 2.5. In this study, the data samples with τ values less than 0.05 (a typical background aerosol loading) are considered as clear-sky samples and participate in the model calculations.

The surface downward SW fluxes are calculated for these clear-sky samples and compared with the observed surface downward SW fluxes provided in the sgpswaradC1 product. The sgpswaradC1 data product provides surface downward SW flux every one minute. Therefore, the surface flux measured at the time closest to that of sunphotometer measurements is compared with the model calculations.

There are a total of 17 clear-sky samples in April and a total of 77 clear-sky samples in May. Figures 3.1 and 3.2 show the observed surface downward SW fluxes versus the model-estimated surface downward SW fluxes in April and May, respectively. From Figures 3.1 and 3.2, it is seen that the δ-four stream model underestimates the atmospheric absorption, as suggested by Charlock

and Alberta (1996). However, the bias calculated here is smaller than that estimated in Charlock and Alberta (1996). The mean biases in both April and May are within 10 Wm^{-2}, as opposed to the values of 30 Wm^{-2} presented in Charlock and Alberta (1996). The Root-Mean-Square (RMS) errors are about 15 Wm^{-2} for both months.

In general, the δ-four stream model works well in the simulation of shortwave atmospheric radiative transfer.

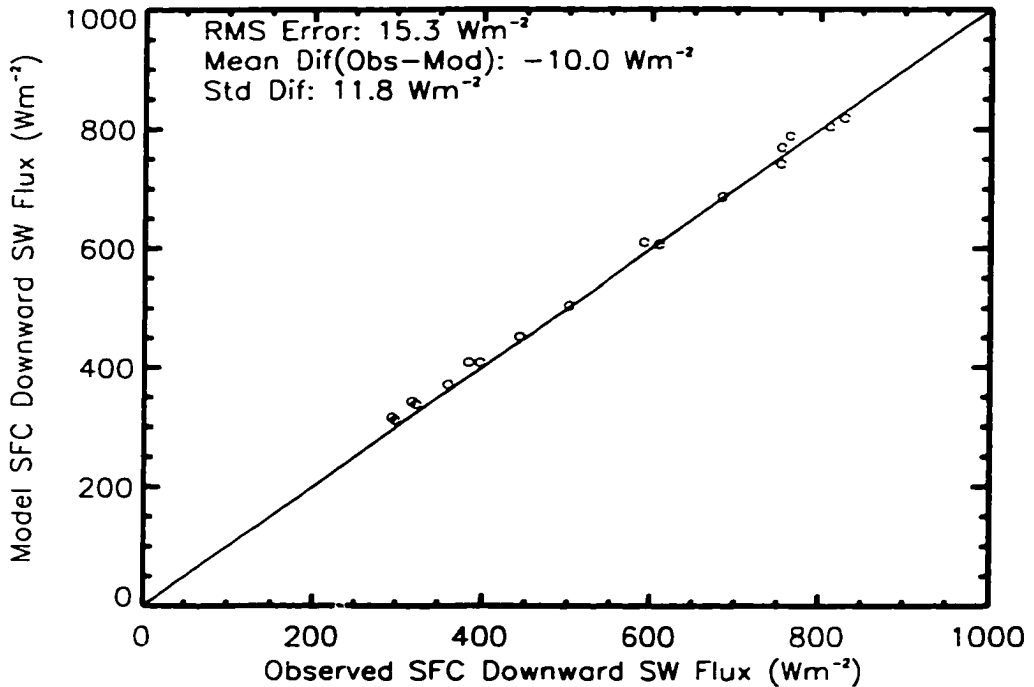

Figure 3.1 Clear−sky observed surface downward SW flux versus versus model downward SW flux in April 1998 over ARM−CART site

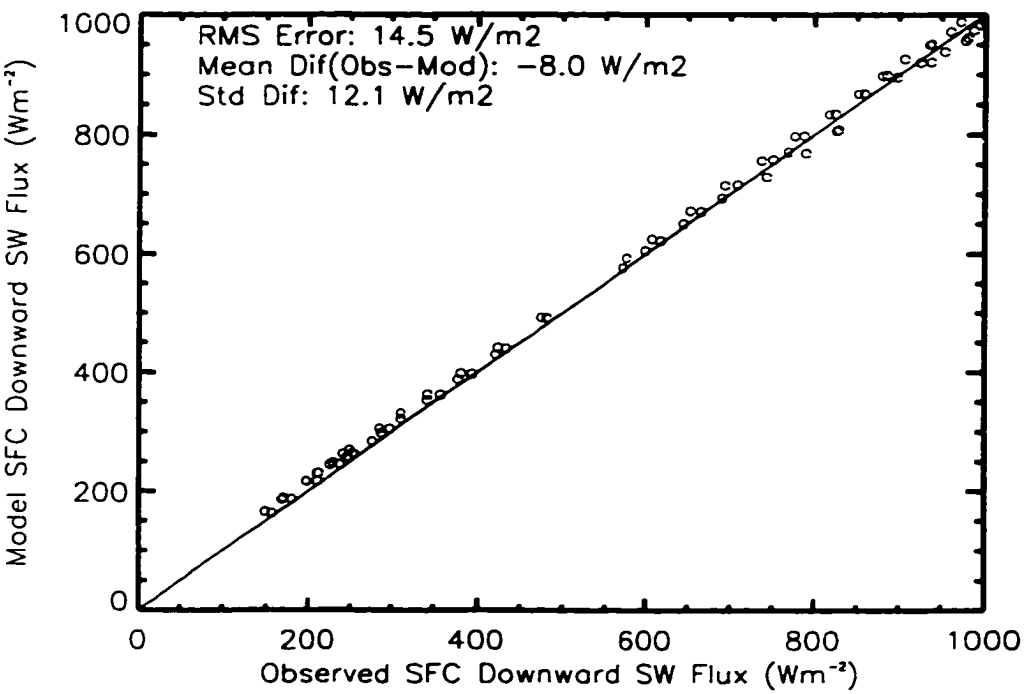

Figure 3.2 Clear−sky observed surface downward SW flux versus versus model downward SW flux in May 1998 over ARM−CART site

CHAPTER 4

METHODOLOGY

The methodology for the key issues in this study is presented in this chapter. A multi-spectral thresholding algorithm to identify smoke pixels from the VIRS images is presented in section 4.1. The detected smoke pixels from the VIRS images then are used to study the radiative impact of biomass burning aerosols over South America and Africa. A table look-up approach to retrieve aerosol optical properties using AVHRR and VIRS visible channel (channel 1) reflectance is presented in section 4.2. The optical thicknesses of detected smoke pixels from the VIRS images are retrieved using this approach. Section 4.3 presents the method to estimate the SW angular distribution model (ADM) for smoke aerosols that is necessary to convert measured CERES SW radiances into TOA SW fluxes over biomass burning regions. The global surface radiation budget is normally estimated from satellite measurements at the TOA using a radiative transfer model (Whitlock et al. 1993; Charlock and Alberta 1996). Section 4.4 presents a modified δ-four stream broadband radiative transfer model which can be used to estimate the TOA and surface SW fluxes over biomass

burning regions. Finally, the Shortwave Aerosol Radiative Forcing (SWARF) is defined in Section 4.5.

4.1 Smoke detection from VIRS imagery

Identifying smoke pixels from satellite images is the first step to estimate the radiative impact of biomass burning aerosols from satellite measurements. As is used for fire detection, the multi-spectral thresholding technique is also the common approach to detect smoke pixels from satellite images. Using data from visible channel (0.62 μm), near-infrared (3.7 μm) and thermal infrared channels (11 μm, 12 μm), an automated smoke/aerosol detection algorithm (ASADA) was developed to routinely detect the smoke from the Geostationary Operational Environmental Satellite (GOES) imagery (Prins and Menzel 1992, 1996a, b). In the ASADA algorithm, the visible channel albedo of a smoke pixel was limited to be 0.15 - 0.40 over land surfaces and 0.10 - 0.40 over ocean surfaces. For a pixel to be labeled as a smoke pixel, the temperatures in the 3.7 μm and 11 μm channels were required to be higher than 285 K, and the temperature difference between the 3.7 μm and 11 μm channels was required to be within the range of –4 to +20 K. These thresholds were set to exclude opaque clouds, cirrus and stratus clouds. To exclude low-level moisture, opaque clouds and semi-transparent cirrus, the temperature in the 12 μm channel was set to be larger than 280 K, and the temperature difference between the 11 μm and 12 μm

channels was set to be within the range of –4 to +6 K for smoke pixels. This algorithm was applied to SCAR-B and to the 1995 burning season over South America (Prins et al. 1998). A similar multi-spectral thresholding algorithm was also used in the smoke detection from AVHRR imagery (Christopher et al. 1998). Textural information from satellite images also was used to separate the dense smoke, haze, and clouds from the underlying background (Christopher et al. 1996).

In this study, a multi-spectral thresholding algorithm similar to Prins et al. (1998) and Christopher et al. (1998) was developed to detect smoke pixels from the VIRS images. A total number of 14 VIRS data files over South America were used in the development of the algorithm. Table 4.1 lists the information of the

Table 4.1. A list of VIRS data files used in the smoke detection and smoke SWARF forcing investigation

Number	Year	Month	Day	Lat (°) Min	Lat (°) Max	Long (°) Min	Long (°) Max	Start_time (GMT)	End_time (GMT)
1	1998	08	11	-23.79	-7.80	-67.26	-47.35	11.9822	12.0668
2	1998	08	11	-13.14	3.55	-50.95	-32.07	12.0669	12.1514
3	1998	08	13	-16.79	-0.23	-59.13	-40.04	11.2190	11.3036
4	1998	08	23	-15.44	1.19	-71.30	-52.31	20.1765	20.2611
5	1998	08	25	-17.38	-0.83	-71.62	-52.49	19.3722	19.4568
6	1998	08	25	-24.03	-11.92	-56.01	-41.83	19.4569	19.5110
7	1998	08	26	-15.44	1.18	-64.10	-45.12	18.1843	18.2689
8	1998	08	27	-15.44	1.18	-53.88	-34.90	17.0093	17.0939
9	1998	08	27	-19.41	-2.99	-71.65	-52.33	18.5624	18.6470
10	1998	08	27	-29.07	-13.88	-55.79	-34.91	18.6470	18.7316
11	1998	08	28	-15.45	1.17	-67.13	-48.13	17.3633	17.4478
12	1998	08	28	-25.80	-10.05	-51.69	-31.46	17.4479	17.5324
13	1998	08	29	-21.54	-5.30	-71.64	-52.06	17.7637	17.8482
14	1998	08	29	-34.38	-20.81	-69.56	-47.26	19.4142	19.4987

14 VIRS data files, including the observing date and time and geographical coverage (range of latitude and longitude). Smoke can be visually seen from the channel 1 images of these VIRS data files. Figure 4.1(a) shows an example (data file 9 in Table 4.1) of the channel 1 image of the VIRS data. In Figure 4.1(a), the lower part of the image clearly shows high cloud amounts. The middle of the upper part of the image shows clear-sky, and the middle part of the image shows smoke haze.

The thresholding algorithm identifies smoke pixels over land surfaces using the VIRS channel 1 albedo (R1), channel 2 albedo (R2), channel 3 albedo (R3), channel 4 brightness temperature (T4) and channel 5 brightness temperature (T5). A number of thresholds are used to identify a VIRS pixel as either a cloud, a smoke or a clear-sky pixel. Three VIRS data files on August 27, 1998 (data files 8, 9 and 10) are used to adjust the thresholds so that smoke pixels visually seen in these VIRS channel 1 images can be properly identified. Figure 4.2 shows the flowchart of the thresholding algorithm. First, isolated cumulus clouds are identified using a 5 x 5 window region around a VIRS pixel. If the standard deviation of channel 1 reflectance (σ_{R1}) for the pixels in the window is larger than 0.04, the window region is labeled as cloud and no further processing will be done on these pixels. A pixel with R1 larger than 0.4 and R2 larger than 0.35 is labeled as bright cloud pixel. A pixel with R1 larger than 0.35 and T4 lower than 273 K is labeled as cold cloud pixel. When R1 is larger than 0.35 and T4 is higher than 273 K, the pixel could most possibly be either low-level thick cloud or

Figure 4.1 (a) VIRS channel image of data file 9 shown in Table 4.1, (b) classification of the image into three categories: white – smoke, gray – clouds, and black – clear-sky regions.

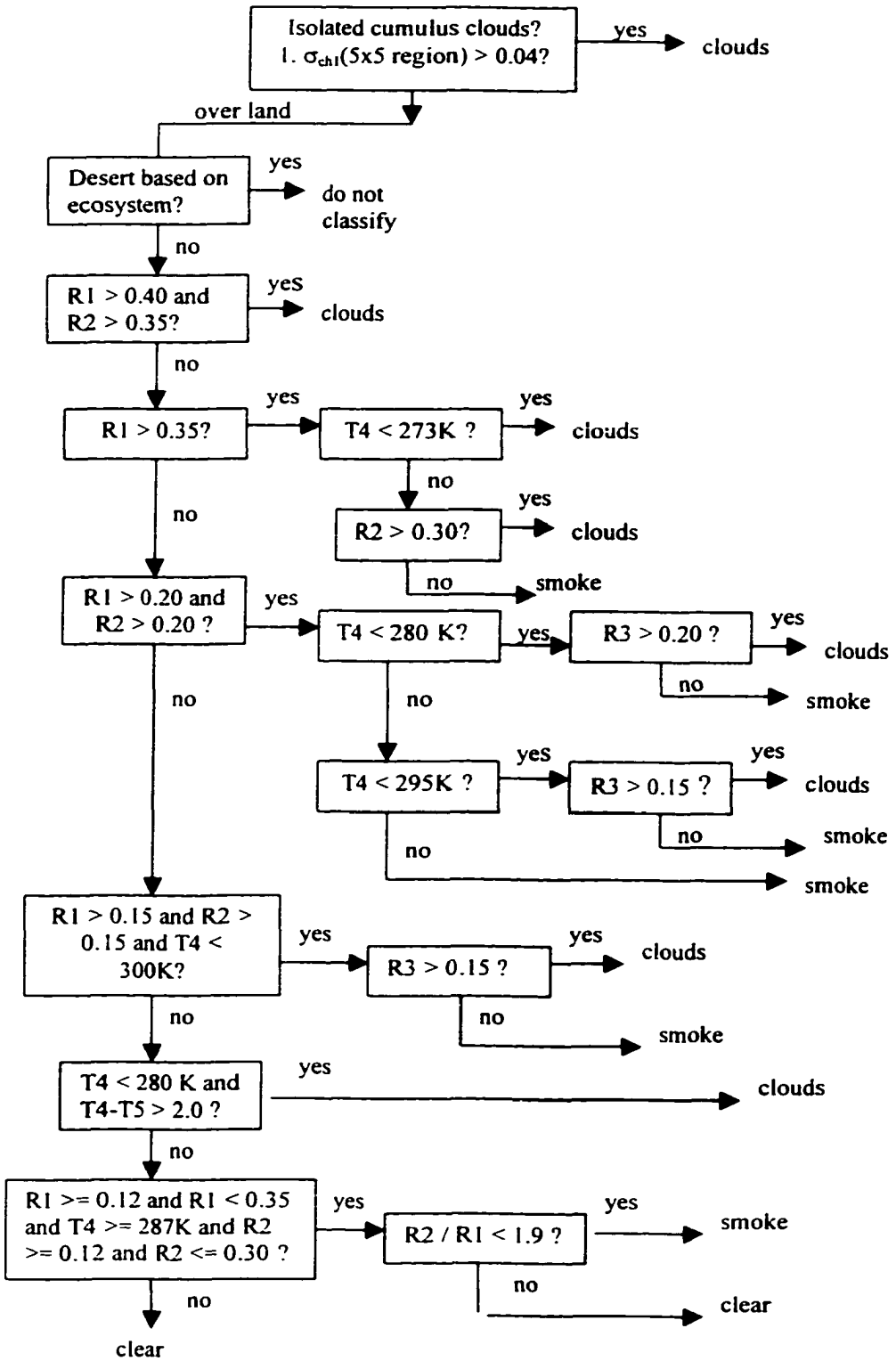

Figure 4.2 flowchart of multi-spectral thresholding technique to separate clouds, smoke and clear-sky pixels in VIRS images

dense smoke and R2 is used to separate clouds from smoke. Due to the small particle size of smoke aerosols (volume median radius of 0.15 μm), the scattering coefficient for smoke aerosols decreases rapidly with increasing wavelength in the visible and near-infrared spectrum. As a result, the smoke aerosols are less reflective than cloud particles at 1.6 μm (VIRS channel 2). When R2 is larger than 0.30, the pixel is labeled as cloud, otherwise, it is labeled as optically thick smoke. For the same reason, the channel 3 albedo (R3) is affected by the presence of clouds but less affected by the presence of smoke particles. When R1 is less than 0.35 and larger than 0.12, the pixel could most possibly be low-level and middle-level thin stratus clouds, optically thin cirrus clouds, or smoke particles which are often within the lowest 3 km of the surface. In this case, the values of R2, R3, T4 and T5 are used to separate cloudy pixels from smoke pixels. R3 values are larger for cloudy pixels than for smoke pixels and the temperature difference of T4 – T5 is used to identify optically thin cirrus clouds (Inoue 1989). For pixels with R1 values between 0.12 and 0.15, it is more difficult to distinguish between thin smoke haze and clear-sky over bright land surface such as savanna. The surface albedo for savanna in Africa is usually larger than 0.12 (Louisse et al. 1997). In this case, the ratio of R2 to R1 is used to separate smoke pixels from clear-sky pixels over land. For the vegetation surface types, surface spectral albedo at 1.6 μm (channel 2) is much higher than that at 0.64 μm (channel 1). As a result, the values of R2/R1 for vegetation are usually larger than 2.0. The existence of smoke aerosols increases channel 1 reflectance and the values of R2/R1 decrease. The smoke threshold of 1.9 for

R2/R1 is used which separates most of the clear-sky pixels from smoke pixels for the 3 images that were studied.

This smoke detection algorithm is applied to the rest of 14 VIRS data files. By visually comparing the classification results with the channel 1 images, this algorithm works well in identifying cloud, smoke and clear-sky pixels. Figure 4.1(b) shows the scene identification image corresponding to the VIRS image in Figure 4.1(a). The black color represents clear sky over land. The gray color represents clouds, and the white color represents smoke aerosols. Comparing to Figure 4.1(a), most of the smoke haze, clouds and clear sky pixels are identified.

Since the observed visible channel albedo over a smoke region is affected by the surface type (surface albedo), the visible channel thresholds should be a function of surface type. Using constant thresholds, some of the cloud, smoke and clear-sky pixels can be incorrectly identified. A more refined smoke detection algorithm and more solid validation scheme are necessary to improve the classification results but it is out of the scope of this research work. The same algorithm is also used to detect smoke pixels over Africa in the 1998 burning season.

4.2 Retrieval of optical properties of smoke aerosols

As mentioned in Chapter 1, optical thickness (τ) and single scattering albedo (ω_0) are the two most important optical properties of smoke aerosols influencing their radiative impact (Lenoble 1991; Christopher et al. 2000). Knowledge of aerosol optical properties is required in order to estimate their radiative impact both at the TOA (Penner et al. 1992; Hobbs et al. 1997) and at the surface (Christopher et al. 2000).

Liousse et al. (1997) and Chu et al. (1998) have shown that aerosol optical properties can be retrieved from satellite measurements under cloud-free conditions. In a cloud-free area, the SW radiance measured by a satellite sensor is composed of the contributions from molecular (Rayleigh) and aerosol scattering in the atmosphere and reflectance from the earth's surface. In the present study, Rayleigh scattering was specified by Penndorf's (1957) formula. The surface reflectance was characterized by the surface albedo. The aerosol scattering effect was characterized by the aerosol optical properties that include τ, ω_0 and phase function, as well as the vertical distribution of the density of aerosol particles. Aerosol optical properties were determined by their chemical compositions and their microphysical structure, such as the particle size distribution and the aerosol mixing mode.

4.2.1 Modeling for smoke aerosols

Biomass burning aerosols are mainly composed of two substances: Black Carbon (BC) and organic matter. To characterize biomass burning aerosols in radiative transfer calculations, two approaches are possible: 1) The BC and organic matter are externally mixed, thereby treated separately (Kaufman et al. 1992), or 2) the black carbon core is surrounded by the viscous organic liquid shell (Ross et al. 1998), therefore internally mixed. The derived optical properties depend upon whether the black carbon and the organic matter are internally or externally mixed. The internal mixture is more absorbing (a lower value of ω_0), with the difference depending upon the ratio of volume of soot to the total volume (Ackerman and Toon 1981). The percentage of the mass of black carbon to the total aerosol mass determines the absorption of smoke aerosols and therefore the aerosol ω_0. Biomass burning aerosols are also slightly hygroscopic (the ratio of light-scattering coefficient at a Relative Humidity (RH) of 80% to that at a RH of 30% ranging from 1.01 – 1.51), where the aerosol particle size distribution and mass composition changes with the ambient relative humidity (Kotchenruther and Hobbs 1998), also resulting in slight changes in smoke optical properties. Furthermore, the ω_0 value of smoke aerosols changes during the aging process, due to coagulation and secondary aerosol production (Reid et al. 1999).

Smoke aerosols are characterized in the radiative transfer model by 1) the aerosol extinction coefficient, 2) ω_0, and 3) either the aerosol phase function, or asymmetry factor, which is the average cosine of the scattering directions weighted by the phase function. All the three parameters are wavelength dependent. The optical properties of smoke aerosols are determined by the particle size distribution, spectral complex index of refraction, and mixing mode between black carbon and organic matter. Since combustion particles are generally internally mixed (Liousse et al. 1997), the smoke aerosols in this study are assumed to be solid, spherical cores of black carbon surrounded by viscous organic liquids (Reid et al. 1998b). The size distribution of smoke aerosols is assumed to be lognormal with a volume median radius of 0.15 μm and a standard deviation of 1.80 (Reid et al. 1998b). The spectral complex index of refraction of the black carbon core of smoke aerosols is adopted from Chang and Charalampopoulos (1990). The organic shell is assumed to have a complex refractive index of (1.5, 0i) across the visible spectral band (0.3-3.0 μm) similar to Ross et al. (1998). Smoke particles are assumed to be spheres, which is well supported by SCAR-B measurements (Martins et al. 1998), and Mie theory is applied to stratified spheres (Ackerman and Toon 1981) to calculate the light scattering and absorption coefficients for smoke aerosols. In these calculations, absorption of smoke aerosols varies by changing the ratio of black carbon volume to the total volume of the particles.

Figure 4.3 shows the calculated wavelength-dependent values of τ, ω_0, and g of smoke aerosols using Mie calculations with the assumed smoke aerosol model. Three ratios of soot to total volume are assumed in the calculations, resulting in three spectral curves. From Figure 4.3(b), it is seen that values of ω_0 slightly decrease with increasing wavelength. For the wavelength change from 0.55 μm to 0.75 μm, the ω_0 value decreases by less than 0.02 for all three curves. The extinction coefficient decreases with increasing wavelength, as shown in Figure 4.3(a). From 0.55 μm to 0.75 μm, the coefficient decreases by a factor of about 1.7. The asymmetry factor (g) also decreases with increasing wavelength. From 0.55 μm to 0.75 μm, g decreases by about 0.05. Also, both the ω_0 and g value change with the change of the ratio of soot to total volume.

4.2.2 Visible channel look-up table

The look-up table approach is commonly used in the retrieval of aerosol properties (Kaufman et al. 1996; Stowe and Ignatov 1997). In this study, the Santa Barbara Discrete-ordinate Atmosphere Radiative Transfer (SBDART) model is used to produce the look-up table of radiances as a function of τ and ω_0. The TOA albedos in the visible channel of the AVHRR are pre-calculated for a variety of atmospheric and surface conditions and as a function of sun-satellite viewing geometries. The surface is assumed to be Lambertian, and the standard tropical atmosphere is assumed (McClatchey et al. 1972). The aerosols are

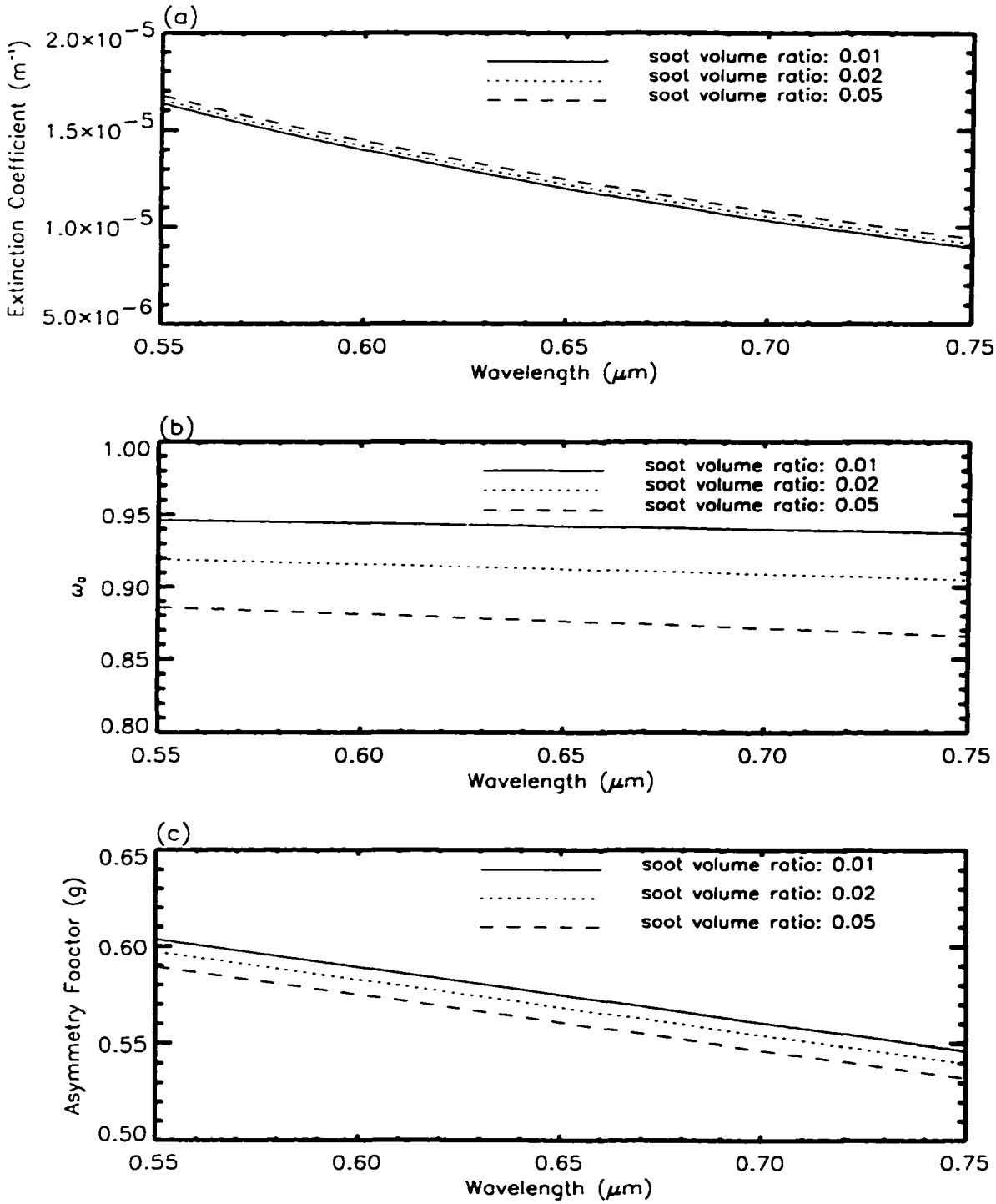

Figure 4.3 (a) τ, (b) ω_o, and (c) g of smoke aerosols as function of wavelength calculated using the assumed smoke aerosol model

characterized in the radiative transfer model by 1) the aerosol extinction coefficient, 2) the single scattering albedo, and 3) the aerosol phase function that are obtained from Mie calculations, as described in Section 4.2.1.

The look-up table is a function of τ(0.64 μm), ω_0(0.64 μm), surface albedo(α_s), solar zenith angle, satellite viewing zenith angle, and relative azimuth angle between the sun and satellite. The discrete-ordinate radiative transfer model used in this study characterizes aerosol concentration in terms of τ at 0.64 μm. The values of τ at other wavelengths are scaled correspondingly, based on Mie calculations. In the look-up-table, the aerosol values of τ at 0.64 μm range from 0.071 to 3.6 in steps of 0.071. The seven ω_0 values are 0.65, 0.70, 0.74, 0.79, 0.85, 0.88, and 0.91, respectively. This is the typical range of ω_0 values for young and aged smoke (Reid et al. 1998a,b). The solar zenith angle ranges between 0-70° and the viewing zenith angle ranges between 0-60° in 5° increments. The relative azimuth angle ranges from 0-180° in 10° intervals. There are 13 α_s values. They are 0.03, 0.06, 0.07, 0.08, 0.09, 0.10, 0.11, 0.12, 0.13, 0.14, 0.15, 0.17, and 0.20, covering the range for surface types in the Amazon and Africa.

The radiative transfer model requires clear-sky surface albedos, whereas the satellite-measured values are at the TOA. Therefore, the radiative transfer model is used to calculate the TOA albedos under clear sky (aerosol and cloud free) conditions corresponding to each of the α_s values. In this way we obtain the

relationship between α_s and TOA clear sky albedo, and then the TOA clear sky albedo is used in the aerosol retrieval process.

Since only the visible channel reflectance of AVHRR imagery is used in the retrieval process, only one parameter of τ and ω_0 can be retrieved at any given time, assuming the other parameter. For example, in a scenario in which τ is available, such as over a sunphotometer site, the value of ω_0 can be retrieved from AVHRR channel 1. For more than a dozen sites during SCAR-B where the τ values were obtained from sunphotometer measurements, the ω_0 values were retrieved using AVHRR-14 channel 1 images and then compared with values obtained from *in situ* and ground-based measurements. The comparisons show good agreement between the two data sets, and results are presented in Chapter 5. The τ values of smoke aerosols also can be retrieved from AVHRR channel 1 assuming the ω_0 values of smoke aerosols, since the ω_0 values generally are found in a narrow range from 0.8 to 0.9 over South America, with a typical value of 0.89 (Reid et al. 1999).

The look-up-table for VIRS channel 1 is also calculated using the same approach. The difference in the two look-up-tables is caused only by the difference of the spectral response functions of the two sensors.

4.2.3. Sensitivity study

In the retrieval of ω_0 given τ, the accuracy of the retrieved ω_0 values is mainly determined by the accuracy of aerosol τ values, the calculated TOA clear-sky albedos, and the AVHRR observed TOA reflectances. Figure 4.4 shows the uncertainty in retrieved values of ω_0 as a function of TOA clear-sky albedos. The solar zenith angle and viewing zenith angle are 30° in this example, and the relative azimuth between the sun and the sensor is 40°. The surface is assumed to be Lambertian with an albedo of 0.10, and the corresponding TOA clear-sky albedo is about 0.11.

Sensitivity is examined for 5 different values of aerosol τ, ranging from 0.28 (light aerosol concentration) to 1.78 (heavy aerosol concentration). From Figure 4.4, it is seen that the retrieved value of ω_0 is very sensitive to the TOA clear-sky albedo for small τ values, while for heavy smoke concentrations, the retrieved ω_0 is less sensitive to the TOA clear sky albedo values. The errors of retrieved values of ω_0 due to one percent uncertainty in TOA clear-sky albedo are -0.085, -0.033, -0.016, -0.012, and -0.004, for τ values of 0.28, 0.56, 0.85, 1.07 and 1.78, respectively. The minus sign indicates that overestimation of TOA clear-sky albedo will underestimate the retrieved values of ω_0. The sensitivity of the retrieved values of ω_0 to the TOA clear-sky albedos for different values of τ is given in Table 4.2.

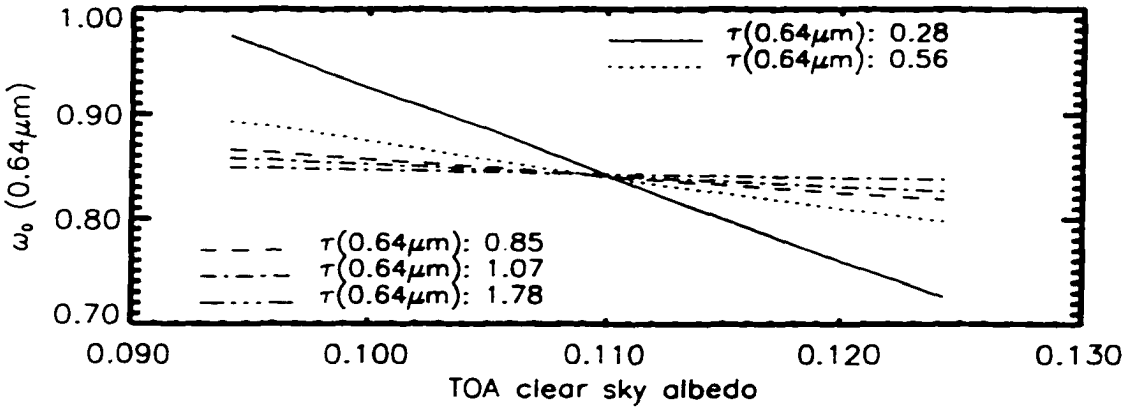

Figure 4.4 The uncertainty of retrieved ω_0 due to the uncertainty of TOA clear-sky albedo for 5 different aerosol concentrations

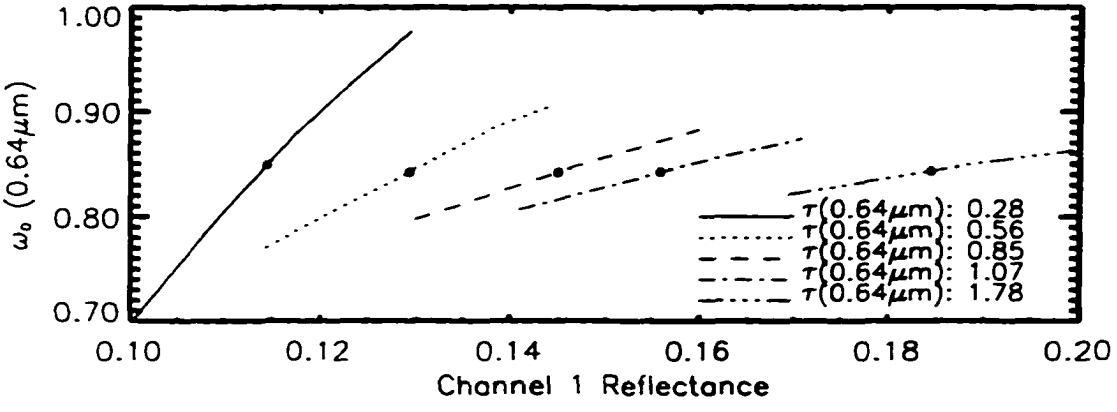

Figure 4.5 The uncertainty of retrieved ω_0 due to the uncertainty of the observed chanel 1 reflectance for 5 different aerosol concentrations

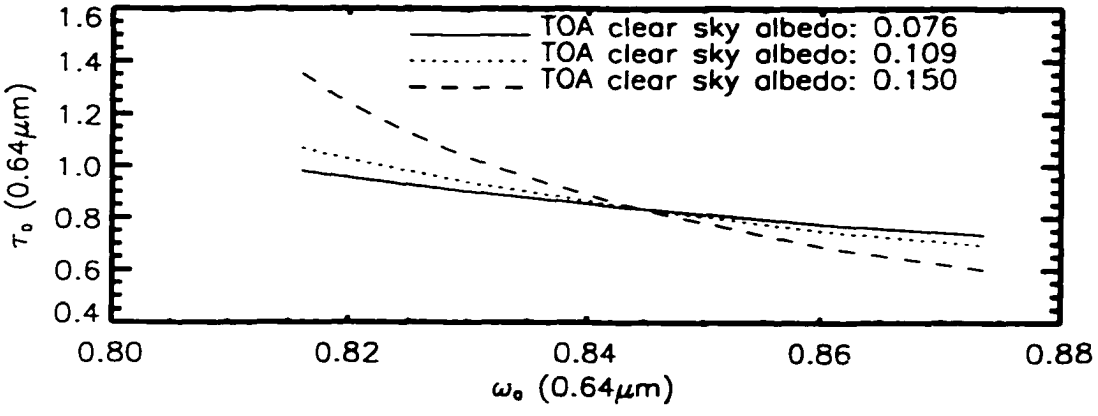

Figure 4.6 The uncertainty of retrieved τ due to the uncertainty in assumed value of ω_0 for 3 different TOA clear-sky albedos

Table 4.2 Sensitivity of retrieved $\omega_0(0.64\mu m)$ as function of TOA clear-sky albedo given $\tau(0.64\mu m)$. The solar zenith angle, satellite zenith angle and relative azimuth angle are 30°, 30°, and 40°, respectively, original ω_0 is 0.845.

TOA clear sky albedo(%)	$\Delta\omega_0/\Delta\alpha_{TOA\_clear}(\%)$				
	τ=0.28	τ=0.56	τ=0.85	τ=1.07	τ=1.78
7.6	-0.112	-0.039	-0.018	-0.012	-0.004
11.0	-0.085	-0.033	-0.016	-0.012	-0.004
15.1	-0.067	-0.027	-0.014	-0.010	-0.004

Table 4.2 shows that for dense smoke concentrations, the values of retrieved ω_0 are not sensitive to the clear-sky albedo, while for light smoke concentrations, the ω_0 values are much more sensitive to the clear-sky albedo. Errors in retrieved values of ω_0 increase with decreasing values of TOA clear-sky albedo and for decreasing values of aerosol optical thicknesses.

Figure 4.5 shows the errors in retrieved values of ω_0 due to uncertainties in TOA observed reflectance for the range of τ values shown in Table 4.2. The solar and viewing geometry is the same as in figure 4.4. The value of ω_0 is assumed to be 0.85 and α_s is 0.10. The retrieved value of ω_0 becomes more sensitive to TOA reflectance at small values of τ and becomes less sensitive at large values of τ. For example, when τ is 0.28, the value of ω_0 will be underestimated, decreasing from 0.85 to 0.75 as the TOA reflectance decreases from 0.114 to 0.104. When the value of τ is 1.78, the value of ω_0 is only slightly affected, decreasing from 0.84 to 0.83 as the TOA reflectance decreases from 0.184 to 0.174. Errors in the retrieved values of ω_0 increase with decreasing

values of TOA reflectance and for decreasing values of aerosol optical thicknesses.

Since only the visible channel of AVHRR imagery is used in the retrievals, only one parameter can be retrieved at any given time. Smoke optical thickness can be retrieved assuming a typical value of ω_0 obtained from field experiments, such as SCAR-B. The accuracy of retrieved τ values is directly affected by the assumed values of ω_0. Figure 4.6 shows uncertainties of retrieved values of τ due to uncertainties in the assumed values of ω_0. The solar and viewing geometry is the same as in Figures 4.4 and 4.5.

From Figure 4.6, it is seen that errors in retrieved τ values are a function both of errors in values of ω_0 and errors of TOA clear-sky albedos. In general, the darker the surface, the more accurately the values of τ can be retrieved. For example, when the TOA clear-sky albedo is 0.109, an error in the assumed value of ω_0 by 0.01 causes an error in retrieved value of τ by 0.06. However, for a TOA clear-sky albedo of 0.15, the error in retrieved τ value increases to about 0.16. Also from Figure 4.6, it is seen that the retrieved τ value is more sensitive to the assumed value of ω_0 when ω_0 is smaller (more absorptive).

Table 4.3 shows the uncertainty of retrieved value of τ with the uncertainty of assumed value of ω_0 at the solar and viewing geometry used in Figure 4.6. The sensitivity of retrieved τ values to the assumed ω_0 value is shown for three

aerosol optical thicknesses: 0.35, 1.07 and 1.78, representing light, medium and heavy smoke concentrations. From Table 4.3, the uncertainty of retrieved τ is sensitive to both the aerosol optical thickness and the TOA clear-sky albedo. The smaller the TOA albedo (the darker the surface), the less sensitive is the retrieved value of τ. The denser the smoke (the larger the τ), the more sensitive the retrieved value of τ.

The uncertainties of retrieved τ due to the uncertainties of TOA clear sky albedo and observed albedo also are examined. The solar and viewing angles are assumed to be the same as ones in Figure 4.4. When the TOA clear sky albedo, ω_0 and τ values are 0.109, 0.85 and 1.06, respectively, AVHRR channel 1 reflectance is 0.156. An increase of TOA clear-sky albedo from 0.109 to 0.119 causes a decrease in the retrieved τ value from 1.06 to 0.94. On the other hand, a decrease of channel 1 reflectance from 0.156 to 0.146 causes a decrease in the retrieved τ value from 1.06 to 0.86. An uncertainty of 0.01 in TOA clear-sky albedo or channel 1 reflectance causes uncertanity of retrieved τ value by about 0.1-0.2.

Table 4.3. Sensitivity of retrieved τ (0.64 μm) as function of ω_0(0.64 μm) given TOA clear sky albedo. The solar and viewing geometry is same as in Table 4.1. Original ω_0 is 0.845

TOA clear sky albedo(%)	$\Delta\tau/\Delta\omega_0$ τ=0.35	τ=1.07	τ=1.78
7.6	-1.32	-4.05	-16.08
11.0	-2.29	-6.04	-21.06
15.1	-5.10	-10.77	-32.68

4.3 Smoke angular distribution model

The angular distribution model (ADM) is an integral part of the Earth Radiation Budget Experiment (ERBE) and Cloud and Earth Radiant Energy System (CERES) projects. It is used to convert the measured TOA radiances into TOA fluxes, and the accuracy of the ADM directly determines the accuracy of the TOA fluxes. However, there is no ADM for smoke aerosols in either of these projects. In this study, the smoke ADM is calculated using the optical properties of smoke aerosols obtained from SCAR-B results and the SBDART radiative transfer model.

4.3.1 Angular Distribution Model (ADM)

The measured radiance from the CERES scanner at a specific sun-satellite angle is converted to TOA flux (Green et al. 1995) using the following equation:

$$F_{TOA}^{\uparrow} = \frac{\pi I(\theta_0, \theta, \varphi)}{\xi(\theta_0, \theta, \varphi)} \quad \text{.....(4.1),}$$

where $I(\theta_0, \theta, \phi)$ is the sensor-measured radiance at solar zenith angle θ_0, satellite zenith angle θ, and relative azimuth angle between Sun and satellite ϕ, $\xi(\theta_0, \theta, \phi)$ is the angular distribution model value that relates radiance to flux at

that specific solar and satellite viewing geometry, and $F^{\uparrow}_{TOA}$ is the TOA upward flux in the 0.3 – 5.0 μm shortwave channel. As a result, the accuracy of converted TOA SW fluxes over biomass burning regions depends upon the accuracy of the ADM for smoke aerosols.

The SBDART model is used to calculate the shortwave (0.28 – 4.0 μm) ADM for horizontally homogeneous smoke aerosols over different surface types. The SBDART model was introduced in Chapter 3 and was used to produce the look-up-table for the retrieval of smoke optical properties in Section 4.2. The spectral optical properties of smoke aerosols used in this study are obtained from the SCAR-B experiment (Ross et al. 1998), with smoke particles modeled as organic liquid shells with black carbon cores (Ross et al. 1998). The volume size distribution of smoke aerosols is assumed to be lognormal with a volume median radius of 0.15 μm (Remer et al. 1998). Smoke particles are assumed to be spheres, which is well supported by SCAR-B measurements (Martins et al. 1998), and Mie theory is applied to stratified spheres (Ackerman and Toon 1981) to calculate the light scattering and absorption coefficients of the smoke aerosols. Figures 4.7 show the mass extinction coefficients in (a), and single scattering albedos and asymmetry factors in (b) as a function of wavelength. The curves at 3.0-4.0 μm are extrapolated from the curves at 0.30-3.0 μm, since Ross et al (1998) provided values only up to 3.0 μm. In Figure 4.7(b), the ω_0 value at 0.55 μm is 0.81. For smoke aerosols with different absorption properties (i.e., different ω_0 values at 0.55 μm), the corresponding spectral ω_0 curve (curve 2) is scaled

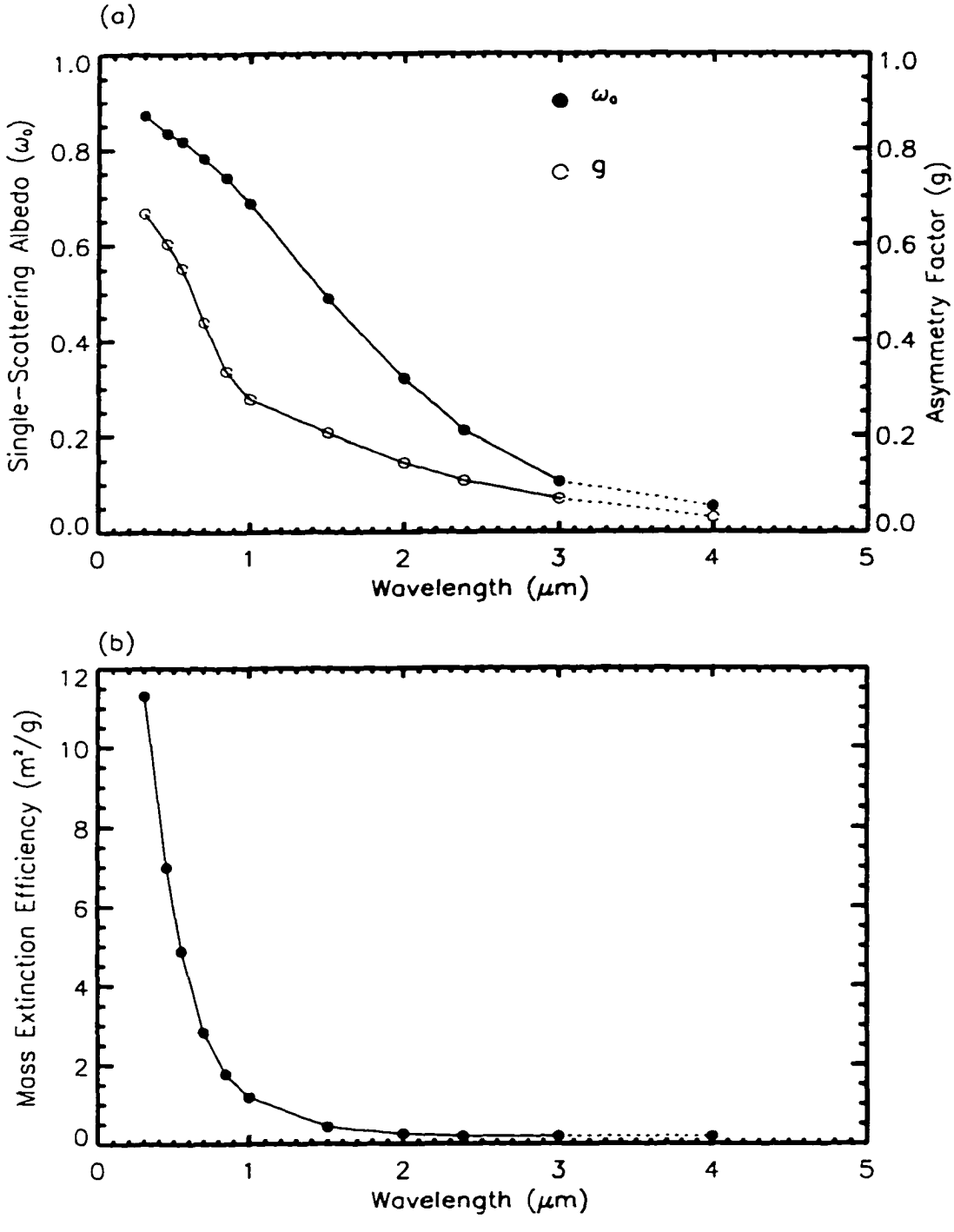

Figure 4.7 (a) Single scattering albedo and asymmetry factor and (b) mass extinction coefficient of smoke aerosols as the function of wavelength from Mie calculations

from the curve (curve 1) in Figure 4.7(b) according to their ω_0 value at 0.55 μm using the following equation:

$$\omega_{0,2}(\lambda) = \frac{\omega_{0,2}(550nm)}{\omega_{0,1}(550nm)} \omega_{0,1}(\lambda) \quad \text{.....(4.2),}$$

where $\omega_{0,2}(\lambda)$ represents the ω_0 value at wavelength λ for the scaled curve, and $\omega_{0,1}(\lambda)$ represents the ω_0 value at wavelength λ for the curve in Figure 4.7(b).

In the smoke ADM calculations, a standard tropical atmosphere (McClatchey et al. 1972) is assumed, and the surface is assumed to be Lambertian. In this study, we refer to the calculated ADM for smoke aerosols as the "smoke ADM". The smoke ADM is a function of τ, ω_0, broadband surface albedo (α_s), θ_0, θ, and φ. The τ and ω_0 values are specified at a wavelength of 0.64 μm unless otherwise stated. The aerosol values of τ are calculated in the range from 0.36 to 3.6 in steps of 0.36. There are four ω_0 values used in the calculations: 0.70, 0.79, 0.82, and 0.85, respectively. There are 10 solar zenith angles used in the calculations with cosine of the angles decreasing from 0.90 to 0.45 in steps of 0.05. Likewise, there are 15 satellite zenith angles with cosines of the angles decreasing from 1.0 to 0.3 in steps of 0.05. Values of φ range from 0° to 180° in intervals of 22.5°. There are four assumed values of α_s: 0.10, 0.15, 0.20, and 0.25, covering the range for the surface types found in the biomass burning regions.

Figures 4.8a–d show the calculated ADMs for aerosol values of τ of 0.36, 1.1, 1.8, and 2.5, respectively. In these calculations, the aerosol ω_0 value is assumed to be 0.85, α_s is assumed to be 0.15, and the solar zenith angle is assumed to be 36.9°. The relative azimuth angle of 0° represents the forward direction of scattering. From Figures 4.8a–d, the ADM value increases with increasing satellite zenith angle. Consider the case when the τ value is 0.36; then the ADM values in the forward scattering direction (φ=0°) increase from 0.87 to 1.34 and values in the backward scattering direction (φ=180°) increase from 0.87 to 1.11 as θ values increase from 0° to 69.5°. Now consider the case when the τ value increases from 0.36 to 2.5; then the ADM values in the forward direction increase from 0.83 to 1.49 and values in the backward direction increase from 0.83 to 0.96 as θ values increase from 0° to 69.5°. Therefore, with increasing value of τ, the range of ADM values in the forward direction increases and values in the backward direction decrease. Comparison of Figures 4.8c and 4.8d shows no significant difference between the two ADMs, indicating that the smoke ADM is not sensitive to the value of τ when τ is larger than 1.8 (heavy smoke concentration). Figures 4.8e and 4.8f show smoke ADMs the with same values of ω_0 and solar zenith angle as in Figure 4.8a and 4.8c, but with the value of α_s increased from 0.15 to 0.20. The τ values for Figures 4.8e and 4.8f are 0.36 and 1.8, respectively. Comparison of Figures 4.8f and 4.8c, with τ = 1.8, shows no large difference between the two ADMs, indicating that when aerosol τ is large, the smoke ADM is less dependent on the surface albedo (surface type).

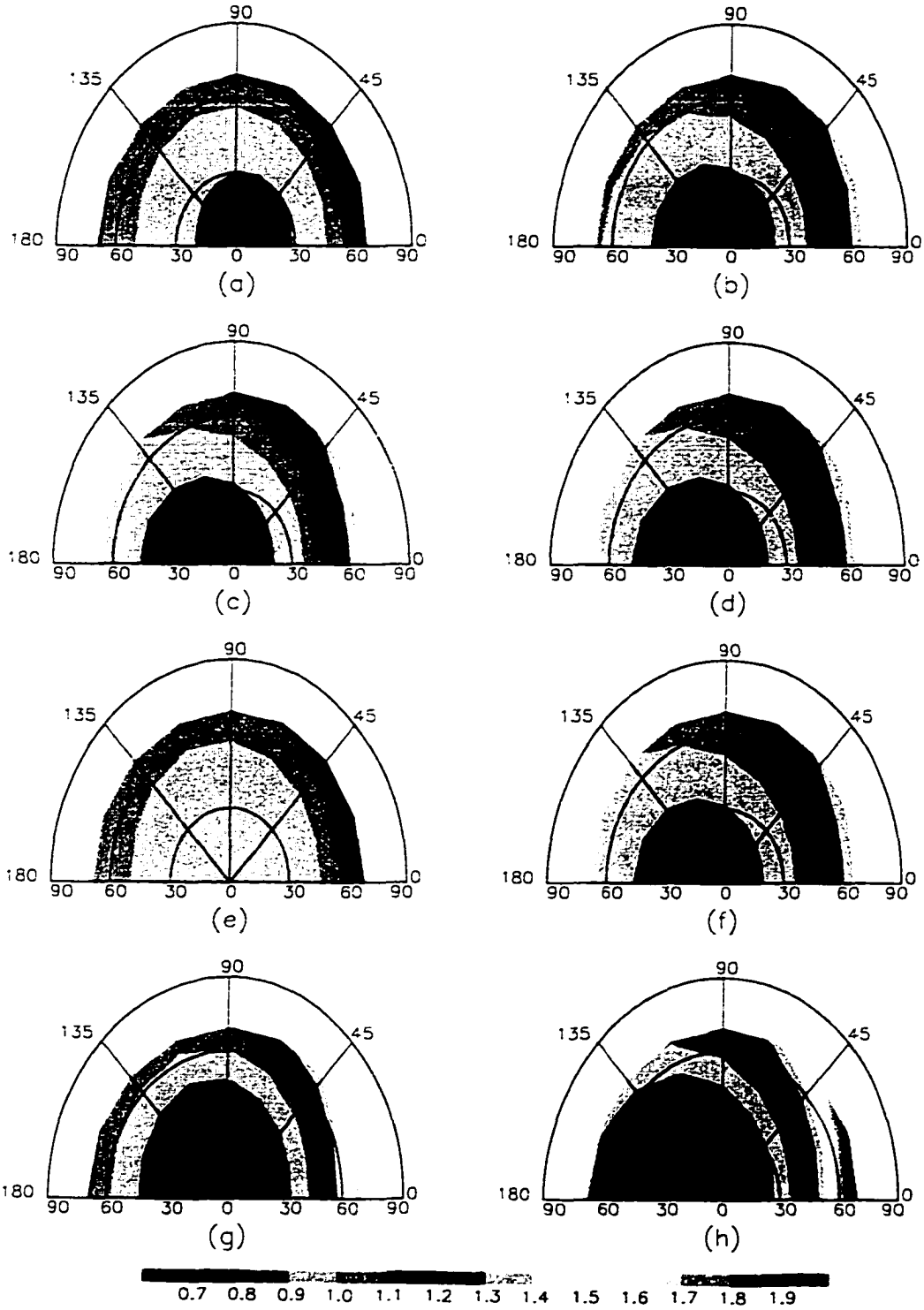

Figure 4.8 Calculated smoke ADM at (a) τ=0.36, ω_0=0.85, α_s=0.15, sza=36.9°, (b) τ=1.1, ω_0=0.85, α_s=0.15, sza=36.9°, (c) τ=1.8, ω_0=0.85, α_s=0.15, sza=36.9°, (d) τ=2.5, ω_0=0.85, α_s=0.15, sza=36.9°, (e) τ=0.36, ω_0=0.85, α_s=0.20, sza=36.9°, (f) τ=1.8, ω_0=0.85, α_s=0.20, sza=36.9°, (g) τ=0.36, ω_0=0.85, α_s=0.15, sza=60.0°, and (h) τ=1.8, ω_0=0.85, α_s=0.15, sza=60.0°

Comparison of Figures 4.8e and 4.8a, with τ = 0.36, shows large differences in the smoke ADMs. In the forward and backward scattering directions, the ADM values in Figure 4.8e range from 0.91 to 1.28 and from 0.91 to 1.07, respectively. Comparing to Figure 4.8a, the range of ADM values decreases in both the forward and backward scattering directions. The reason is that for small values of aerosol τ, the surface albedo has a greater impact on the smoke ADM. Holding the τ, ω_0 and α_s values the same as in Figures 4.8e and 4.8f, Figures 4.8g and 4.8h show smoke ADMs with solar zenith angle increased from 36.9° to 60°. In Figure 4.8h, the ADM values range from 0.73 to 2.12 in the forward scattering direction and from 0.73 to 0.90 in the backward scattering directions as θ values increase from 0° to 69.5°. Comparison of Figures 4.8f and 4.8h shows that the range of smoke ADM values in the forward scattering direction significantly increases with increasing solar zenith angle. That is, at larger solar zenith angle, the smoke ADM is less isotropic.

4.3.2 Sensitivity study

Since the smoke ADM is a function of τ, ω_0, α_s, uncertainties in these values cause uncertainties of the smoke ADM values. Since the TOA clear-sky albedo is directly related to α_s in clear-sky conditions, the sensitivity of the smoke ADM to the parameters of τ, ω_0, and TOA clear-sky albedo is examined. Figure 4.9a shows the ADM value as the function of smoke τ value. In this case, the ω_0,

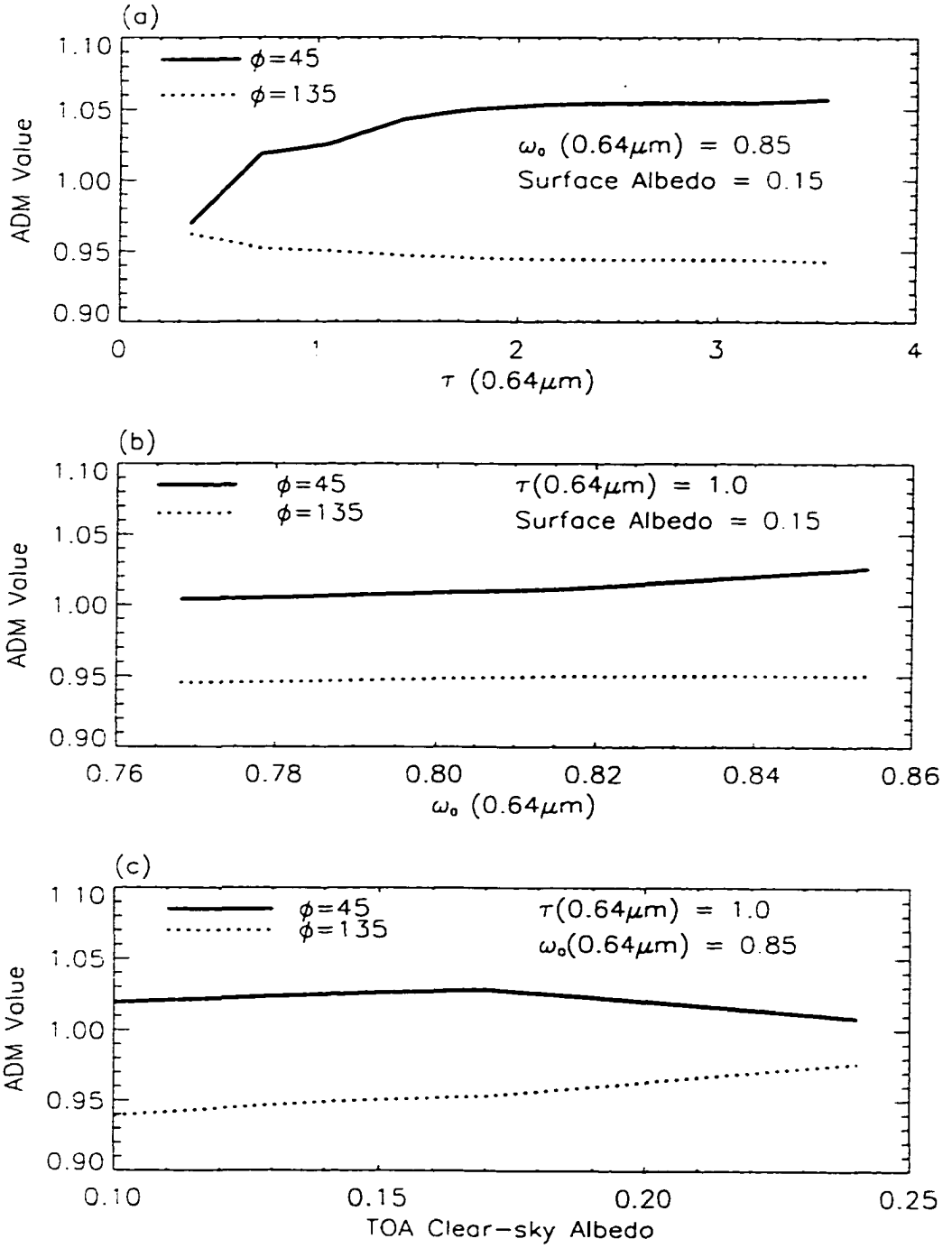

Figure 4.9 Uncertainty of smoke ADM value as function of (a) τ, (b) ω_o, and (c) TOA clear-sky albedo. ϕ represents relative azimuth angle between Sun and satellite

α_s and θ values are 0.85, 0.15 and 40°, respectively, and the solar zenith angles are assumed to be 30° and 60°, respectively. The relative azimuth angles are assumed to be 45° (forward scattering) and 135° (backward scattering), respectively.

From Figure 4.9a, it is seen that the ADM values are not sensitive to the values of τ when τ is larger than 1.7. When τ is less than 1.7, the ADM values become more sensitive to the τ values, especially at the larger solar zenith angles. When ϕ_0 is 60°, the ADM values vary from 0.97 to 1.04 as the τ values vary from 0.35 to 1.5, an increase of about 7%. Figure 4.9b shows the ADM values as a function of ω_0. In this case, the τ value is 1.1, and TOA clear-sky albedo and solar and satellite viewing geometry are identical to the ones in Figure 4.9a. The ADM values are relatively insensitive to values of ω_0 when the ω_0 values are less than 0.81, becoming more sensitive to the values of ω_0 as the ω_0 values become larger than 0.81. Note that the ADM values vary by less than 3% when the ω_0 value varies from 0.76 to 0.85. Figure 4.9c shows the ADM values as a function of TOA clear-sky albedo. In this case, the ω_0 value is 0.85 and the τ value is 1.1. The solar zenith angle, satellite angle and relative azimuth angle are identical to those in Figures 4.9a and 4.9b. From Figure 4.9c, it is seen that the ADM values are slightly more sensitive to TOA clear-sky albedo in the backward scattering direction than in the forward scattering direction. The ADM value varies from 0.92 to 0.97 as clear-sky albedo changes from 0.10 to 0.24, a change of about 5%.

In general, we conclude that the smoke ADMs are relatively insensitive to the smoke optical properties and TOA clear-sky albedos. For most cases, the uncertainty of smoke ADM is expected to be less than 10% due to the uncertainties of these parameters.

4.4 Modified δ-4 stream broadband model for smoke aerosols

While the global earth radiation budget can be directly obtained from satellite measurements such as ERBE and CERES, it is typical to use radiative transfer models (Pinker and Laszlo 1992; Zhang and Rossow 1995) or model-derived relationships between the TOA and surface SW fluxes (Li et al 1993) to estimate the Solar Surface Radiation Budget (SSRB) from satellite observations. As mentioned in Chapter 1, although the model-estimated surface SW radiation budget is in reasonably good agreement with the observations, significant discrepancies between model results and surface observations exist over regions where biomass burning prevails (Konzelmann et al. 1996; Li 1998). The large discrepancies are most probably due to the improper characterization of smoke aerosols in the model calculations. For example, the aerosols in the Global Energy and Water cycle Experiment (GEWEX) Surface Radiation Budget (SRB) SW radiative transfer model (Pinker and Laszlo 1992) are assumed to be either marine or continental types. The reason that biomass burning aerosols have not been properly treated in the models is that little information has been available

concerning their optical properties. The δ-four-stream plane-parallel broadband radiative transfer model (Fu and Liou 1993), as presented in Chapter 3, is a popular model that is used by the CERES Surface and Atmosphere Radiation Budget (SARB) team to estimate the SW and longwave (LW) fluxes at both the TOA and the surface as well as in the atmosphere. Using this model, the diurnally averaged radiative impact of dust aerosols has been simulated (Liao and Seinfeld 1998). However, smoke aerosols have not been characterized in this model. In the present study, the δ-four-stream model is modified to account for the smoke aerosol effect using the optical properties obtained during SCAR-B so that it can be used to estimate surface SW radiation budget over biomass burning regions.

4.4.1 Characterization of smoke aerosols

One of the standard techniques for computing the optical properties of aerosols is to assume an aerosol size distribution and refractive index which are then used as input to Mie calculations (e.g., Kaufman and Nakajima 1993; Lenoble 1991). The smoke aerosol particles are assumed to be spherical, and Mie calculations are performed, providing the phase functions, single scattering albedos (ω_0), asymmetry parameters (g) and extinction coefficients. These values then are used to compute the TOA and surface irradiance values. In this section, the wavelength-dependent ω_0 and g parameters are taken from the

SCAR-B experiment (Ross et al. 1998). The wavelength-dependent extinction coefficient (which can be scaled to obtain wavelength-dependent τ parameter) is obtained by a different approach. Since the sunphotometers measure τ values at seven wavelengths from 0.34 μm to 1.02 μm, the wavelength-dependent τ parameter for smoke aerosols at 0.34 – 1.02 μm is obtained based on the observed τ values over 12 sunphotometer sites during SCAR-B. The wavelength dependency of the τ value between any of the two observed wavelengths is obtained by the linear interpolation of the mean values of τ at the two wavelengths. The wavelength-dependency of τ between 1.02 and 4.0 μm, as required in the model, is obtained by extrapolation of the mean values of τ at 0.87 μm and 1.02 μm. The uncertainty in characterizing smoke aerosols due to the uncertainty of the assumed wavelength-dependent τ value at wavelength larger than 1.02 μm is less significant due to the fact that 1) smoke optical thickness decreases significantly with increasing wavelength and 2) solar energy decreases significantly at wavelengths larger than 1.0 μm. As a result, the extrapolation of wavelength-dependent τ values is not expected to significantly affect the accuracy of the parameterization of the smoke radiative impact. The wavelength dependency of the τ value is categorized into seven curves based on the observed τ values at a wavelength of 0.50 μm: $\tau < 0.5$, 0.5-1.0, 1.0-1.5, 1.5-2.0, 2.0-2.5, 2.5-3.0, and $\tau > 3.0$. Figure 4.10 shows the seven curves obtained from the sunphotometer measurements during SCAR-B. For the sake of comparison, the wavelength-dependent τ curve based on Mie calculations (Ross

et al. 1998) is also shown in Figure 4.10. From Figure 4.10, it is seen that the τ curves derived from the sunphotometer measurements are similar to the one obtained from Mie calculations.

The four-stream broadband radiative transfer model requires values of τ, ω_0 and g at wavelengths between 0.2-4.0 μm in six discrete intervals. Based on Figures 4.7 and 4.10, the energy-weighted values of ω_0, g and τ for each band (Pinker and Laszlo 1992) are obtained by using the LOWTRAN incoming solar energy spectrum and are characterized in the four-stream model. For the water-soluble aerosols, including the smoke particles, the light scattering coefficient (σ_S) increases as ambient relative humidity (RH) increases. The *humidification factor*, which is a measure of this increase, is defined as the light-scattering coefficient at 80% relative humidity divided by the light-scattering coefficient of the dry aerosol (Kotchenruther and Hobbs 1998). The light scattering coefficients of smoke particles from various types of fires as a function of relative humidity were estimated from these measurements, and the single scattering albedos used in the calculation account for this humidification factor.

The aerosol τ and ω_0 values at 0.55 μm are required as input to characterize the radiative impact of smoke aerosols in the modified model. This model is validated using the observational data during SCAR-B and results as discussed in Chapter 5.

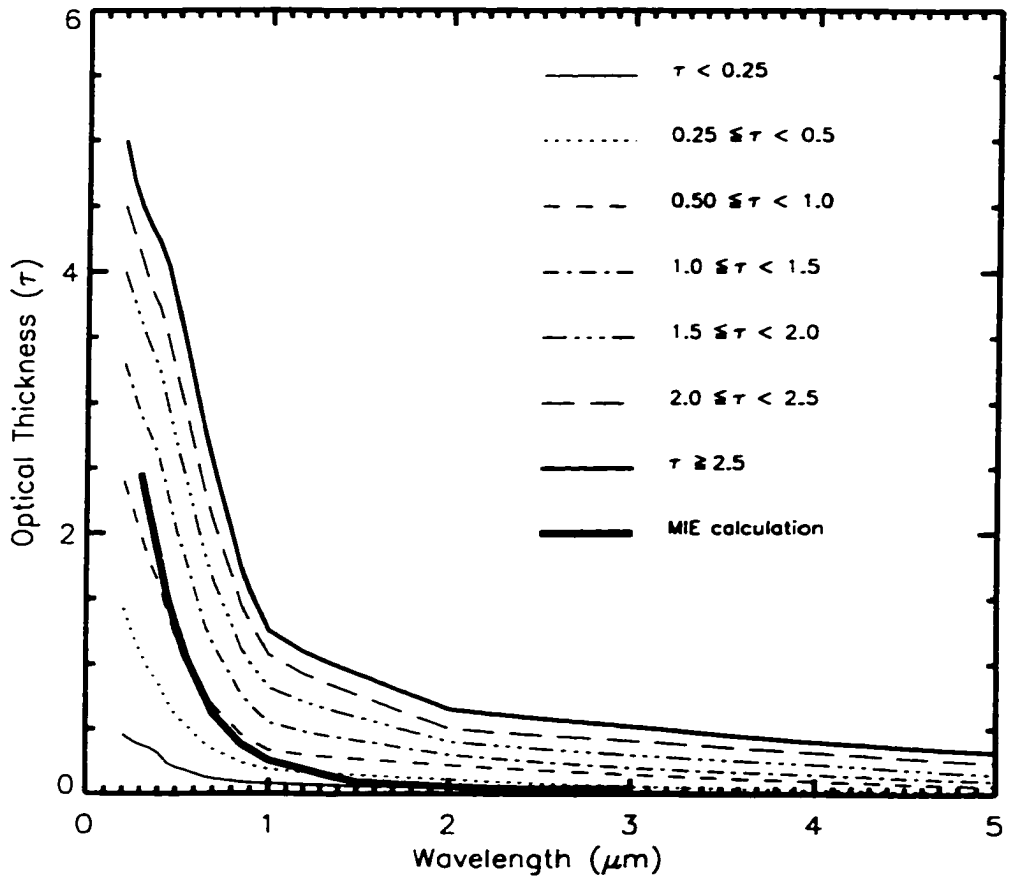

Figure 4.10 The wavelength-dependent optical thickness curves derived from sunphotometer measurements during SCAR-B. The model-calculated curve shown in Figure 4.7(a) is scaled so that $\tau(0.55\mu m)=1.0$ and ploted here as thick line for comparison

4.4.2 Sensitivity of TOA and surface SW fluxes to aerosol and ambient parameters

The sensitivity of several model parameters to TOA and surface SW fluxes are examined using the four-stream radiative transfer calculations. The following model parameters are examined: 1) aerosol optical thickness, 2) single-scattering albedo, 3) asymmetry parameter, 4) surface albedo, 5) column water vapor amount, and 6) column ozone amount.

As a first test, the sensitivity of downward shortwave irradiances (DSWIs) to a range of aerosol optical thicknesses at 0.55 μm is examined as a function of solar zenith angle. To perform these calculations, ω_0, surface albedo, *g*, column water vapor and ozone amounts are fixed. The column ω_0 (at 0.55 μm) for smoke aerosols between 0-4 km is assumed to be 0.823, the mean value of UW C-131A airborne measurements during SCAR-B, and the column g value is 0.55. The surface albedo is set to be 0.12. The standard tropical vertical profiles of water vapor and ozone are assumed. By varying the τ values, while holding all other parameters constant, the sensitivity of the DSWI values to τ can be estimated. Figure 4.11(a) shows that the calculated values of DSWI are extremely sensitive to the assumed values of τ. As τ increases at a given solar zenith angle (θ_0), the amount of SW energy at the surface decreases. Also, for a constant value of τ, a larger solar zenith angle produces lower DSWI values. For example, at $\theta_0 = 31.7^\circ$ ($\cos(\theta_0) = 0.85$), as τ varies from 0.5 to 1.0 the DSWI

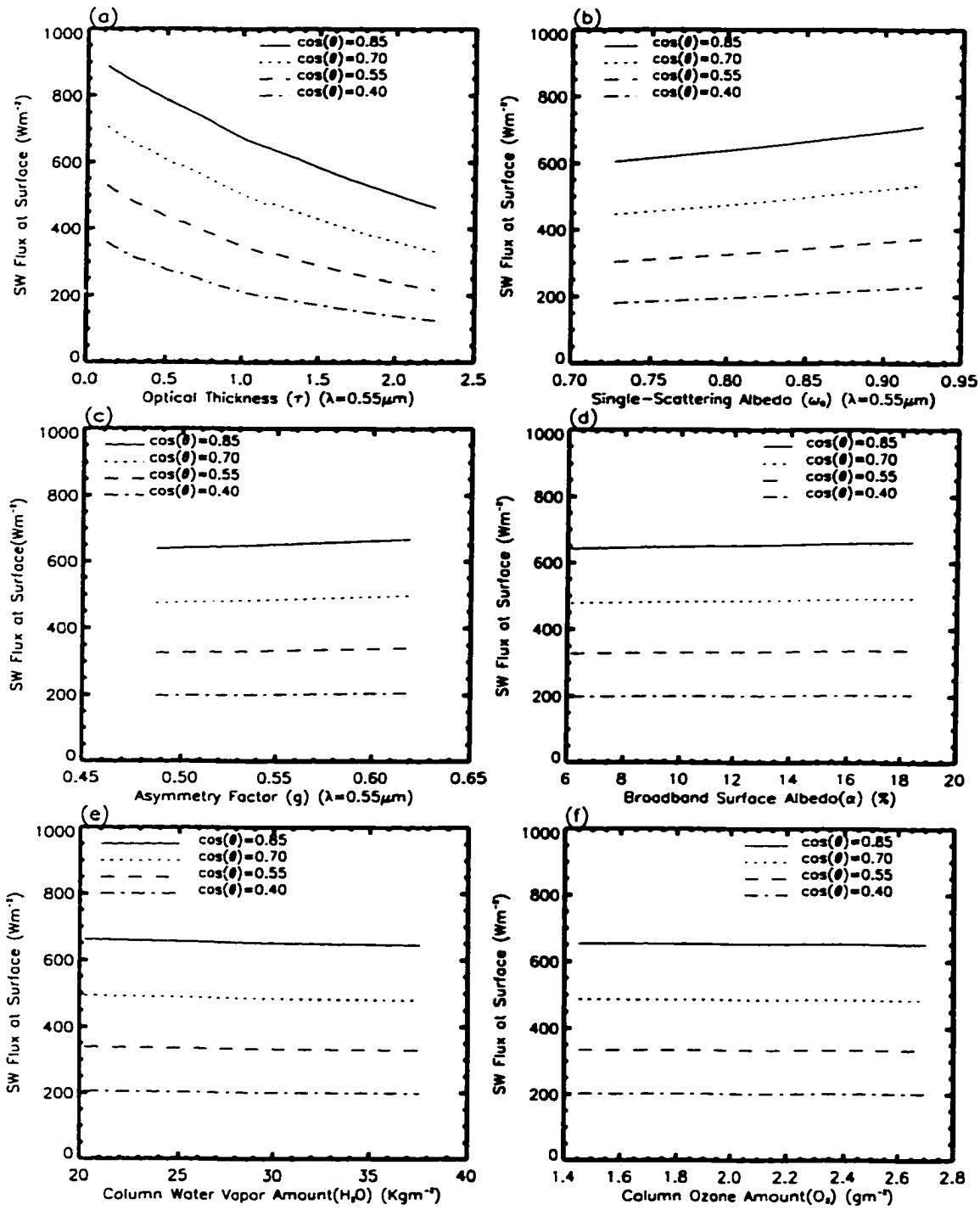

Figure 4.11 Sensitivity of surface downward SW flux to the uncertainty of 1) τ, 2) ω_0, 3) g, 4) surface albedo, 5) column water vapor amount and 6) column ozone amount

value changes from 750-600 W m^{-2}. The radiative transfer calculations show that an uncertainty of 0.1 in τ (and for the range of smoke optical thickness and solar zenith angles that are considered here) yields an uncertainty of about 20-30 Wm^{-2} in DSWI, assuming that all other variables (e.g. *g*, ω_0) are known.

Figure 4.11(b) shows the sensitivity of the calculated DSWI values to ω_0 at different solar zenith angles. The column τ is assumed to be 0.9 at 0.55 μm. At a given θ_0, the DSWI values increase with increasing ω_0 values due to the less absorption of smoke particles. At a θ_0 of 31.7°, a change in ω_0 from 0.80 to 0.85 produces an increase in DSWI of about 25 Wm^{-2}. Figure 4.11(c)-(f) shows that only small changes in DSWI occur as *g*, surface albedo, column water vapor and column ozone are varied. A change in *g* of 10% (between 0.55-0.60) produces a change in DSWI of less than 10 Wm^{-2}. Likewise, a 40% change in surface albedo (from 10-14%) produces a DSWI change of less than 10W m^{-2}. Similar changes can be seen in Figure 4.11(e) and (f) as column water vapor and column ozone values are changed. From Figure 4.11 we conclude that the DSWI calculations are sensitive primarily to the assumed values of τ and ω_0. Indeed, values of both τ and ω_0 must be estimated to within 10-12% to obtain DSWI values within 20 Wm^{-2}, which means that τ and ω_0 must be estimated to within 0.1 and 0.05, respectively. Therefore, if global retrievals of DSWI are to be done on a routine basis using the combination of satellite and radiative transfer calculations, new methodologies must be developed to estimate τ and ω_0 accurately.

The sensitivity of TOA upward SW flux (TUSWF) to these six parameters also is examined, and results are shown in Figure 4.12. In Figure 4.12(a), values of ω_0, surface albedo, *g*, column water vapor and ozone amounts are fixed. The value of column ω_0 (at 0.55 μm) for smoke aerosols between heights of 0-4 km is assumed to be 0.89, and the column g value is 0.55. Once again, these are typical values from SCAR-B. The surface albedo is assumed to be 0.12. Figure 4.12(a) shows that the calculated values of USWF are extremely sensitive to the assumed values of τ. The value of TUSWF increases with increasing value of τ at a given θ_0. Also, for a constant value of τ, a larger solar zenith angle produces larger values of TUSWF. For example, at $\theta = 31.7^{\circ}$, as τ varies from 0.5 to 1.0 the value of TUSWF increases from 248 to 261 Wm^{-2}, an increase of 13 Wm^{-2}. The radiative transfer calculations show that an uncertainty of 0.1 in τ (and for the range of smoke optical thickness and solar zenith angles that are considered here) will yield an uncertainty of about 2-3 Wm^{-2} in TUSWF, assuming that all other variables (e.g. *g*, ω_0) are known. However, the sensitivity of TUSWF to the column τ value also is dependent upon the ω_0 value. For example, when the value of ω_0 is 0.823, the TUSWF value changes from 228.9 to 228.5 Wm^{-2} as τ increases from 0.5 to 1.0. This is due to the balance between the brightening of the surface by atmospheric scattering and the darkening by aerosol absorption for smoke aerosols (Kaufman 1987). Figure 4.12(b) shows the sensitivity of the calculated TUSWF values to values of ω_0 at different solar zenith angles. The value of column τ is assumed to be 0.9 at 0.55 μm. For a given θ_0, the values of TUSWF increase with increasing values of ω_0 due to the decrease of absorption

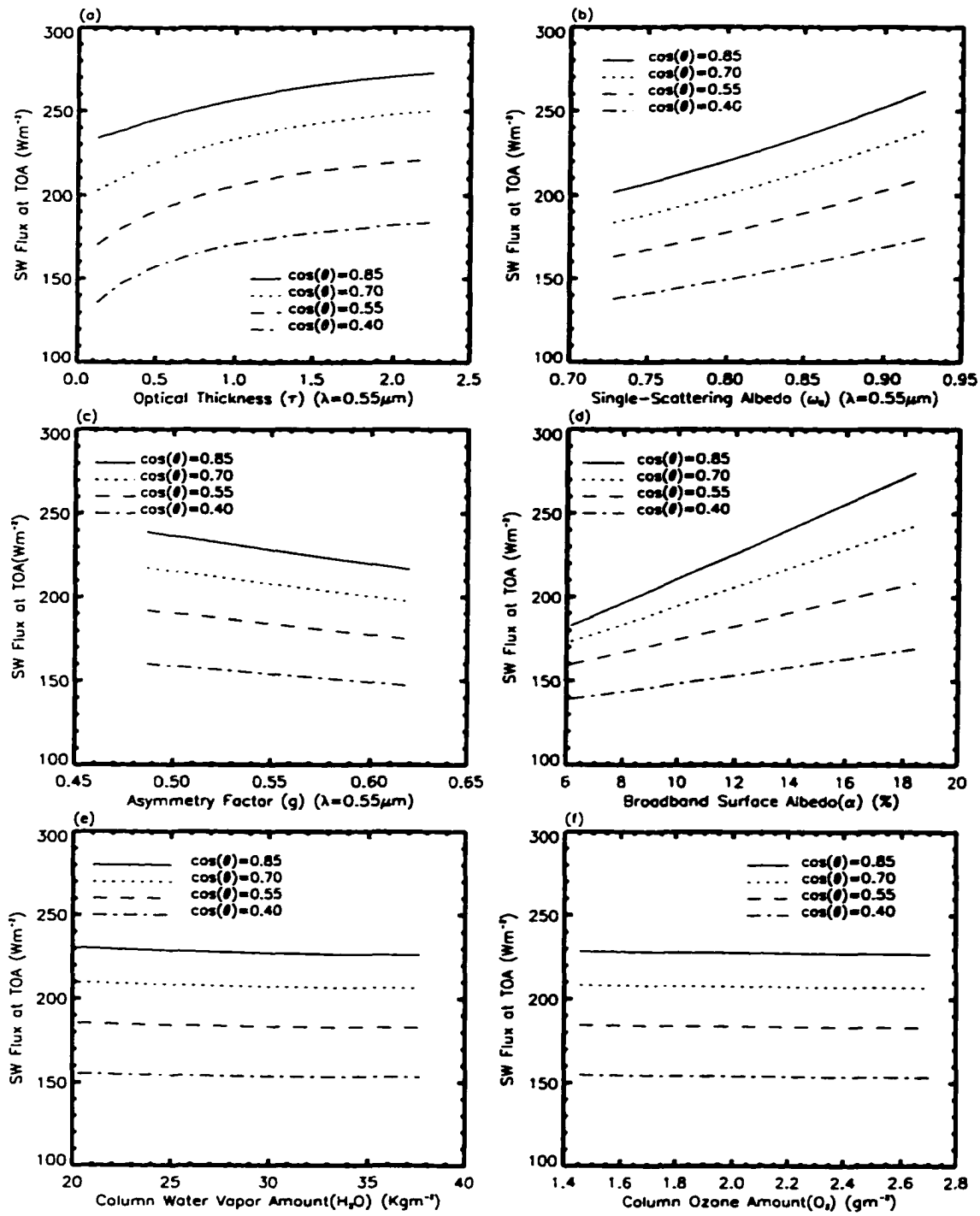

Figure 4.12 Sensitivity of TOA upward SW flux to the uncertainty of 1) τ, 2) ω_0, 3) g, 4) surface albedo, 5) column water vapor amount and 6) column ozone amount

for smoke aerosols. At a θ_0 of 31.7°, a change in ω_0 from 0.80 to 0.85 produces an increase from 223 to 238 Wm^{-2}. Figure 4.12(c) shows that the TUSWF also is sensitive to the asymmetry factor which is related to the particle size distribution. With other parameters fixed, at a θ_0 of 31.7°, an increase of g value from 0.60 to 0.62 results in a decrease in TUSWF from 220 to 216 Wm^{-2}. From Figure 4.12 (a)-(c), it is clear that the value of TUSWF is sensitive to τ, ω_0, and g of smoke aerosols, although it is most sensitive to τ and ω_0. As expected, the value of TUSWF also is strongly dependent upon the surface albedo, as shown in Figure 4.12(d). With other parameters fixed, at a θ_0 of 31.7°, an increase of surface albedo value from 0.110 to 0.135 increases the value of TUSWF from 219 to 237 Wm^{-2}. Figures 4.12(e)-(f) show only small changes in TUSWF as column water vapor and column ozone amounts are varied. A change in water vapor amount from 20 to 37 kgm^{-2} causes a decrease of TUSWF from 230 to 226 Wm^{-2}. A change in column ozone amount from 1.5 to 2.7 gm^{-2} causes a decrease of TUSWF from 228 to 227 Wm^{-2}. From Figure 4.12 we conclude that the TOA upward SW flux calculations are sensitive primarily to the assumed values of τ and ω_0 as well as to the surface albedo. The surface albedo must be determined to within 5-6% to obtain TUSWF values within 5 Wm^{-2}. The values of τ must be estimated to within 0.2 and values of ω_0 must be estimated to within 0.02 to obtain TUSWF values within 5 Wm^{-2}.

4.5 Instantaneous Shortwave Aerosol Radiative Forcing (SWARF)

The term "radiative forcing" was first used to describe the radiative impact of clouds on the earth radiation budget (Ramanathan et al. 1989; Hartmann et al. 1986). The TOA radiative forcing of clouds at a specific location is defined as the difference of TOA fluxes that occur between clear-sky condition and the case when clouds are found. Therefore, radiative forcing is a measure of how clouds directly change the TOA fluxes compared to clear-sky conditions. ERBE measurements also have been used to estimate the radiative impact of volcanic aerosols (Minnis et al. 1993) and biomass burning aerosols (Christopher et al. 1998). The TOA shortwave radiative forcing (SWARF) of aerosols was defined by Christopher et al. (1998) and are expressed here as:

$$\text{SWARF (TOA)} = S_0^{TOA} [\, \alpha_{clr,TOA} - \alpha_{aer,TOA} \,] \qquad (4.3),$$

where

S_0^{TOA} = incoming solar flux at the TOA,

$\alpha_{clr,TOA}$ = clear-sky albedo at the TOA, and

$\alpha_{aer,TOA}$ = aerosol-sky albedo at the TOA.

Similarly, the downward shortwave aerosol radiative forcing at the surface (SFC) is defined as:

$$\text{SWARF (SFC, downward)} = F_{clr}^{SFC,SW} - F_{aer}^{SFC,SW} \qquad (4.4),$$

where

$F_{clr}^{SFC,SW}$ = clear-sky downward SW flux at the surface,

$F_{aer}^{SFC,SW}$ = aerosol-sky downward SW flux at the surface;

The net downward shortwave aerosol radiative forcing at the surface is defined as:

$$SWARF\ (SFC,\ net) = (F_{clr}^{SFC,SW} - F_{aer}^{SFC,SW})\,[\,1 - \alpha_{SFC}] \qquad (4.5),$$

where

α_{SFC} = surface albedo.

These definitions of radiative forcings for smoke aerosols will be used throughout this study.

CHAPTER 5

RESULTS AND DISCUSSIONS

This chapter presents the results and discussions of several areas investigated in this study. Section 5.1 presents the retrieval of ω_0 values of smoke aerosols over the locations where smoke τ values were obtained from the sunphotometer measurements. Section 5.2 presents the effect of the angular distribution model on the estimation of smoke radiative forcing by examining the difference between the values of instantaneous smoke TOA SWARFs estimated using the SW fluxes from smoke ADMs produced in this study and those estimated using the CERES ES-8 ERBE-like data product in which the SW fluxes are obtained using the ERBE ADMs. Section 5.3 shows the comparison results of surface DSWIs estimated using the modified δ-four stream model with observations during SCAR-B for a limited number of cases. The accuracy of the estimated values of surface DSWI is examined as a function of value of ω_0. Section 5.4 shows the estimated TOA and surface SWARF values of smoke aerosols during the 1998 burning season over South America and Africa.

5.1 Retrieval of ω_0 of smoke aerosols during SCAR-B

Values of ω_0 of smoke aerosols from the AVHRR channel 1 images are retrieved over sites where τ values are available from the sunphotometer measurements during the SCAR-B project in 1995 in South America and the Zambian International Biomass Burning Emission Experiment (ZIBBEE) project in 1997 in Africa. The retrieved values of ω_0 are compared with those obtained from *in situ* measurements and the ground-based measurements wherever they are available. The results are presented in Section 5.1.1. Using the mean values of the retrieved ω_0 over several sites in Brazil and in Africa, the surface DSWIs are estimated using the δ-four stream model and results are compared with the ground-based Eppley pyranometer measurements. The results are shown in Section 5.1.2.

5.1.1 Satellite Retrieval of ω_0

During SCAR-B and ZIBBEE, the loading of smoke aerosols was monitored over several isolated locations using the sunphotometers. By collocating the sunphotometer measurements with the AVHRR measurements over these locations, the ω_0 values of smoke aerosols are retrieved. For a collocated sample, the time difference between the sunphotometer measurement and the AVHRR observation is within 15 minutes and the spatial difference is

within 0.02° in latitude and longitude. Table 5.1 shows the 9 sites over South America and Africa, including the latitude and longitude.

In the retrieval process, to minimize the effects of navigational errors, a 3 x 3 array of AVHRR pixels surrounding these sites is used. Three ω_0 values for a given location are calculated using the mean value (μ) and the mean ± standard deviation ($\mu \pm \sigma$) of the observed channel 1 reflectances in the 3 x 3 array. The smoke ω_0 values are retrieved for each set of collocated AVHRR and sunphotometer measurements over all sites. Due to the difference in spatial resolution between satellite and ground-based instruments, the scene identified by the ground-based instruments may be different from the one inferred from the satellite. For example, while the sunphotometer, due to its narrow field of view, may report a value of aerosol optical thickness, the satellite pixel, due to its larger

Table 5.1 The latitude, longitude and continent for each site where sunphotometer instrument locates.

Site	Continent	Location (Latitude, Longitude)
Alta_Folresta	South America	(-9.92, -56.00)
Ariqiums	South America	(-9.89, -63.00)
Cuiaba	South America	(-15.50, -56.00)
El_Refugio	South America	(-14.75, -62.03)
GORDE_rest	South America	(-15.40, -55.98)
Ji_Parana	South America	(-10.85, -61.79)
Pantanal	South America	(-16.38, -56.62)
Potosi_Mine	South America	(-9.27, -62.86)
Uberlandia	South America	(-18.89, -48.27)
Mongu	Africa	(-15.25,23.15)
Sananga	Africa	(-16.11, 23.30)
Zambe	Africa	(-13.53, 23.10)

footprint may be partially filled with clouds. Since cloud reflectances are usually larger than the reflectances for smoke aerosols, the observed reflectance for a partially cloudy scene will most probably be larger than that for smoke aerosols. As a result, the retrieved ω_0 value for smoke aerosols will be over-estimated. If the reflectance from the cloud contribution is significant, we may fail to retrieve the ω_0 value for the pixel.

Figures 5.1(a) and (b) show the time series of retrieved ω_0 at 0.64 μm over Alta Floresta and Cuiaba Brazil, respectively, during SCAR-B. Figures 5.1(a) and (b) also show as vertical line the range of retrieved ω_0 values corresponding to the ($\mu \pm \sigma$) values in the 3 x 3 array. For a total of 17 out of 27 days over Alta Floresta and 10 out of 33 days over Cuiaba, the values of ω_0 are retrieved within the range of 0.66 to 1.0, with most of the values being in between 0.76 and 0.91, a typical range for aged smoke aerosols obtained during SCAR-B (Reid et al. 1998a, 1999). The mean ω_0 values over Alta Floresta and Cuiaba are 0.87 and 0.84, respectively, as shown by the horizontal lines. Except for several points in Figures 5.1(a) and (b), the retrieved values of ω_0 are consistent and within 0.04 of the mean values, indicating that the ω_0 values of smoke aerosols do not change significantly during the burning season. This is consistent with the findings of Reid et al. (1999). However, for about 35% of the days over Alta Floresta and 70% of the days over Cuiaba, the algorithm fails to retrieve the ω_0 values. For most of these days, the observed AVHRR channel 1 reflectances are over 0.30, which are probably due to cloudy conditions. The failure to

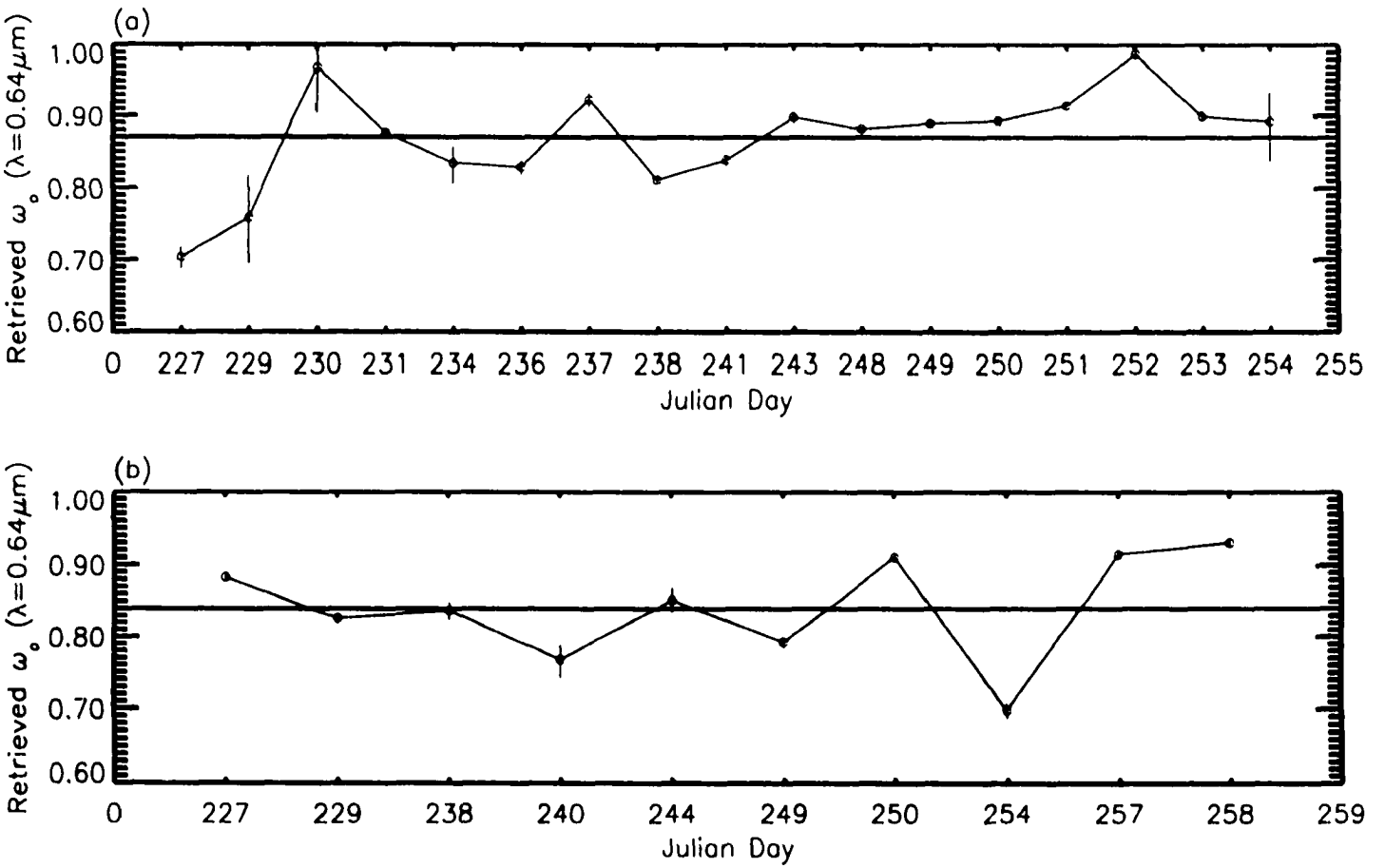

Figure 5.1 AVHRR retrieved ω_0 over (a) Alta Floresta and (b) Cuiaba Brazil during SCAR-B. The vertical lines represent the range of ω_0 retrieved using $\mu+\sigma$ and $\mu-\sigma$ values. The horizontal lines represent the mean ω_0 values

retrieve ω_0 on these days is probably caused by navigational errors and/or differences in spatial resolution between the collocated sunphotometer measurements and satellite measurements, since sunphotometer measurements indicate that the sun is unobscured by clouds for these cases while satellite measurements suggest cloud-contamination. For example, on Julian day 259 (September 18) over Alta Floresta, the channel 1 albedo is 0.45, suggesting that the AVHRR pixel is cloudy. The mean τ values over Alta Floresta and Cuiaba are 1.56 and 0.83, respectively. As shown in Section 4.3, when τ values are small, the retrieval of ω_0 is sensitive to TOA clear sky albedo and observed albedo, as well as τ. The uncertainties in these parameters may cause errors in the retrieval process when τ is small.

The uncertainties in retrieved ω_0 values depend upon the uniformity of the scene, as indicated by the σ value of the 3 x 3 array. For example, over the Alta Floresta on day 229, the μ and σ values of channel 1 reflectance are 0.127 and 0.015, respectively. For the observed τ value of 0.5, the retrieved values of ω_0 range from 0.67 to 0.79. An uncertainty in channel 1 reflectances of 0.03 causes uncertainties in retrieved ω_0 values of 0.12 for τ of 0.5. Uncertainties in retrieved ω_0 values also are a function of aerosol optical thickness. On day 254, the μ and σ values of channel 1 reflectances are 0.187 and 0.033, respectively. For an observed τ value of 1.7, the retrieved values of ω_0 range from 0.81 to 0.91. An uncertainty in channel 1 reflectance of 0.066 causes an uncertainty in retrieved ω_0 value of 0.10 for τ value of 1.7. The larger the τ, the smaller the uncertainty in

the retrieved ω_0 value. Therefore, with the same value of σ, the retrieved ω_0 value is more reliable when the τ value is larger.

During SCAR-B, the UW C131-A aircraft made measurements over Brasilia, Cuiaba, Porto Velho, and Maraba, and aerosol values of ω_0 at 0.55 μm were obtained using three different methods (Reid et al. 1998c). The values of ω_0 at 0.55 μm also were retrieved from the ground-based photosynthetically active radiation (PAR) measurements together with sunphotometer measured τ over selected sites (Eck et al. 1998). For Cuiaba on August 27, the satellite retrieved value of ω_0 at 0.55 μm is compared to ω_0 values obtained from *in situ* measurements (Reid et al. 1998c) and from ground-based PAR measurements (Eck et al. 1998). However, there exists a lack of exact time coincidences for the three measurements. The AVHRR measurement was obtained at 1644 UTC and the *in situ* measurements were taken at about 2000 UTC. The satellite retrieved value of ω_0 was 0.85, while the value of ω_0 from the *in situ* measurement was 0.83 and ground-based measurement also provided a value of 0.83. The satellite retrieved mean value of ω_0 at 0.55 μm over Cuiaba is 0.85, averaged over a total of 10 days, and the mean value of ω_0 obtained from the series of C131-A measurements was also 0.85. However, the standard deviation of ω_0 retrieved from satellite observations is 0.07, as compared to only 0.02 from the *in situ* measurements. The values of ω_0 retrieved from PAR measurements ranges between 0.82 and 0.84.

Since Porto Velho(9°S, 64°W) is geographically close to Potosi Mine (9.27°S, 62.86°W), and the two sites have the same surface scene type of forest, the retrieved ω_0 values in Potosi Mine were compared with those obtained from the *in situ* measurements over Porto Velho, even though there are only three satellite retrieved ω_0 values available at this site from September 4 to 6. The AVHRR retrieved mean value of ω_0 at 0.55 μm is 0.93 with standard deviation of 0.05, while the mean *in situ* retrieved ω_0 value over Porto Velho is only 0.86 with standard deviation of 0.05 from a total of 21 measurements. Therefore the average value retrieved from the satellite observations is about 0.07 higher than that obtained from *in situ* measurements. For a τ of 0.7 (0.64 μm), this discrepancy may cause the values of instantaneous DSWI to be overestimated by about 20 to 30 Wm^{-2} compared to the ones using ω_0 values derived from the *in situ* measurements (Christopher et al. 2000). In terms of possible errors, note that the comparisons of ω_0 are not for exactly the same geographical locations and dates. Comparisons of retrieved ω_0 values between satellite observations and ground-based observations are done over Potosi Mine. The retrieved ω_0 values from ground-based PAR measurements range from 0.85 to 0.92 during the time period from September 4 to 7 (Eck et al. 1998). The mean value of retrieved ω_0 from AVHRR is 0.93, about 0.04 larger than that obtained from ground-based measurements.

Table 5.2 summarizes results of the retrieved values of ω_0 over 6 selected sites in South America and Africa. Results are not shown in Table 5.2 for the

Table 5.2 Statistics of the aerosol optical thicknesses from sunphotometer measurements and AVHRR retrieved ω_0 at 0.64 μm over 6 sites. The values of ω_0 at 0.55 μm are also given which are scaled from the retrieved values of ω_0 at 0.64 μm using wavelength dependency of ω_0 from the MIE calculation.

Site	Samples	τ (0.64 μm)		Retrieved ω_0 (0.64 μm)		Scaled ω_0 (0.55 μm)	
		μ	σ	μ	σ	μ	σ
Alta_Floresta	17	1.55	0.56	0.87	0.07	0.88	0.07
Cuiaba	10	0.83	0.31	0.84	0.07	0.85	0.07
El_Refugio	9	1.22	0.40	0.86	0.08	0.87	0.08
Ji_Parana	5	1.99	0.28	0.91	0.01	0.92	0.01
Mongu	7	0.64	0.22	0.84	0.05	0.85	0.05
Zambe	9	0.58	0.12	0.81	0.07	0.82	0.07

other sites due to small sample size (less than 4). For 56 out of 111 sets of data over the 6 sites, the ω_0 values are successfully retrieved. For each site, the total number of retrieved ω_0 values, the mean and standard deviations of the observed aerosol values of τ, and the mean and standard deviations of the retrieved ω_0 values at 0.64 μm are given in Table 5.2. To facilitate comparisons with ω_0 values obtained from the *in situ* and ground-based measurements during SCAR-B, AVHRR retrieved values of ω_0 at 0.64 μm are scaled to values at 0.55 μm, also shown in Table 5.2. The mean ω_0 value ranges from 0.82 to 0.92 at 0.55 μm over the 6 sites, with standard deviations being within 0.08.

In situ aircraft measurements during SCAR-B show that the physical and optical properties of smoke particles are correlated so that if one physical or optical property of smoke aerosols is determined, other properties can be derived (Reid et al. 1999). The relationship is established between the multi-wavelength

Angstrom exponents (α) determined from the sunphotometer measurements and the ω_0 obtained from insitu aircraft measurements during SCAR-B (Reid et al. 1999). The ω_0 values retrieved from AVHRR are compared with those derived from sunphotometer measurements using the relationship between α and ω_0. From Table 5.2, the mean value of ω_0 (0.55 μm) is 0.88±0.07 for a total of 17 samples over Alta Floresta. The mean value of ω_0 (0.55 μm) derived from sunphotometer measurements is 0.86±0.02 for this site (Reid et al. 1999). The retrieved value of ω_0 from AVHRR is slightly larger than that derived from sunphotometer measurements with larger standard deviation. Over Cuiaba, the mean value of ω_0 is 0.85±0.07 for a total of 10 samples and the mean value of ω_0 derived from sunphotometer measurements is 0.85±0.02. The retrieved mean value of ω_0 from AVHRR matches with that from sunphotometer measurements with larger standard deviation. Over Ji Parana, the mean value of ω_0 is 0.92±0.01 for a total of 5 samples and the mean value of ω_0 derived from sunphotometer measurements is 0.87±0.01. The retrieved mean value of ω_0 from AVHRR is over-estimated by 0.05 compared to the value from sunphotometer measurements. Note that in this study, the value of ω_0 decreases with increasing wavelength, based on Mie calculations. For the case that ω_0 of smoke aerosols increases with wavelength, the retrieved ω_0 value will be smaller than that retrieved using the look-up table.

5.1.2 Aerosol attenuation of solar flux at surface

The radiative impact of biomass burning aerosols is determined by their optical properties. One of the most important applications of retrieved smoke optical properties is to estimate shortwave radiation budgets, especially at the surface, over the biomass burning regions. In this section, the δ-four stream radiative transfer model is used to calculate the DSWIs using the retrieved ω_0 and observed τ values at the sunphotometer sites. The model calculated DSWIs then are compared with ground-based Eppley pyronometer measurements. There are total of 14 cases from which such comparisons can be made. Eight of them are in Africa, and the rest of them are in South America. Note that the δ-four stream radiative transfer model was discussed in Chapter 3.2. Both ω_0 and τ values are required as input parameters for estimating DSWIs over smoke areas.

Figures 5.2 and 5.3 show the results of model-estimated and observed DSWI comparisons over South America and Africa, respectively. Since the ω_0 values over a site do not change significantly during a burning season (Reid et al. 1999), the mean ω_0 value for a site is used to calculate surface DSWIs. Figures 5.2(a) and (b) show the results over Cuiaba on August 27 and September 1, 1995, respectively. The mean ω_0 value over Cuiaba at 0.64 μm is 0.84 (0.85 at 0.55 μm) as shown in Table 5.2. As a result, the root mean square (RMS) errors of surface DSWIs between observations and the model calculations are 11.0 and 17.3 Wm^{-2}, respectively. The mean and standard deviation of the errors

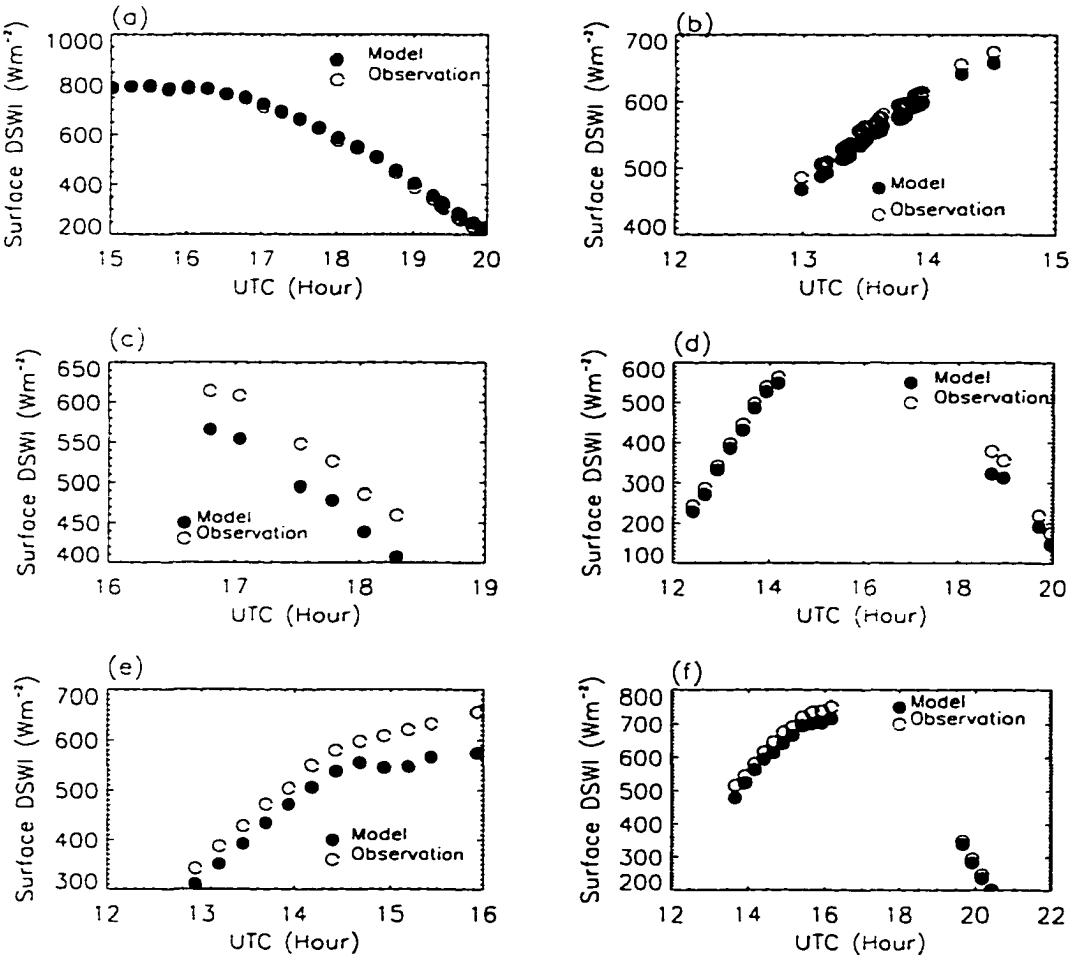

Figure 5.2 Comparison of model-estimated DSWIs with observed DSWIs during SCAR-B in South America. (a) 08/27 over Cuiaba, (b) 09/01 over (c) 08/30 over Pantanal, (d) 09/04 over Potosi Mine, (e) 09/05 over Potosi Mine, and (f) 09/06 over Potosi Mine

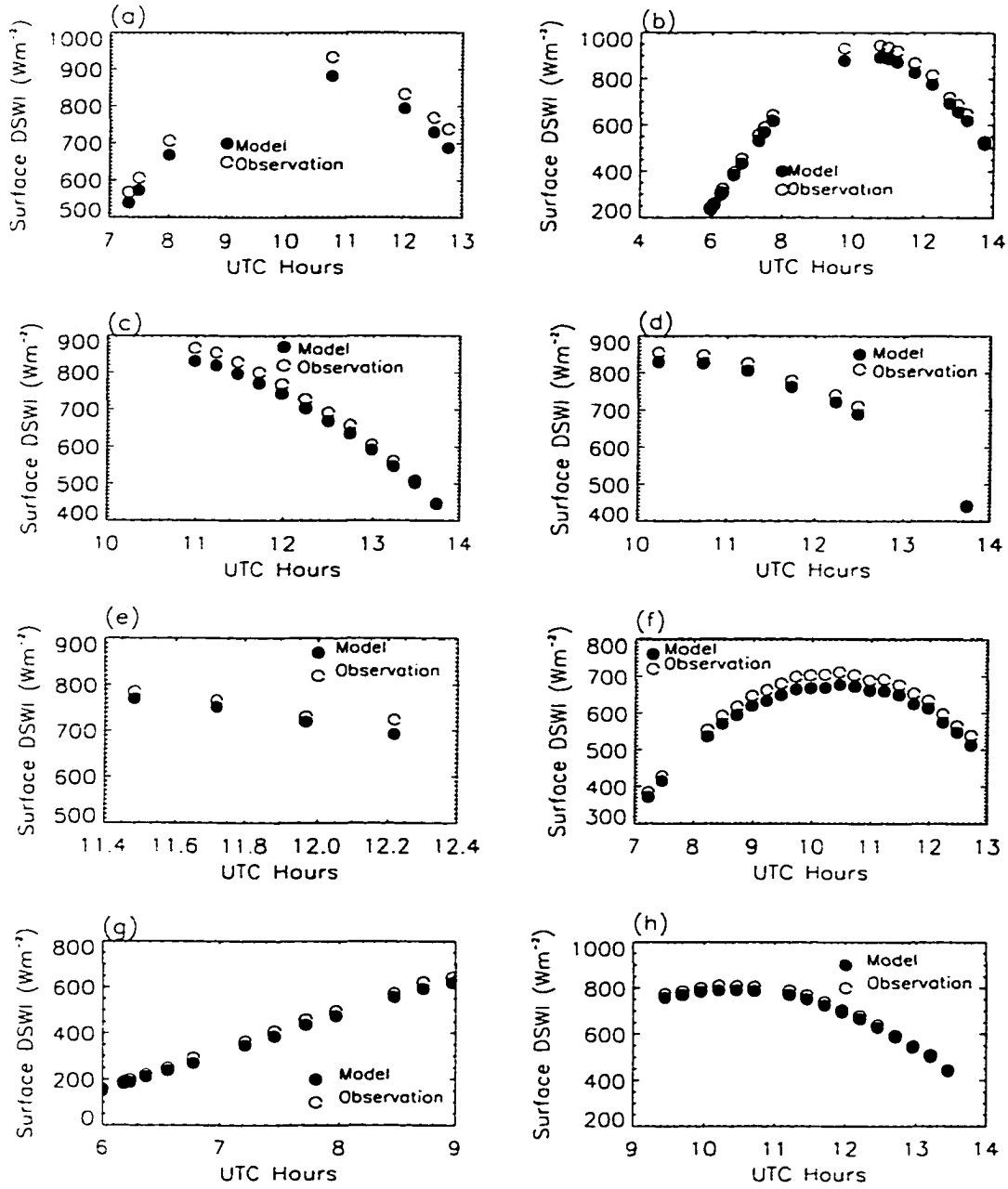

Figure 5.3 Comparison of model-estimated DESWs with observed DSWIs in 1997 over Mongu, Africa on (a) 08/25, (b) 08/26, (c) 08/27, (d) 08/28, (e) 08/30, (f) 08/31, (g) 09/01 and (f) 09/03

between observed fluxes and model estimated fluxes are –8.9±6.4 and 17.3±2.7 Wm^{-2}, respectively. Fig. 5.2(c) shows the results over Pantanal on August 30. The mean retrieved ω_0 value at 0.64 μm over Pantanal is 0.89 (0.90 at 0.55 μm) with standard deviation of 0.06 using a total of 3 samples. In this case, model calculations consistently underestimate the values of DSWI. The mean and standard deviation of the errors between observations and model calculations are 50.6±2.7 Wm^{-2}, and the RMS error is 50.6 Wm^{-2}. However, increasing the assumed value of ω_0 from 0.89 to 0.92 narrows the mean error to within 20 Wm^{-2}. The mean values of τ at 0.64 μm for Figures 5.2(a), (b) and (c) are 0.57, 0.80 and 1.38, respectively.

Figures 5.2(d), (e) and (f) show the results over Potosi Mine on September 4, 5, and 6, respectively. The mean retrieved ω_0 value at 0.64 μm over Potosi Mine is 0.92 (0.93 at 0.55 μm) with standard deviation of 0.05 using a total of 3 samples. From Fig. 5.2(d), the model underestimates the surface DSWIs consistently, with the mean and standard deviation of errors being 21.4±14.1 Wm^{-2}, with the RMS error being 25.6 Wm^{-2}. An increase of the assumed value of ω_0 from 0.92 to 0.93 narrows the mean error to within 20 Wm^{-2}. In this case, a small change in ω_0 of only 0.01 causes a surface DSWI error of about 6 Wm^{-2}; this is the result of the large mean aerosol optical thickness of 1.80. Figure 5.2(e) also shows the underestimation of surface DSWIs by the model. The mean and standard deviation of errors are 48.9±16.8 Wm^{-2}. An increase of the assumed value of ω_0 from 0.92 to 0.95 narrows the mean error to within 20 Wm^{-2}, due to

the large mean aerosol optical thickness. In this case, the mean value of τ is 1.95, so an error of $\omega_0 = 0.03$ can cause a surface DSWI error by about 30 Wm^{-2}. In Figure 5.2(f), the model underestimates the surface DSWIs; the RMS error is 25.8 Wm^{-2} and the mean and standard deviation of errors are 23.5±10.7 Wm^{-2}. The mean value of τ is 1.23. From Figures 5.2(d), (e) and (f), a mean ω_0 value of 0.95 at 0.64 μm can make the model calculations of surface DSWIs match well with observations. Note that a less steeply decreasing trend of ω_0 with λ will also result in agreement between calculated DSWIs and measured DSWIs. The retrieved mean ω_0 value at 0.64 μm is 0.92 (0.93 at 0.55 μm), about 3-4% smaller than the one indicated from the surface DSWI measurements.

Figures 5.3(a)–(h) show the comparison of results on August 25-28, August 30-31, September 1, and September 3, respectively, over Mongu, Africa during the ZIBBEE experiment. The mean retrieved ω_0 values at 0.64 μm are 0.84 (0.85 at 0.55 μm), as shown in Table 5.2. The RMS errors for the eight days are 40.7, 31.6, 24.2, 19.7, 19.8, 27.1, 18.2, and 14.1 Wm^{-2}, respectively, and the mean and standard deviation of errors are 39.9±7.8, 27.4±10.6, 21.7±10.7, 17.9±8.2, 18.2±7.8, 26.2±6.7, 16.9±6.9, and 13.0±5.4 Wm^{-2}, respectively, for these eight days. The corresponding mean values of τ for the eight days are 0.15, 0.15, 0.34, 0.36, 0.44, 0.84, 0.83, and 0.57, respectively. From Figure 5.3, the largest RMS error is about 40 Wm^{-2}, with the mean RMS error for the 8 cases being about 25 Wm^{-2}. The radiative transfer calculations, as

shown in Figures 5.3 (a)-(h), suggest that the mean ω_0 value for smoke aerosols retrieved over Mongu from AVHRR images is slightly underestimated.

Through the comparisons of surface DSWIs between model calculations and observations, as shown in Figures 5.2 and 5.3, it is seen that for 10 out of 14 cases, the mean errors between observations and model calculations are within 30 Wm^{-2}, with the largest error of 51 Wm^{-2}. The model can either underestimate or overestimate the surface DSWIs, depending on the accuracy of the retrieved ω_0 values.

Figures 5.2 and 5.3 suggest that retrieved ω_0 values from AVHRR are slightly underestimated. The errors of estimated surface DSWIs also are strongly dependent on the aerosol optical thicknesses. These comparisons suggest that the retrieved ω_0 values from AVHRR measurements can be used to estimate the instantaneous surface DSWIs over biomass burning regions to within an accuracy of about 30 Wm^{-2}.

5.2 Smoke ADM and the estimated instantaneous smoke SWARF

The smoke ADM is calculated using the SBDART model, as described in Section 4.3. This smoke ADM then is used to convert the CERES measured SW radiances into the TOA SW fluxes for smoke footprints. The selected Level 1B

VIRS images listed in Table 4.1 are collocated with the corresponding CERES ES8 products for August 1998, and then the CERES SW radiances are converted into the TOA SW fluxes using the smoke ADM for all smoke samples (a collocated sample is labeled as smoke sample if the percentage of the identified VIRS smoke pixels within the CERES footprint is larger than 90%). The collocation procedures are discussed in Section 2.4. The converted SW fluxes for smoke samples then are compared with the TOA SW fluxes from the CERES ES8 ERBE-like data product. Differences in the estimated instantaneous SWARF of smoke aerosols using these SW fluxes also are examined. Section 5.2.1 shows the comparison results and discussions. The smoke ADM is also compared with the ERBE ADM, and the results are shown in Section 5.2.2.

5.2.1 TOA SW fluxes from the smoke and ERBE ADMs

For the smoke pixels detected from the VIRS images, aerosol optical thicknesses are retrieved from the VIRS channel 1 images using the table look-up approach presented in Section 4.2. The τ values are retrieved from the VIRS channel 1 images using the same procedure as the ones retrieved from the AVHRR channel 1 images (Li et al. 1999). To retrieve τ, the aerosol ω_0 values are assumed, based on the surface types defined in the International Geosphere-Biosphere Programme (IGBP). The IGBP has a total of 18 surface types,

covering different vegetation surfaces over land, ocean, and ice (Belward and Loveland 1996). The instantaneous SWARF of smoke aerosols over the surface types of forest, savanna, grassland, wetland, mixed forest and cropland are examined in this section. The ω_0 values at the wavelength of 0.55 μm for the surface types of forest, savanna, grassland, and wetland are assumed to be 0.88, 0.86, 0.92 and 0.89, respectively, which are the mean ω_0 values for the corresponding surface types retrieved from the AVHRR imagery during SCAR-B (Li et al. 1999). For the other surface types, the ω_0 value of 0.88 at 0.55 μm is assumed, a typical value obtained during SCAR-B (Reid et al. 1998b).

Surface albedo is a key parameter in both the look-up table for the smoke τ retrieval and in the application of the smoke ADM. Since the clear-sky albedo at the TOA can be directly estimated from the satellite observations, the SBDART model is used to calculate the relation between TOA albedo and surface albedo under clear-sky conditions assuming the standard tropical atmosphere (McClatchey et al. 1972). The result is that the TOA clear-sky albedo determined from satellite measurements can be directly used.

The VIRS channel 1 TOA clear-sky albedo map is determined as following. The study area is first divided into 4 x 4 km grids. The clear sky albedo is determined by assigning the minimum R1 value obtained from all pixels falling into this grid. All VIRS data files in August 1998 are used to obtain this clear-sky albedo map.

The broadband TOA clear-sky albedo map is determined in three steps. First, the study area is also divided into 20 x 20 km sections. If the percentage of clear-sky pixels for a collocated VIRS-CERES sample is greater than 90%, we assume that this collocated sample is a clear-sky sample. The broadband TOA clear-sky albedo for a grid is determined to be the minimum value of broadband TOA albedos for all clear-sky samples in August which fall into this grid. The broadband TOA albedo for a sample is determined as the ratio of CERES ES8 ERBE-like SW fluxes to the downward broadband SW fluxes at this solar zenith angle. Second, if there are no clear-sky samples available for a grid, the TOA albedo for the grid is obtained by averaging the TOA clear-sky albedo at the four neighbors of this grid. Third, if the clear-sky albedos are not available for the four neighbors, the TOA clear-sky albedo for the grid is assigned as a value based on the IGBP surface type. The mean clear-sky albedo for each of the IGBP surface types is calculated from all clear-sky samples detected in August, 1998. The broadband TOA clear-sky albedos for the 6 surface types of forest, savanna, grassland, and wetland, mixed forest and cropland are shown in Table 5.3.

For each of the collocated samples, the smoke, cloud and clear-sky percentages are calculated. A sample is labeled as a smoke sample if the smoke percentage is over 90% within the CERES footprint, and the smoke τ value is retrieved using the mean value of VIRS channel 1 reflectance for this footprint. A total of 23783 collocated data samples are labeled as smoke samples from the 14 VIRS images investigated, and 20156 of the samples are

Table 5.3 The mean broadband TOA clear-sky albedo, the statistics for the retrieved τ, estimated smoke TOA SWARF using smoke ADMs and ERBE ADMs, and TOA SWARF per optical thickness, and the number of samples for the statistics for the 6 surface IGBP types. Flux unit: Wm^{-2}.

Surface types	Mean α_{TOA}	# of sample	τ (0.64μm)		Model SWARF		CERES SWARF		SWARF / τ	
			μ	σ	μ	σ	μ	σ	Model	CERES
Forest	0.145	6211	1.51	0.64	-54.1	23.0	-49.5	22.7	-35.8	-32.8
*M Forest	0.159	476	0.98	0.56	-35.5	23.3	-41.1	19.8	-36.2	-41.9
Savanna	0.144	7234	1.36	0.70	-40.5	24.2	-38.4	20.7	-29.8	-28.2
Grassland	0.144	3454	0.75	0.46	-32.5	28.7	-34.3	26.0	-43.3	-45.7
Wetland	0.149	1125	0.90	0.34	-46.6	24.5	-47.9	27.8	-51.8	-53.2
Cropland	0.159	365	0.62	0.32	-35.1	23.9	-44.3	23.6	-56.6	-71.5

*M Forest stands for mixed forest in the IGBP surface map.
Model SWARF means the TOA SWARF calculated using smoke ADMs
CERES SWARF means the TOA SWARF calculated using CERES ERBE-like data product.

retrieved with τ values between 0.1 to 3.5, which is the range of our look-up table. For the total of 23783 smoke samples, over 58% of the samples are identified as clear over land in the CERES ES8 ERBE-like data product and over 39% are identified as partly cloudy over land. Therefore, almost all smoke samples are identified as clear and partly cloudy, and the corresponding ERBE ADMs are used to convert the measured radiance into TOA fluxes in the CERES ES8 ERBE-like product.

Using the assumed ω_0 values based on the ecosystem and the retrieved τ values, the TOA upward SW fluxes are calculated for each of the smoke samples using the SBDART model. The smoke optical properties used in the model are

the same as the ones shown in Section 4.4. The model-estimated values then are compared with the values measured from the CERES instrument. Figure 5.4 shows the scatter plot of the CERES radiances versus the model-estimated TOA upward radiances for smoke samples. From Figure 5.4, it is seen that with the retrieved τ values and assumed ω_0 values, the model-calculated TOA upward radiances are in good agreement with the observations. The correlation between model values and observed values is 93%. The mean and standard deviation of the absolute difference are 2.5 and 5.5 Wm^{-2}, respectively. The mean and standard deviation of the relative difference ((model – observation) / observation) are 8.5% and 15.3%, respectively, and the RMS error is 6.1 Wm^{-2}. This result suggests that smoke optical properties are properly characterized in the SBDART model for broadband radiative transfer, as presented in Section 4.5. As a result, the smoke ADM produced using this model is expected to be properly estimated.

For each smoke sample, the TOA SW flux also is estimated using the measured CERES SW radiances and the smoke ADM. Figure 5.5 shows the scatter plot of the ES8 ERBE-like SW fluxes versus the SW fluxes converted using the smoke ADM. From Figure 5.5, the correlation is over 96%. The mean difference between the model-estimated fluxes and the ERBE-like fluxes is 0.48 Wm^{-2} with standard deviation of 12.7 Wm^{-2}. The RMS error is 12.7 Wm^{-2}, and the relative mean difference is 15%. Therefore, based on the 14 VIRS data files, there is almost no bias between the model-estimated TOA SW fluxes and the

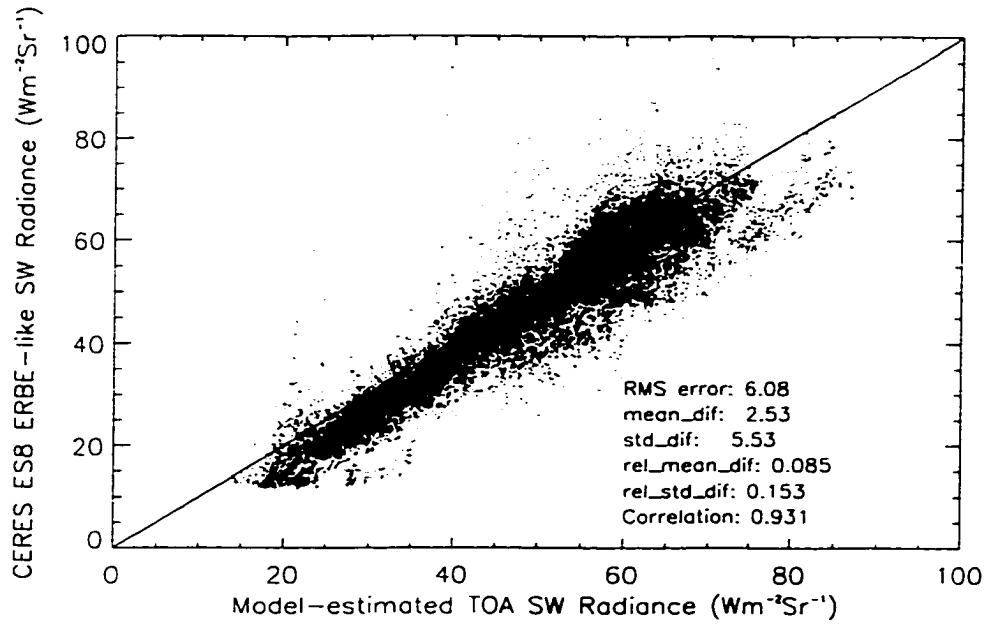

Figure 5.4 Scatter plot of CERES ES8 SW radiances versus the model-estimated SW radiances for the identified smoke samples

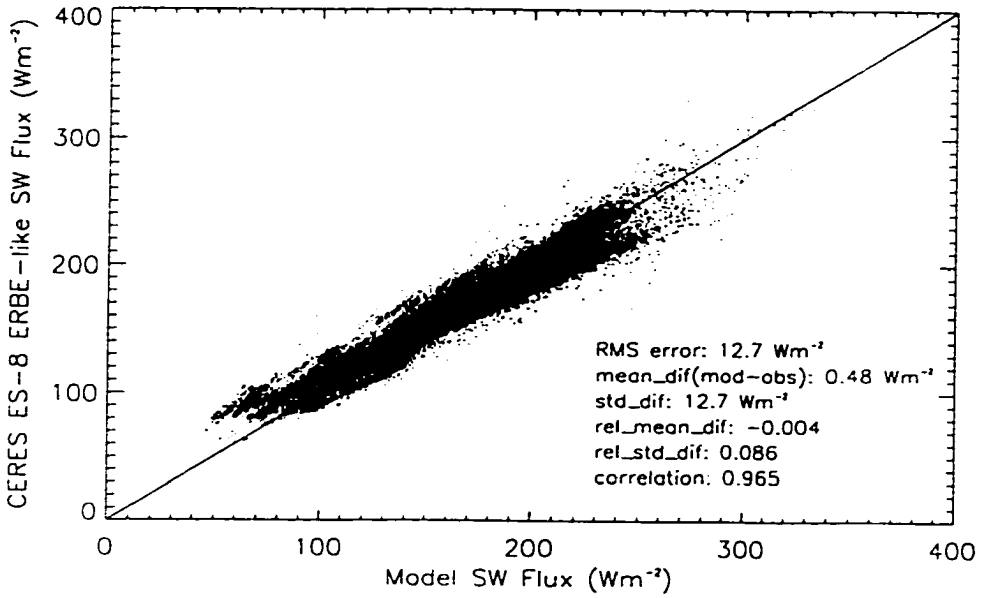

Figure 5.5 Scatter plot of CERES ES8 SW fluxes versus the model-estimated SW fluxes for the identified smoke samples

ERBE-like SW fluxes. This result suggests that on the average, the ERBE ADMs work well in the conversion from measured radiances to TOA SW fluxes.

For all the smoke samples, values of instantaneous smoke SWARF are calculated and grouped, based upon the IGBP surface types. The definition of TOA SWARF of smoke aerosols was given in Section 4.5. Table 5.3 shows the instantaneous smoke TOA SWARFs for the major surface types over the area of study. The TOA SWARF values estimated using the SW fluxes converted from the ERBE ADMs and smoke ADMs for each surface type are given. The mean and standard values of retrieved τ, and the TOA SWARF per unit optical thickness also are given in Table 5.3. For the forest surface type, the mean value of the TOA SWARF using the smoke ADMs is about 5 Wm^{-2} larger than that using the ERBE ADMs. The relative difference is about 9%. For the grassland surface type, the mean value of the TOA SWARF using the smoke ADMs is about 2 Wm^{-2} smaller than that using the ERBE ADMs. The relative difference is about 6%. For the cropland surface type, the mean value of the TOA SWARF using the smoke ADMs is about 9 Wm^{-2} smaller than that using the ERBE ADMs, and the relative difference is over 20%. The TOA SWARFs over the six surface types range from –32 Wm^{-2} to –55 Wm^{-2}, showing that smoke aerosols have a cooling effect. These results are in good agreement with previous studies (Christopher et al. 1996, 1998). The ratio of TOA SWARFs to τ ranges from –29 Wm^{-2} to –57 Wm^{-2}. In general, differences of smoke TOA

SWARF values estimated using the smoke ADM and using the ERBE ADMs are within 10 Wm^{-2}. The relative differences are within 10%.

5.2.2 Comparison of Smoke ADM with ERBE ADM

Since most of smoke-occupied CERES footprints are classified as either clear or partly cloudy in the ES8 ERBE-like data product, we compare the smoke ADMs with two ERBE ADMs: for solar zenith angle of 60° clear over land as shown in Figure 5.6(c), and partly cloudy over land as shown in Figure 5.6(d). Figures 5.6(a) and (b) are calculated smoke ADMs assumed τ values of 0.36 and 1.8, respectively. The assumed value of ω_0 at 0.64 μm is 0.85 and the assumed surface albedo is 0.15. Although the ranges of ADM values are similar between smoke ADMs and ERBE ADMs, the patterns of the two types of ADMs are different. The ERBE ADMs are more sensitive to azimuth-angle. The ERBE clear ADM (Figure 5.6(c)) has larger ranges of values in the forward and backward scattering angles than that for smoke ADM at τ value of 0.36. Comparison of Figures 5.6(b) and 5.6(d) shows that the range of smoke ADM values is larger than that of the ERBE ADM in the forward scattering direction, and is smaller than that of the ERBE ADM in the backward scattering direction. The mean absolute difference between the ADMs in Figures 5.6(a) and 5.6(c) is 0.102, and the relative difference is 10.3%. The mean absolute difference

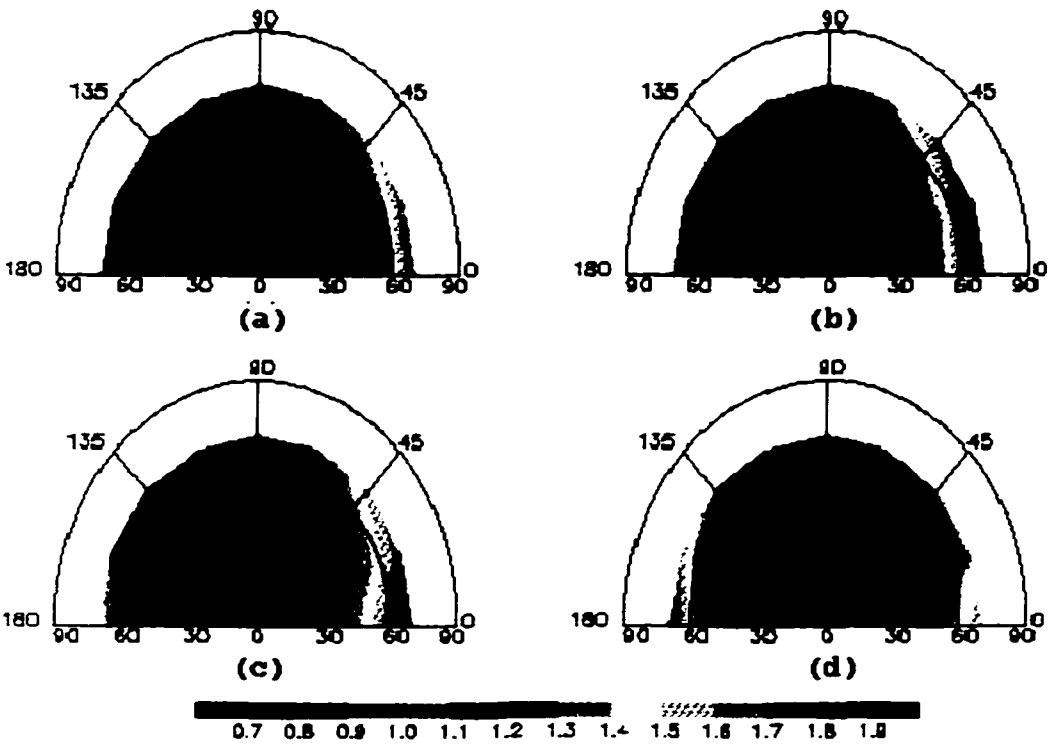

Figure 5.6 (a) Smoke ADM with τ =0.36, ω_0=0.85, and α_s=0.15, (b) Smoke ADM with τ =1.8, ω_0=0.85, and α_s=0.15, (c) ERBE ADM with clear over land and (d) ERBE ADM with partly cloudy over land. Solar zenith angle is 60°

between the ADMs in Figures 5.6(b) and 5.6(d) is 0.101, the relative difference is 9.8%.

5.3 Validation of modified δ-4 stream model for smoke aerosols

In Section 5.3.1, the modified δ-4 stream model is validated using two cases in which both τ and ω_0 values of smoke aerosols are available from the observations during SCAR-B (these are called the "control cases"). There are another five cases in which τ values are available but ω_0 values have to be assumed to estimate the surface DSWIs. These are called "validation cases". Table 5.4 lists the locations and times for the case studies. The model-estimated DSWIs are compared with the surface observations during the SCAR-B experiment, and results are shown in Section 5.3.1. Section 5.3.2 shows how the assumed ω_0 values can affect the estimated surface DSWI estimations.

5.3.1 Comparison between measured and calculated DSWI values

There are two cases during SCAR-B in which the observed DSWI values from the Eppley pyranometer, column optical thicknesses at seven wavelengths from the sunphotometer, as well as profiles of temperature, pressure, dew point temperature, potential temperature, smoke extinction coefficient and vertical

profiles of ω_0 are available. These are called the "control cases" because the two most important parameters (τ and ω_0) are available for surface DSWI estimation and comparison with ground-based observations. The two cases are on August 27 and September 1, 1995 at Cuiaba. However for September 1, 1995 the *in situ* measurements of ω_0 are from Pantanal which is about 100 km from Cuiaba.

Figures 5.7(a) and 5.7(b) show the calculated values of DSWI from the four-stream radiative transfer model and the observed DSWI values from the Eppley pyranometer for August 27 and September 1, 1995, over Cuiaba. The open circles represent the measured DSWI values and the '+' symbols denote the model calculated values. Also shown by the solid circles are the measured

Table 5.4 Details of locations and times for the case studies. See Figure 1 for location of sites. Surface measurements denote both the sunphotometer and the Eppley pyranometer measurements

No	Location	Date 1995	C131-A Flight Number	C-131A Profile Time (UTC)	Surface measurements (UTC)
1	Cuiaba	08/27	1694(Cuiaba)	1633-2027	1500-2000
2	Cuiaba	09/01	1697(Pantanal)	1206-1445	1300-1430
3	Pantanal	08/30	Not applicable	Not applicable	1200-1800
4	Potosi Mine	09/04	Not applicable	Not applicable	1200-2000
5	Potosi Mine	09/05	Not applicable	Not applicable	1200-2000
6	Potosi Mine	09/06	Not applicable	Not applicable	1600-1800
7	Potosi Mine	09/07	Not applicable	Not applicable	1300-1600

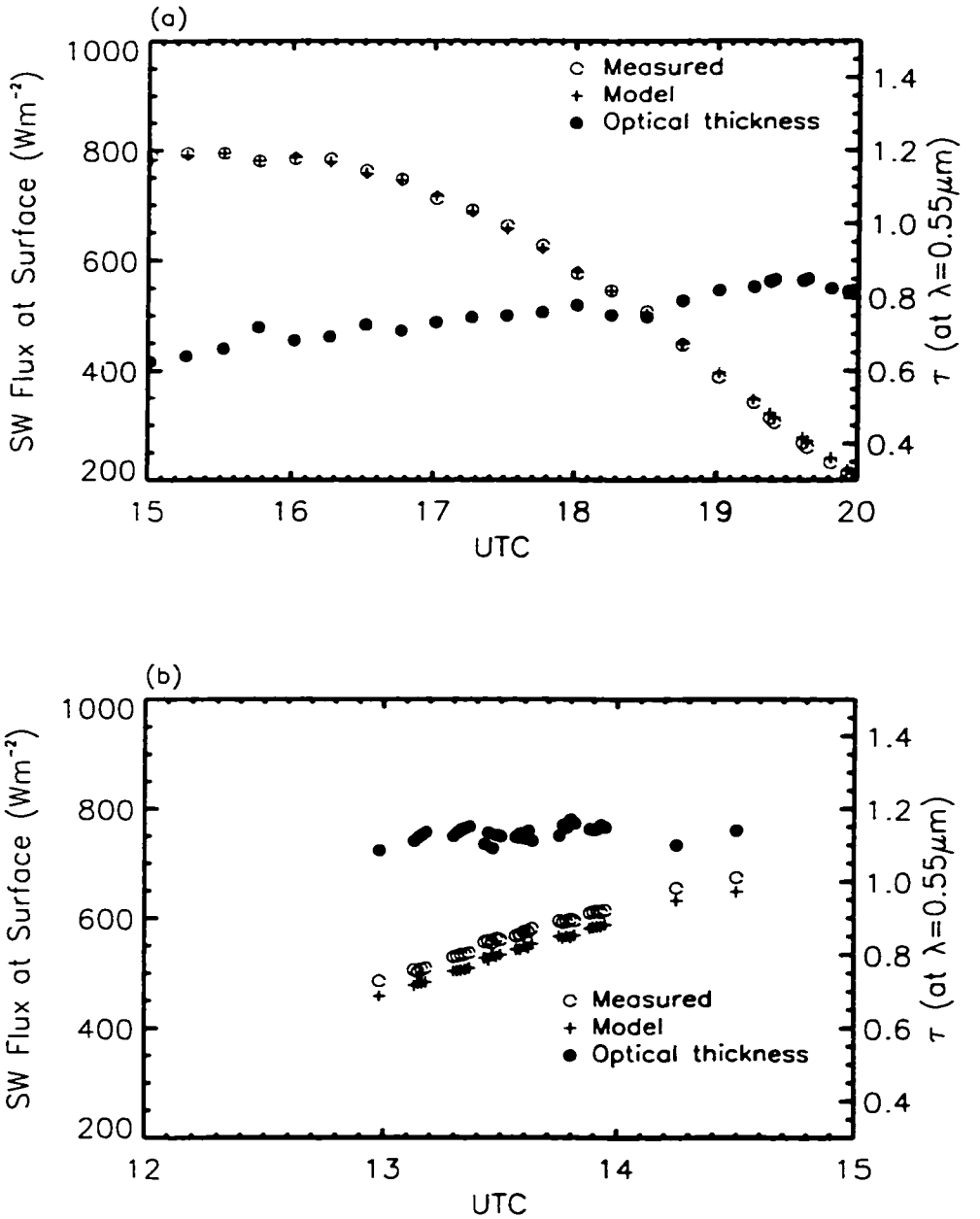

Figure 5.7 Comparison between measured (open circles) and calculated DSWI (+sign) for a)August 27, 1995 over Cuiaba, and b) September 1, 1995 over Cuiaba as a function of UTC time. Also shown in solid circles are the measured aerosol optical thickness at 0.55 μm

values of τ at 0.55 μm. Figure 5.7a shows that on August 27 over Cuiaba the DSWI values change between 800 to about 200 W m^{-2} from 1500 UTC to 2000 UTC. Note that on this day, the C-131A measurements were made between 1633-2027 UTC. Six overpasses were made over the sunphotometer site, and uniform thick smoke was observed during the time of the C131-A measurements (Kaufman et al. 1998). During this day, fires and smoke were also observed from satellite measurements over much of this region (Prins et al. 1998). Figure 5.7a shows that during this time the sunphotometer measured τ values at 0.55 μm (solid circles) that varied from 0.6 to 0.8, with peak values between 19 - 20 UTC. The calculated DSWI values are in excellent agreement with the pyranometer measurements for this day. The root-mean-square (RMS) difference between observed and calculated values for 25 sets of measurements is 6.2 W m^{-2} for August 27, and the mean bias error (observed-calculated) is –1.9 W m^{-2}. Figure 5.7b shows similar results over Cuiaba for September 1, 1995. The C-131A measurements were made between 1206-1445 UTC when a thick uniform haze was present (Prins et al. 1998). The sunphotometer and Eppley cloud-free measurements are available only between 1300-1430 UTC. Note the consistently large aerosol optical thickness values around 1.15 compared to values of 0.6-0.8 shown in Figure 5.8a. For the 33 instantaneous measurements, on September 1, 1995, the DSWI values are between 500-650 W m^{-2}. The RMS error between the measured and calculated values is 27.4 Wm^{-2} and the bias error is 27.3 W m^{-2}. From these two cases it is inferred that, given adequate information about the optical and radiative properties of biomass-

burning aerosols, the DSWI values can be calculated to within 30 W m^{-2}. The differences between the measurements and calculations are probably due to: 1) the temporal lack of collocation between the UW C-131A measurements and the sunphotometer measurements; 2) assumptions concerning the wavelength dependency of ω_0 and g; and, 3) the assumption that the C131-A measurements made during a particular time and location are representative of the entire time period.

For the validation cases, only the observed τ and the DSWI measurements are available. Therefore, average values of ω_0 and g are used to calculate the DSWI from the four-stream radiative transfer model. The purpose here is to determine if average values of aerosol properties are adequate for DSWI calculations. Standard water vapor, temperature and ozone profiles for the tropical atmosphere are assumed. The average value of ω_0 at 0.55 μm is 0.823 and g is 0.553; the wavelength dependence of these values is shown in Figure 4.7 (b). Figure 5.8 shows the relationship between observed minus calculated DSWI values as a function of the measured τ at 0.55 μm for all seven days, which includes the both the control and the validation cases. Also shown in Figure 5.8 are the standard deviations in τ and the DSWI values. Table 5.5 shows the RMS errors for each day. The measured τ (0.55 μm) ranges from 0.5 to 2.6 over these sites. As τ increases the differences between the measured and calculated values get larger, with a limiting value of about 150 W m^{-2}. For the two control cases (8/27, 9/01) over Cuiaba where single scattering albedo

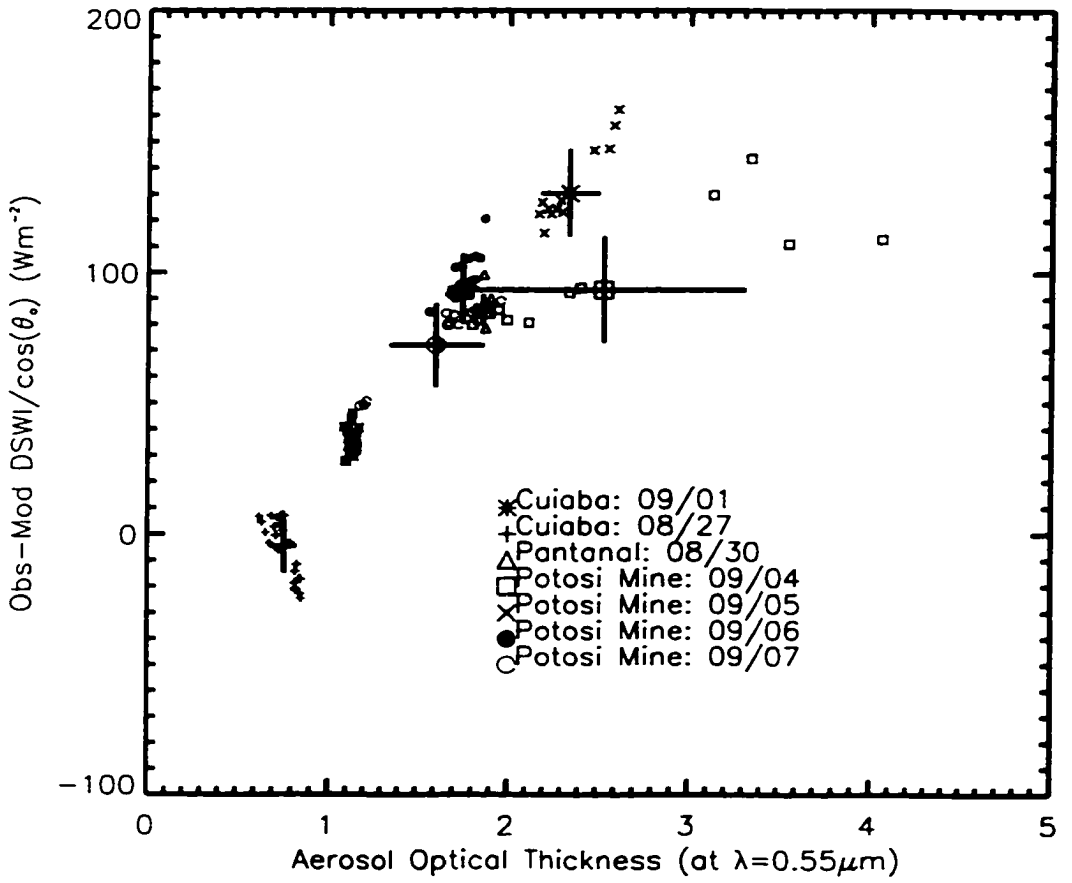

Figure 5.8 Normalized differences between measured and calculated values of DSWI as a function of aerosol optical thickness for all case studies

Table 5.5 Bias (Observed -Calculated) in W m^{-2} and root mean square errors in W m^{-2} for the study

Location	Date	Mean τ_s (0.55 μm)	RMS error	Bias
Cuiaba	08/27/1995	0.76	6.17	-1.86
Cuiaba	09/01/1995	1.13	27.43	27.29
Pantanal	08/30/1995	1.86	69.50	69.44
Potosi Mine	09/04/1995	2.54	67.90	65.78
Potosi Mine	09/05/1995	2.34	113.82	111.11
Potosi Mine	09/06/1995	1.75	80.87	77.60
Potosi Mine	09/07/1995	1.60	54.51	52.08

values were available from *in situ* measurements, the RMS errors are 6.17 and 27.43 W m^{-2} respectively. For the five days when measured values of ω_0 and g were not available, average values were used. The differences between measured and calculated DSWI are a linear function of aerosol optical thickness. As τ (at 0.55 μm) increases the RMS errors also increase. In Section 4.2 we show that to decrease the differences between measured and calculated values, the aerosols would have to be less absorptive (i.e. larger ω_0 values) which would increase the values of DSWI. Therefore, the strategy of assuming average aerosol ω_0 values may not be suitable for radiative transfer studies.

Next we examine the impact of biomass burning aerosols at the TOA from radiative transfer calculations. Unfortunately no broadband measurements were made at the TOA to validate the results. The difference between clear and aerosol conditions is defined as the shortwave aerosol radiative forcing (SWARF) (Christopher et al. 1998). The results shown in Fig. 5.9 are for four major ecosystems in Brazil. The four different ecosystems and their corresponding broadband shortwave clear sky albedos are 1) Forest (10.6 %), b) Mixed Forest (12.9%), c) Savanna (16.6 %) and d) Grassland (14.9%). The SWARF results are shown as a function of aerosol optical thickness at 0.55 μm. These calculations are performed at a solar zenith angle of 45 for a tropical atmosphere. The ω_0 values are assumed to be 0.88 for all ecosystems that are average conditions for regional and aged smoke (Reid et al. 1998b). The wavelength dependence of single scattering albedo is obtained from Figure 2. As τ increases, the SWARF also increases due to the increased reflection from aerosols. For a unit change in aerosol optical thickness (from 0 to 1), the changes in SWARF for the forest, mixed forest, savanna, and grassland ecosystems are about -60, -55, -37, and -43 W m^{-2}, respectively. These changes in SWARF for a unit change in aerosol optical thickness are different for different solar zenith angles, and values of the assumed single-scattering albedo and surface albedo.

Since τ and ω_0 are the two major parameters that affect the calculation of DSWI, as shown in Section 4.4, the assumption of ω_0 has a large impact on the

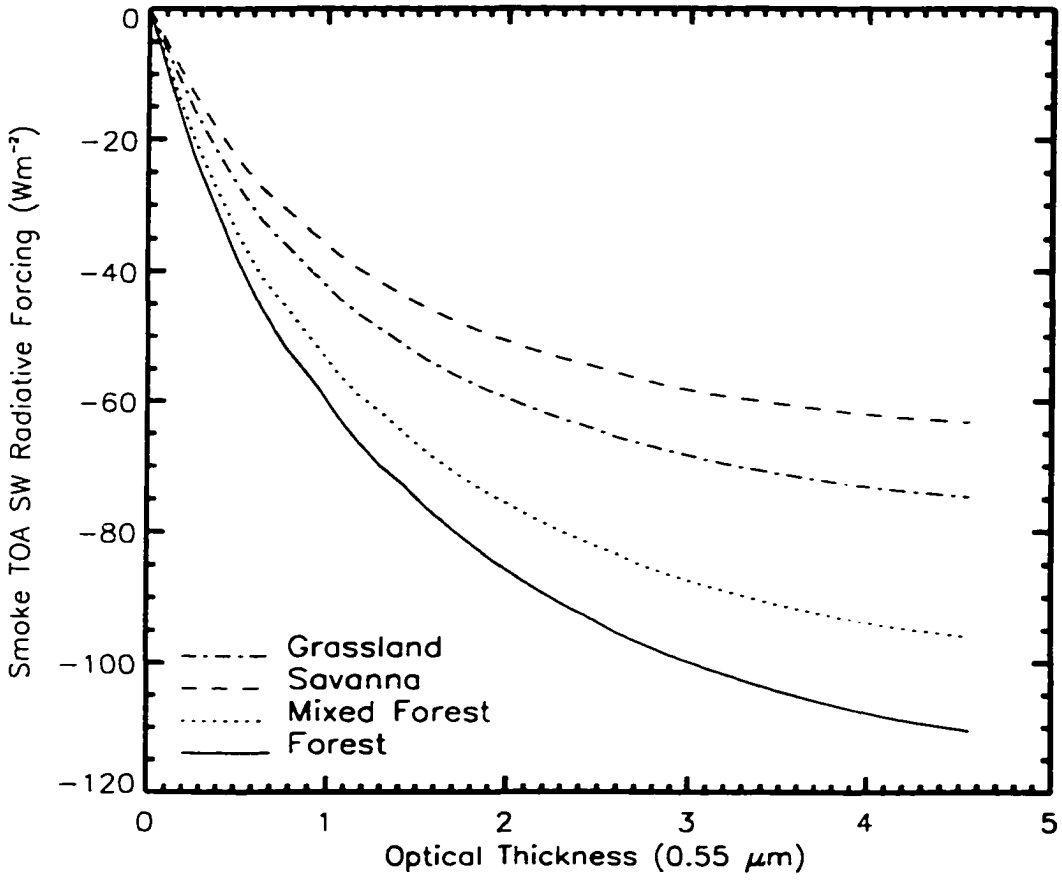

Figure 5.9 Smoke TOA shortwave radiative forcing as a function of optical thickness for four different ecosystems

DSWI values. We will now further examine the data from Potosi Mine on September 5, 1995, where the RMS errors between the measured and calculated values were the largest (113.8 W m^{-2}, see Table 5.5). Since the τ values are obtained from sunphotometer measurements which have a small uncertainty (~0.01), we will assume that ω_0 is the only variable that needs to be adjusted to reduce the RMS errors since the other variables as shown in Fig. 4.11 play a minor role. Figure 5.10a (solid line) shows the ω_0 values as a function of wavelength that produce a RMS error of 113.8 W m^{-2}. The DSWI values at the surface corresponding to this set of ω_0 values are shown in Figure 5.10b (as the '+' symbols). Note that the model underestimates the DSWI values; therefore the ω_0 values need to be increased (to make the aerosols less absorptive and increase scattering) to produce higher DSWI values at the surface. This is accomplished by adjusting the entire ω_0 curve, instead of changing a value at a particular wavelength. Figure 5.10a (dotted lines) shows the results of a 10% increase (from 0.823-0.906) in ω_0 and in Figure 5.10b the 'X' symbols show the corresponding changes in DSWI values; the RMS errors now are decreased from 113.8 to 55.2 W m^{-2}. A 15% increase in ω_0 (from 0.823 to 0.943) results in a decrease in RMS errors from 113.8 to 17.9 W m^{-2}. This is an extreme case where the RMS errors were rather large (113.8 W m^{-2}) to begin with. This range of single scattering albedo is consistent with other SCAR-B studies (e.g. Dubovik et al. 1998). While changes to ω_0 alone can reduce the RMS errors between the measured and calculated DSWI values, in an operational algorithm τ values may

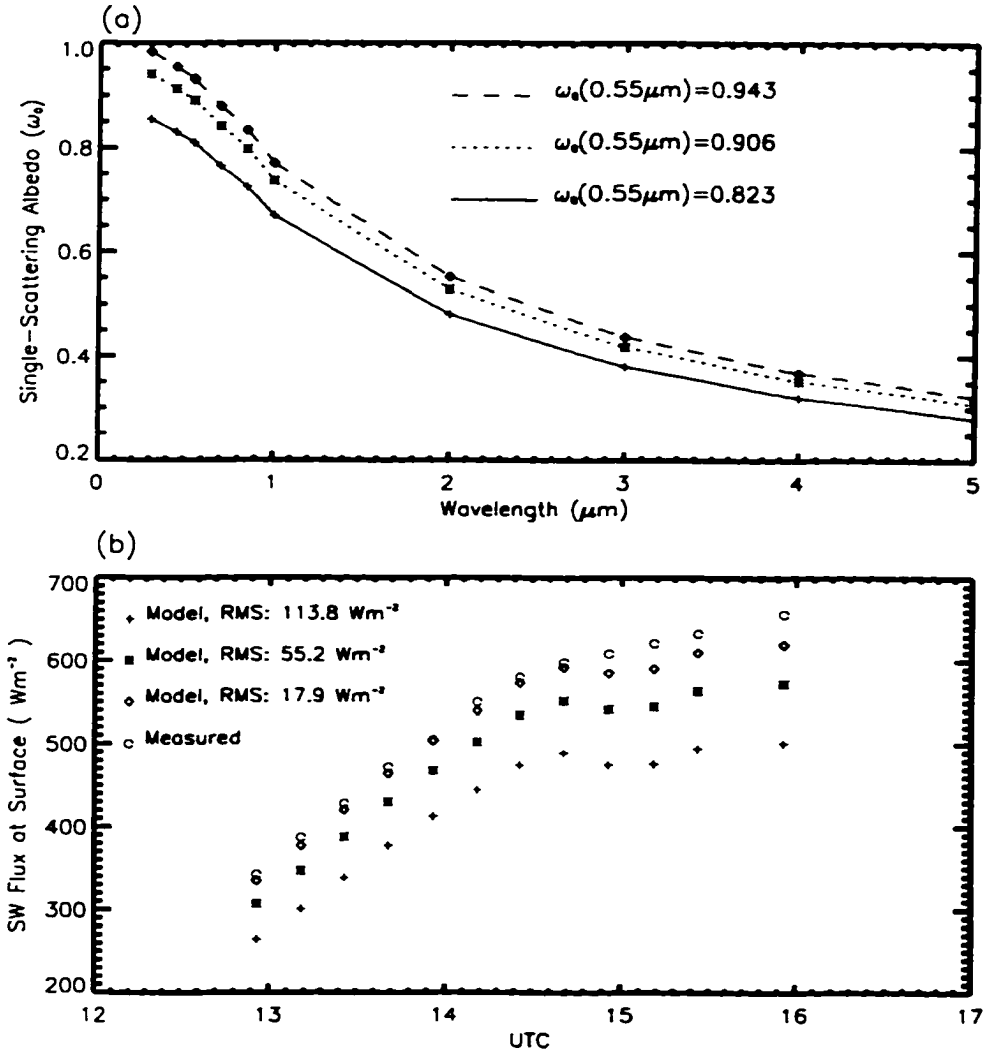

Figure 5.10 Tuning single-scattering albedo to match measured and calculated values for Potosi Mine on September 5 1995.
a) wavelength dependence of the single scattering albedo and
b) calculated DSWI values

also have to be simultaneously adjusted to provide the desired accuracy in the estimation of DSWI values. Note that a change in the dependency of ω_0 with λ will also cause the change of calculated DSWIs.

5.4 Biomass burning season over South America and Africa in 1998

The investigation of the radiative impact of smoke aerosols at both the TOA and the surface over South America and Africa are presented in this section. The study area over South America is between 30°S and 0° in latitude and 70°W and 40°W in longitude. The study area over Africa is between 30°S and 5°S in latitude and 10°E and 40°E in longitude. In this study, both the instantaneous and the daily-averaged smoke radiative forcings are investigated. The instantaneous direct SWARFs for smoke aerosols at the TOA and surface are presented in Section 5.4.1. The diurnally averaged SWARFs at the TOA and surface are presented in Section 5.4.2.

5.4.1 Instantaneous direct SWARF of smoke aerosols

The instantaneous SWARFs of smoke aerosols are estimated using the collocated VIRS and CERES samples. The collocation procedure is presented in Section 2.3. The biomass burning events prevail during the dry season in August-September over South America and Africa. Due to the lack of availability CERES data in September 1998, only the VIRS and CERES data in August 1998

are used to investigate the smoke radiative forcings during the 1998 burning season.

The instantaneous direct SWARFs of smoke aerosols are estimated using the following approach. First, the smoke detection algorithm described in Section 4.1 is applied to all VIRS data in August 1998 to separate smoke, cloud and clear-sky pixels in the images. Then the collocation procedure is applied to the VIRS and the CERES data. For each collocated sample corresponding to a CERES footprint, the smoke, cloud and clear-sky fractions for the sample are calculated based on the number of identified VIRS pixels in each of the three types within the footprint. The collocated samples for which the clear-sky fraction is larger than 90% are considered as clear samples, and the samples for which the smoke fraction is larger than 90% are considered as smoke samples. Only the smoke and clear samples are used to investigate the smoke radiative impact. For a smoke sample, assuming a value of ω_0 (0.64 μm) of 0.89 that is typical for smoke aerosols (Reid et al. 1998), the τ value is retrieved using the table look-up approach introduced in Chapter 4. From the clear-sky samples obtained in that month, the broadband TOA clear-sky albedo map is produced using the procedure described in Chapter 4. The broadband TOA clear-sky albedo is directly used in the calculation of TOA SWARFs. Using the SBDART model, the broadband surface albedo then is estimated from the observed TOA albedo assuming standard tropical vertical profiles (McChatchey et al 1972) under clear-sky conditions.

The TOA SW flux for a collocated smoke sample is obtained by applying the observed CERES radiance to the smoke ADM with the values of assumed ω_0 and retrieved τ. The TOA SW flux for a clear-sky sample is directly obtained from the CERES ES8 ERBE-like product. Assuming the standard tropical profiles (McChatchey et al. 1972), both the upward and downward SW fluxes at the TOA and surface are calculated using the δ-four stream model with the assumed ω_0 and retrieved τ values. The spectral surface albedos required as the input to the δ-four stream model are the ones parameterized as the function of the IGBP ecosystems. These parameterized spectral surface albedos are calculated and used in the CERES SARB project (*http://tanalo.larc.nasa.gov: 8080/Surf_htmls/SARB_Surf.html*). In these calculations, the parameterized spectral surface albedos are scaled so that the broadband surface albedos equal the surface albedos estimated from the CERES observations. The calculated TOA and surface SW fluxes from the δ-four stream model are referred to as model TOA and surface SW fluxes, respectively. Accordingly, the SWARFs calculated using the model SW fluxes are referred to as model SWARFs. Figure 5.11 (a) shows the number of detected smoke pixels from the VIRS images in August 1998, and Figure 5.11 (b) shows the IGBP surface ecosystem map over South America. The spatial resolutions of the grid in Figure 5.11 (a) and (b) are 0.5° x 0.5° degree. From Figure 5.11 (a), the smoke aerosols prevailed mostly over the Amazon region in Brazil where the major surface ecosystems are savanna, forest, and grassland. This is consistent with the findings during the

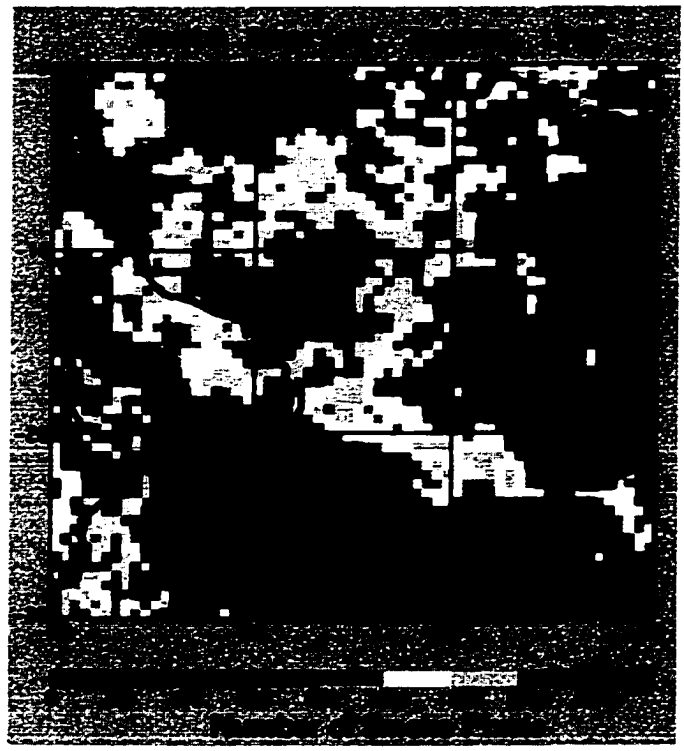

(a)

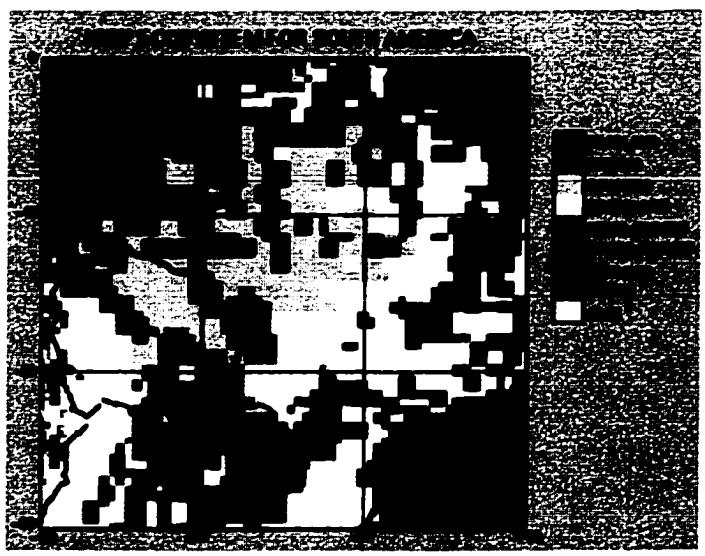

(b)

Figure 5.11 (a) The number of smoke pixels detected from the VIRS images in August 1998 over South America. (b) IGBP surface ecosystem map over South America

SCAR-B experiment as well as in earlier studies (Christopher et al. 1998; Prins et al. 1998). Other areas where smoke aerosols prevailed are in Southwest Bolivia and Northwest Argentina where the major surface ecosystem type is grassland. The surface sunphotometer measurements also show that large aerosol optical thicknesses ($\tau(0.67\mu m) > 0.3$) have been observed over these regions *(http:// aeronet.gsfc.nasa.gov:8080/)*.

Figures 5.12 (a) and (b) show the broadband TOA clear-sky albedos and TOA albedos for smoke aerosols over South America obtained from the collocated clear-sky and smoke samples, respectively, in August 1998. The procedure to obtain clear-sky albedos is mentioned earlier in this section. The TOA albedo for smoke aerosols at a particular grid is the mean value of all the smoke samples falling into the grid during the month. The grid resolution is 0.2°x 0.2° for clear-sky albedos and 0.5°x 0.5° for smoke albedos. The mean broadband clear-sky albedo is about 0.16 and the mean broadband smoke albedo is about 0.21. Since the smoke albedo is larger than the clear-sky albedo, based on the definition of smoke radiative forcing in section 4.5, smoke aerosols have cooling effect on the earth system. At a solar zenith angle of 0° and assuming a solar constant of 1368 Wm^{-2}, the average instantaneous direct TOA SWARF for smoke aerosols is about -70 Wm^{-2}.

Figure 5.13 shows the monthly-averaged grid-mean values of the retrieved τ (0.64 μm) of smoke aerosols over the study area in South America.

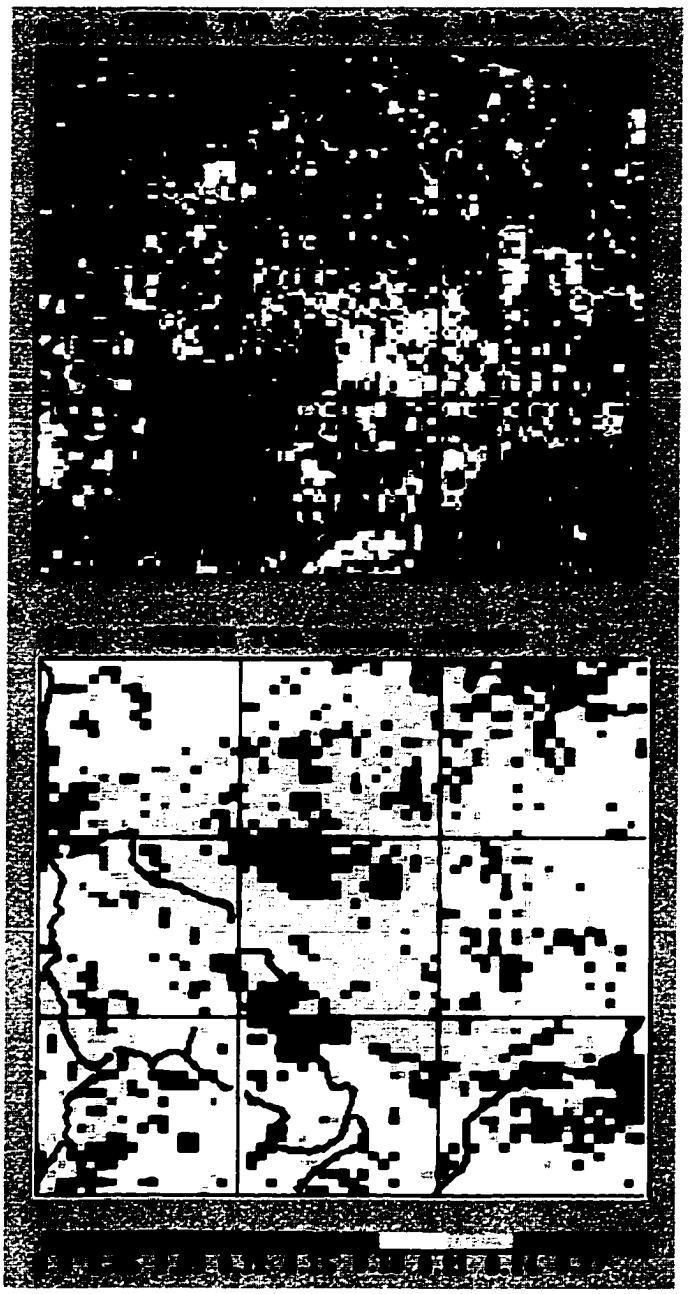

Figure 5.12 (a) Broadband TOA clear-sky albedo and (b) mean TOA albedo for smoke aerosols in August 1998 over South America obtained from the CERES Measurements.

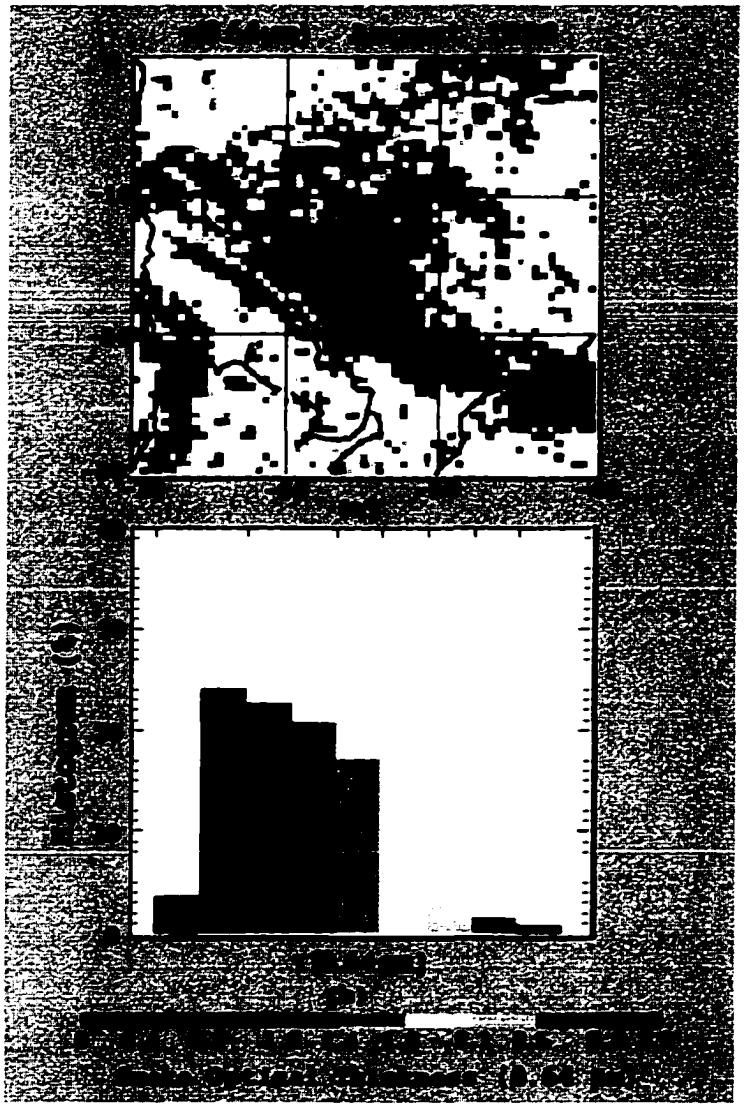

Figure 5.13 (a) monthly-mean optical thickness of smoke aerosols retrieved from the collocated smoke samples in August 1998 over study area in South America. The grid resolution is 0.5x0.5 degree. (b) frequency of occurrence of retrieved smoke optical thicknesses corresponding to (a).

The spatial resolution of this grid is 0.5° x 0.5°. Over the Amazon region (in the middle of the figure), the retrieved values of τ range between 0.7 and 1.4, indicating that strong biomass burning events occurred in 1998. Over the Southwest Bolivia and Northwest Argentina areas where the second peak of smoke pixels is identified from Figure 5.11(a), most of the τ values range between 0.7 and 1.0, also indicating strong aerosol loading over the region. From Figure 5.11(b), most of the retrieved τ values for smoke aerosols are within the range of 0.4 to 2.1.

Figure 5.14 (a) shows the number of detected smoke pixels from the VIRS images and Figure 5.14 (b) shows the IGBP surface ecosystem map over the study area in Africa. The spatial resolutions of the grid in Figure 5.14 (a) and (b) are 0.5° x 0.5°. Note that in contrast to the biomass burning season in South America in which there exists two regions (Amazon region and Bolivia-Argentina region) where smoke pixels are heavily identified, there is only a long strip area in Namibia (Southwest of the study area) where large number of smoke pixels (>2000) are detected from the VIRS images. The surface ecosystem over this area is grassland. There are two other small areas where the total detected smoke pixels is greater than 1500. One such area is in Zaire (middle top of the study area) with surface type of savanna and forest and another in South Africa (middle bottom of the study area) with surface type of grassland. There are two regions in the bottom left of the study area in which no smoke pixels are identified. One area is in Namibia and another one is in Botswana. The surface

(a)

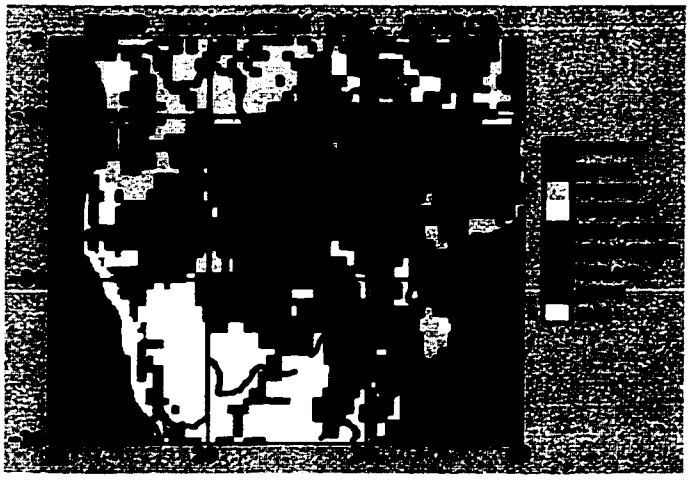

(b)

Figure 5.14 (a) The number of smoke pixels detected from the VIRS images in August 1998 over Africa. (b) IGBP surface ecosystem map over Africa

types over these two areas are barren land (labeled as other) and shrubs. One reason no smoke pixels are identified from the VIRS images in these areas is that barren land and shrubs are much less likely to be ecosystems in which biomass burning events occur. Also, due to the significantly larger surface albedos of these surface types (shown in Figure 5.15(a)), the smoke detection algorithm may not function well, since the algorithm is developed in the Amazon region where the dominant surface types are forest, savanna and grassland. For most of the areas (grids) in Africa, the number of identified smoke pixels is less than 1000, as compared with those in South America where the number of smoke pixels over many grids is over 1500. This suggests that the biomass burning events in South America during 1998 burning season occurs more frequently or are more intense than those in Africa. As a result, it is expected that radiative forcing is larger over South America than over Africa.

Figures 5.15 (a) and (b) show broadband TOA clear-sky albedos and TOA albedos for smoke aerosols over Africa obtained from the collocated clear-sky and smoke samples, respectively, in August 1998. From Figure 5.15 (a), the broadband TOA clear-sky albedos for most of the grids are between 0.12 and 0.18, similar to those obtained in South America. However, over the bottom-left region of the study area, the TOA clear-sky albedo is over 0.24. These large TOA clear-sky albedos are caused by the barren ground and shrubs ecosystems which are the dominant surface types over that area. No smoke samples are

(a)

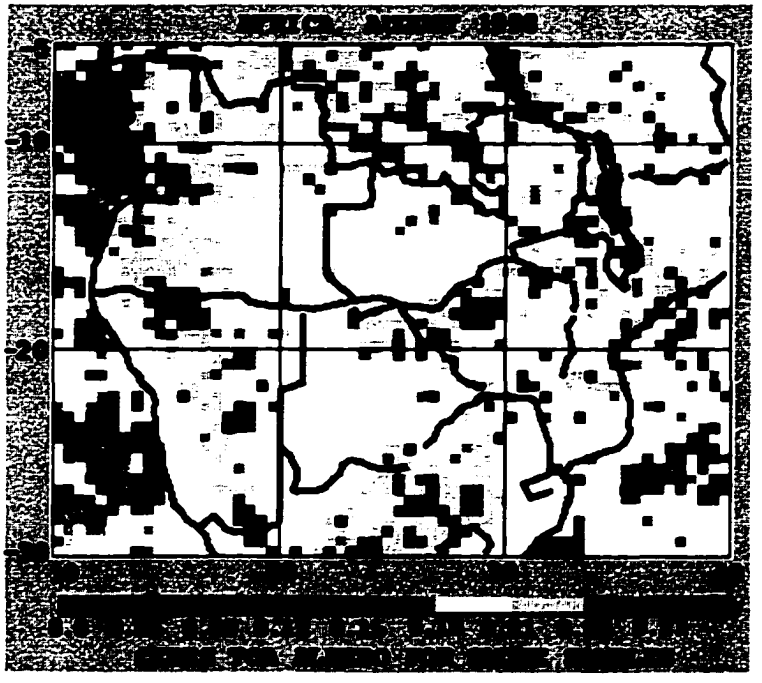

(b)

Figure 5.15 (a) Broadband TOA clear-sky albedo and (b) mean TOA albedo for smoke aerosols in August 1998 over Africa obtained from the CERES measurements.

obtained over this area. The mean broadband smoke albedo over Africa is about 0.21, similar to that found in South America.

Figure 5.16 shows the monthly-averaged grid-mean values of retrieved τ (0.64 μm) of smoke aerosols over the study area in Africa. The spatial resolution of the grid is 0.5° x 0.5°. From Figure 5.16 (a), it is seen that the mean τ values are less than 0.7 over 80% of the grids, as compared with those in South America where the retrieved values of τ range between 0.7 and 1.4. This suggests that the biomass burning is more intense in South America than in Africa.

The relationship between aerosol optical thickness and the observed TOA SWARF is examined using the collocated smoke samples over both South America and Africa. The retrieved τ values of smoke aerosols at 0.64 μm are divided into 10 intervals: 0.2-0.55, 0.55-0.90, 0.90-1.25, 1.25-1.60, 1.60-1.95, 1.95-2.30, 2.30-2.65, 2.65-3.0, 3.0-3.35, and > 3.35. The statistics of instantaneous direct radiative forcings of smoke aerosols is obtained for each τ interval, including the means and standard deviations of aerosol τ values, and the TOA and surface downward SWARFs. If the number of samples in an interval is less than 1% of the total number of samples, the calculated mean and standard deviation of the radiative forcings are omitted due to the lack of enough

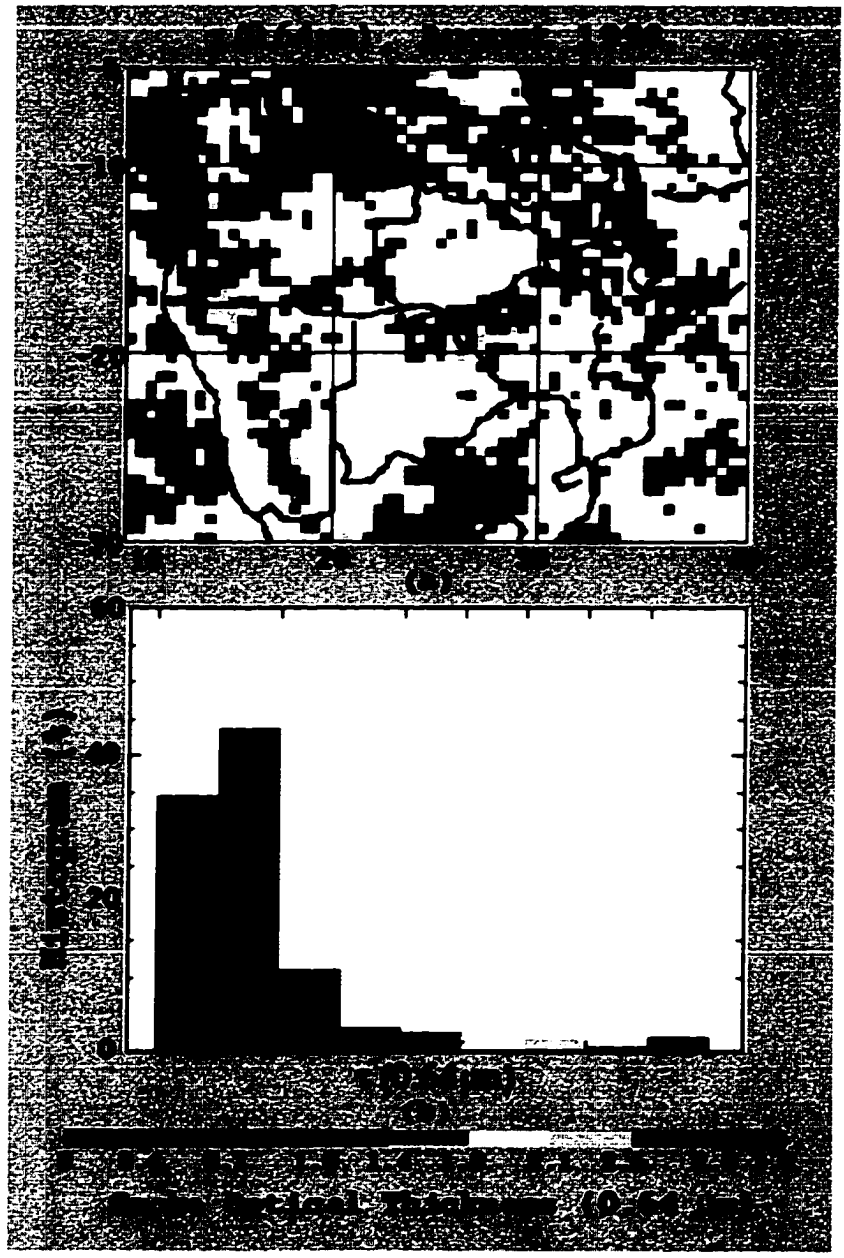

Figure 5.16 (a) monthly-mean optical thickness of smoke aerosols retrieved from the collocated smoke samples in August 1998 over study area in South America. The grid resolution is 0.5x0.5 degree. (b) frequency of occurrence of retrieved smoke optical thicknesses corresponding to (a).

samples. In addition, the mean values of model-estimated TOA SWARFs are also calculated.

Figure 5.17 (a) shows the observed (solid line) and model-estimated (dot line) instantaneous direct TOA SWARF versus τ at 0.64μm obtained from 28780 smoke samples over South America. Also shown as the horizontal and vertical lines are the standard deviations of the observed TOA SWARF and τ values for each interval of τ. From Figure 5.17 (a), it is seen that the magnitude of TOA SWARF increases with increasing τ. When τ increases from 0.40 to 1.80, the magnitude of TOA SWARF increases from -19 Wm^{-2} to –70 Wm^{-2}, the ratio of TOA SWARF per τ being about –36.4 Wm^{-2}. However, when τ is larger than 2.3, the magnitude of the TOA SWARF value does not increase significantly with increasing value of τ. From Figure 5.17 (a), it is seen that in each τ interval, the standard deviation of TOA SWARF is larger than 25 Wm^{-2}, indicating large variation. This is expected since the TOA SWARF value is a function not only of τ but also of solar zenith angle and TOA clear-sky albedo. Comparison of the observed TOA SWARF values with model-estimated TOA SWARF values shows that the model TOA SWARFs are more than 20 Wm^{-2} larger than those of observed TOA SWARFs when τ is smaller than 1.2. This difference may be caused by the over-estimation of TOA clear-sky albedo due to cloud contamination. At solar zenith angle of 0°, an over-estimation of TOA clear-sky albedo by about 0.015 would decrease the magnitude of the observed TOA SWARF by 20 Wm^{-2}. When smoke loading is light (τ values smaller than 0.5), an

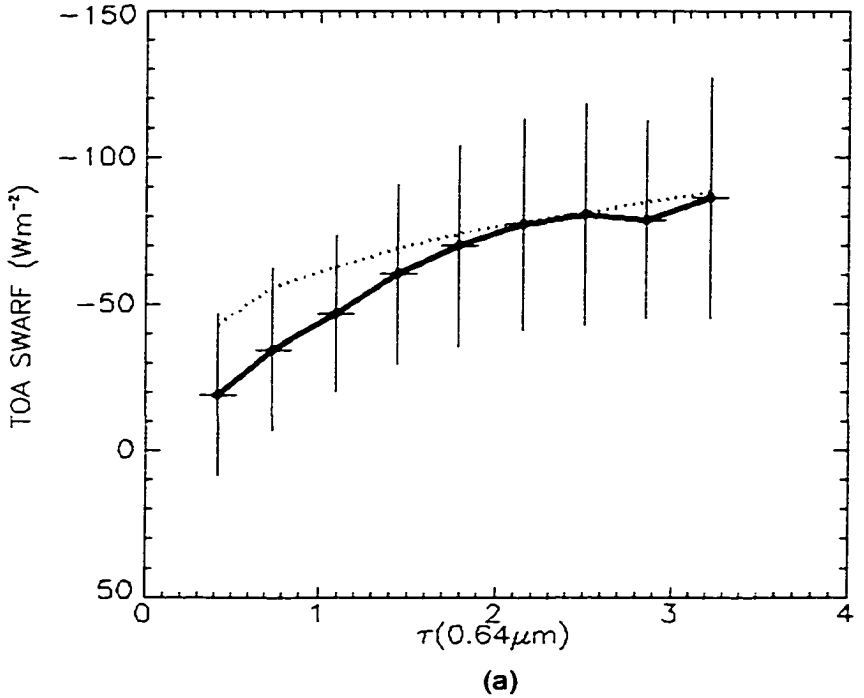

(a)

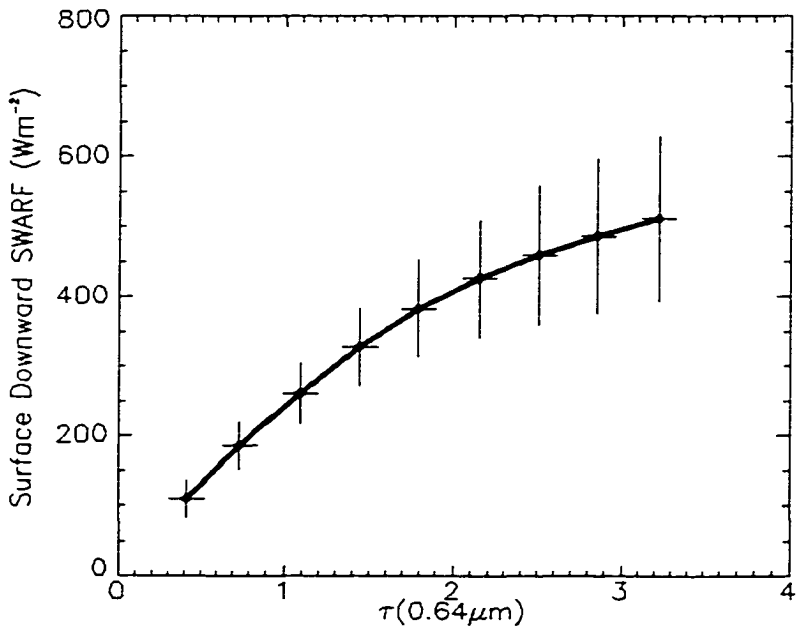

(b)

Figure 5.17 (a) the observed instantaneous direct TOA SWARF (thick solid line) and the model-estimated direct TOA SWARF (thick dash line) versus $\tau(0.64\mu m)$. (b) the instantaneous direct surface downward SWARF versus $\tau(0.64\mu m)$. The horizontal and vertical lines represent the standard deviations of SWARF and τ variables. The study area is in South America.

over-estimation of TOA clear-sky albedo is more significant in affecting the TOA SWARF estimation since the scattering effect of smoke aerosols does not significantly dominate over the surface reflectance.

Figure 5.17 (b) shows the model surface downward values of SWARF versus τ at 0.64μm. It is seen that values of surface downward SWARF increase with increasing aerosol τ value. Based on the definition of surface downward SWARF in section 4.5, if surface downward SW fluxes decrease at the presence of smoke aerosols as compared to the smoke-free conditions, the values of surface downward SWARF are positive. As a result, the positive value of surface downward SWARF indicates smoke "cooling effect" on the surface radiation budget. When τ increases from 0.40 to 1.80, the surface SWARF increases from 110 Wm^{-2} to 380 Wm^{-2}, the ratio of TOA SWARF per τ being about 190 Wm^{-2}. However, when τ is larger than 2.3, the surface SWARF values increase less significantly with increasing τ. With a τ value of 3.2, the surface downward SWARF value reaches 510 Wm^{-2}. From Figure 5.17 (b), the standard deviation of surface downward SWARFs increases with increasing τ. Also from Figure 5.17, it is seen that smoke aerosols have a larger impact on the surface radiation budget than on the TOA radiation budget. It will be shown in the next section that both TOA and surface SWARFs are affected by the aerosol single scattering albedo, as expected.

Figure 5.18 (a) shows the observed (solid line) and model-estimated (dotted line) instantaneous direct TOA SWARF versus τ at 0.64μm obtained from 8457 smoke samples over Africa. Also shown as the horizontal and vertical lines are the standard deviations of the observed TOA SWARF and τ values for each interval of τ. For the τ intervals of 1.25-1.60, 1.60-1.95 and 1.95-2.30, the numbers of smoke samples are 270, 140 and 88, respectively. The relative percentages are about 3.2%, 1.7% and 1%, respectively. In contrast from the results shown in Figure 5.17(a), Figure 5.18(a) shows that compared to the observed TOA SWARFs, the model TOA SWARFs are over-estimated when τ values are smaller than 1.0 and are under-estimated when τ values are larger than 1.4. Again, the under-estimations of the observed TOA SWARFs compared to the model estimations may be caused by the over-estimation of TOA clear-sky albedo due to cloud and smoke contamination. Note that the smoke samples with τ values larger than 1.4 have a greater probability of being contaminated by clouds. As a result, the TOA SW fluxes are larger and the corresponding TOA SWARFs also increase. This may be one reason why model TOA SWARFs are under-estimated when τ values are larger than 1.4. Also note that for the three intervals where τ values are larger than 1.4 the number of smoke samples are less than 6% of the total smoke samples, so that interpretation of the results in these intervals should be made with caution. Figure 5.18 (a) shows that as τ increases from 0.40 to 1.80, the magnitude of TOA SWARF values increase from –20 Wm^{-2} to -90 Wm^{-2}, the ratio of TOA SWARF per τ being about -50 Wm^{-2}, about 14 Wm^{-2} larger than that obtained over South America. This difference can

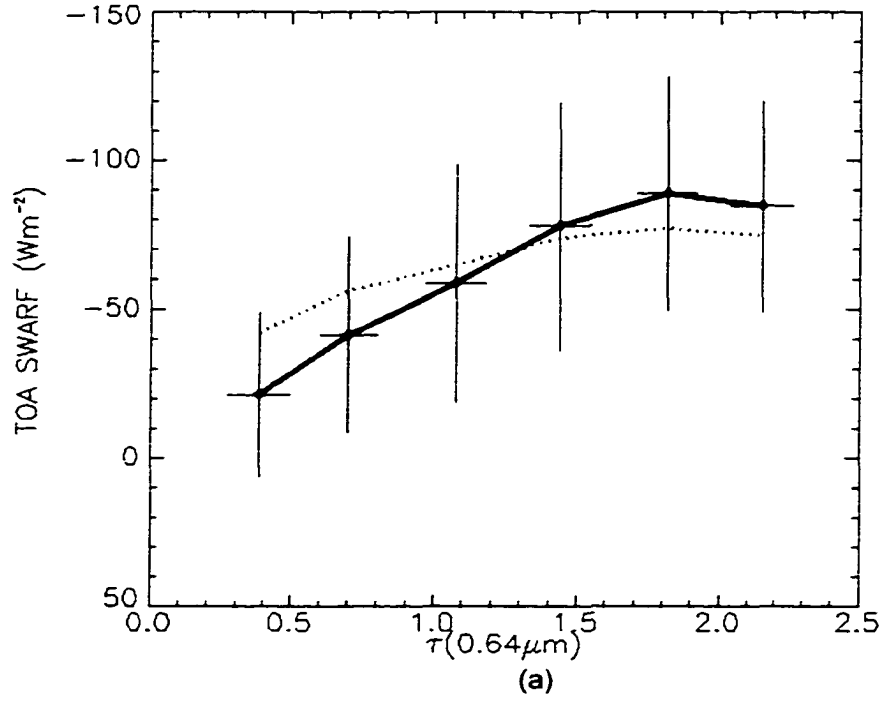

(a)

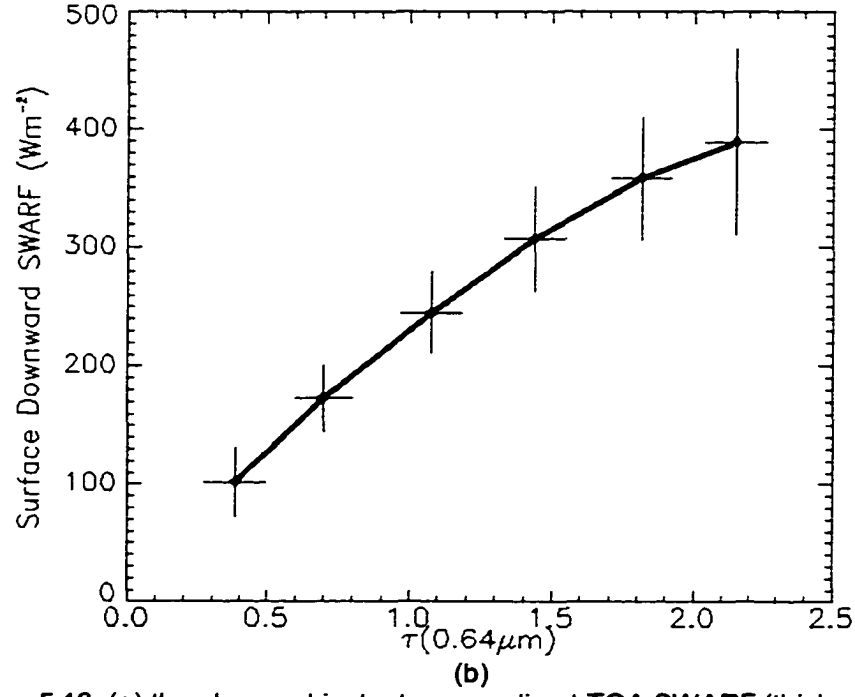

(b)

Figure 5.18 (a) the observed instantaneous direct TOA SWARF (thick solid line) and the model-estimated direct TOA SWARF (thick dash line) versus $\tau(0.64\mu m)$. (b) the instantaneous direct surface downward SWARF versus $\tau(0.64\mu m)$. The horizontal and vertical lines represent the standard deviations of SWARF and τ variables. The study area is in Africa.

be caused by the differences in surface albedo as well as the physical and optical properties of smoke aerosols.

Figure 5.18 (b) shows model surface downward SWARF values versus τ at 0.64μm. Similar to Figure 5.17 (b), the surface downward SWARF values increase with increasing aerosol τ value. As the value of τ increases from 0.40 to 1.80, the surface downward SWARF values increase from 100 Wm^{-2} to 360 Wm^{-2}, the ratio of TOA SWARF per τ being about 186 Wm^{-2}, close to that obtained in South America. At a τ value of 2.16, the surface downward SWARF value reaches 390 Wm^{-2}.

The results derived from the burning season in South America and Africa shows that smoke aerosols have "cooling effect" both at the TOA and at the surface and that the instantaneous smoke radiative impact is large at both the TOA and at surface. The TOA SWARF values can be over –100 Wm^{-2}, and the surface downward SWARF values can be over 600 Wm^{-2}. The ratio of TOA SWARF per optical thickness ranges between -35 to –50 Wm^{-2}, and the surface SWARF per optical thickness is about 190 Wm^{-2}.

One of the limitations in the estimation of instantaneous direct SWARFs is the assumption that the ω_0 value of smoke aerosols is known (Li et al., 1999). Clearly, the assumption of ω_0 is an important uncertainty factor which strongly

affects both the retrieval of τ and estimates of SWARF values. Figure 5.19 shows retrieved values of τ and SWARFs as a function of values of ω_0. In Figure 5.19, the solar zenith angle, viewing angle and relative azimuth angles are set to be 31°, 31°, and 45°, respectively. Surface albedo is 10%. Assuming aerosol τ of 0.78 and ω_0 of 0.825, the calculated upward TOA SW flux and DSWI value are 176.2 and 692.8 Wm^{-2}, respectively. If ω_0 value decreases to 0.795, the retrieved τ increases to 1.06, while the upward TOA SW flux is unchanged at 176.6 Wm^{-2} and the DSWI value decreases to 615.3 Wm^{-2}. On the other hand, increasing the value of ω_0 to 0.854, the retrieved τ decreases to 0.599, the upward TOA SW flux is relatively unchanged at 175.7 Wm^{-2} and the DSWI value increases to 752.1 Wm^{-2}. Clearly the assumed value of ω_0 has very little influence on the TOA SW flux values. However, it does have a large influence on the surface flux estimation. An uncertainty of ω_0 by 0.03 causes an error in the surface SW flux estimation to be over 60 Wm^{-2}. Also, the error caused by the assumption of ω_0 is asymmetric. Underestimation of ω_0 causes larger errors in DWSI values. Figure 5.19 demonstrates the importance of accurate ω_0 in the estimation of surface radiation budgets.

5.4.2 Diurnally-averaged radiative forcings of smoke aerosols

While the investigation of the instantaneous radiative forcings of smoke aerosols is essential to a detailed understanding of the smoke radiative impact

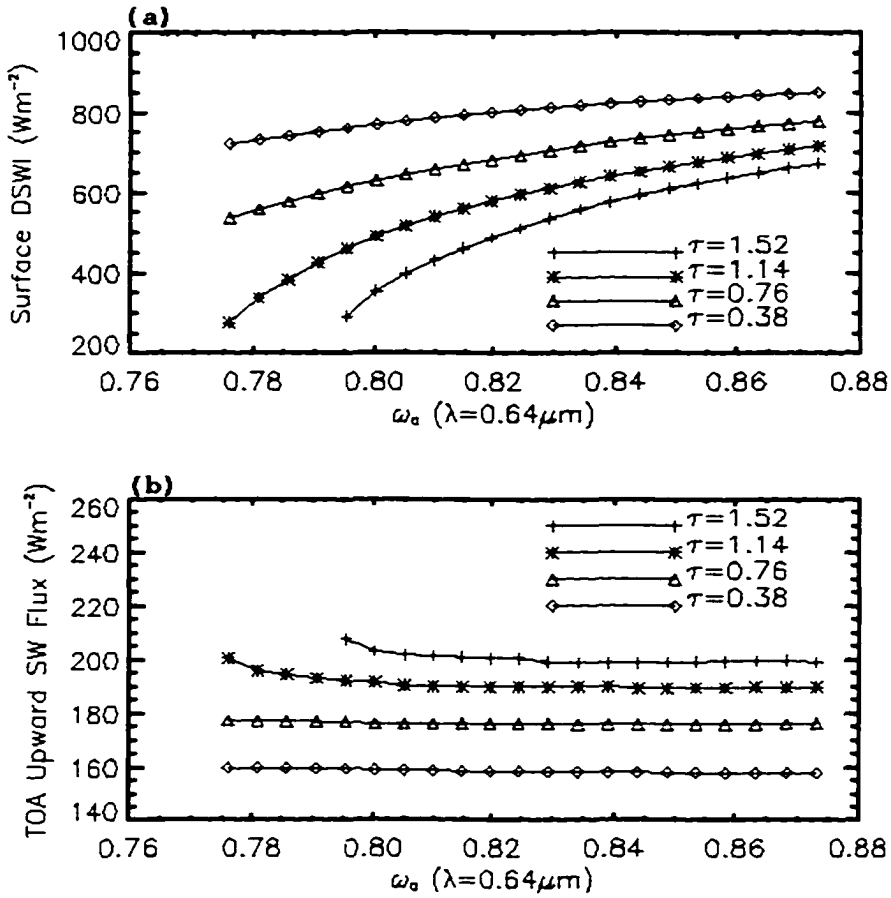

Figure 5.19 Infulence of assumed ω_0 on the estimation of (a) surface DSWI and (b) TOA upward SW flux. Solar zenith angle, viewing zenith angle, and relative azimuth angle are 30°, 30° and 40°, respectively. Surface albedo is 0.10.

and the relationship between smoke optical properties and smoke radiative forcings, diurnally-averaged smoke radiative forcings are the more appropriate parameters to characterize the smoke radiative impact on earth radiation budget and their influence in global climate models. In this section, the daily-averaged smoke radiative forcings at both the TOA and surface are estimated, and the relationship between smoke optical properties and their radiative forcings are investigated.

The diurnally-averaged smoke radiative forcings for each grid are estimated in the following approach. On each day, the smoke mean τ value for a grid is obtained by averaging the retrieved τ values of all the smoke samples falling into the grid. For grids in which there are no smoke samples, the mean τ values are not available and smoke radiative forcings are not estimated. Assuming that smoke loading (optical thickness) does not change significantly during a day, the mean τ value over a grid is considered to represent the average aerosol loading of that grid during the day. Then, the smoke TOA and surface SW fluxes as well as the TOA and surface SWARFs are calculated using the δ-four stream model. The daily-mean radiative forcings at both TOA and surface are calculated using following equations:

$$SWARF^{TOA}(daily\_mean) = \sum_{i=1}^{24} SWARF^{TOA}(i)/24 \quad \text{.....(5.1),}$$

$$SWARF^{SFC}(daily\_mean) = \sum_{i=1}^{24} SWARF^{SFC}(i)/24 \quad \text{.....(5.2),}$$

where $SWARF^{TOA}(i)$ and $SWARF^{SFC}(i)$ are the TOA and surface radiative forcings of smoke aerosols at the ith UTC hour.

During burning season, smoke optical thickness may change significantly during a day due to advection of well-mixed uniform smoke from regional fires and/or production of smoke from local fires (Holben et al. 1996). As a result, the estimated daily-mean TOA and surface SWARFs may be either under-estimated or over-estimated using the retrieved smoke optical thicknesses, depending on the deviations of the retrieved τ values from the equivalent τ values during the day. Over Cuiaba and Alta Floresta in 1994, the mean values and standard deviations of smoke optical depth at 0.44 μm are 1.39 ± 0.51 and 1.73 ± 0.62, respectively, for a total of 50 days (Holben et al. 1996).

Figure 5.20 shows the time-series of model-calculated instantaneous TOA and surface downward SWARFs. The ω_0 value at 0.64μm and TOA broadband clear-sky albedo are 0.88 and 0.16, respectively. The τ values at 0.64μm are 0.90, 1.38 and 0.86, respectively. Figures 5.20 (a) shows that the absolute value of TOA SWARF decreases with decreasing solar zenith angle (The local noon is at about 15 UTC). Although the incoming solar irradiance decreases with increasing solar zenith angle, at large solar zenith angle the optical depth of smoke aerosols is much larger than that at nadir assuming daily-constant optical

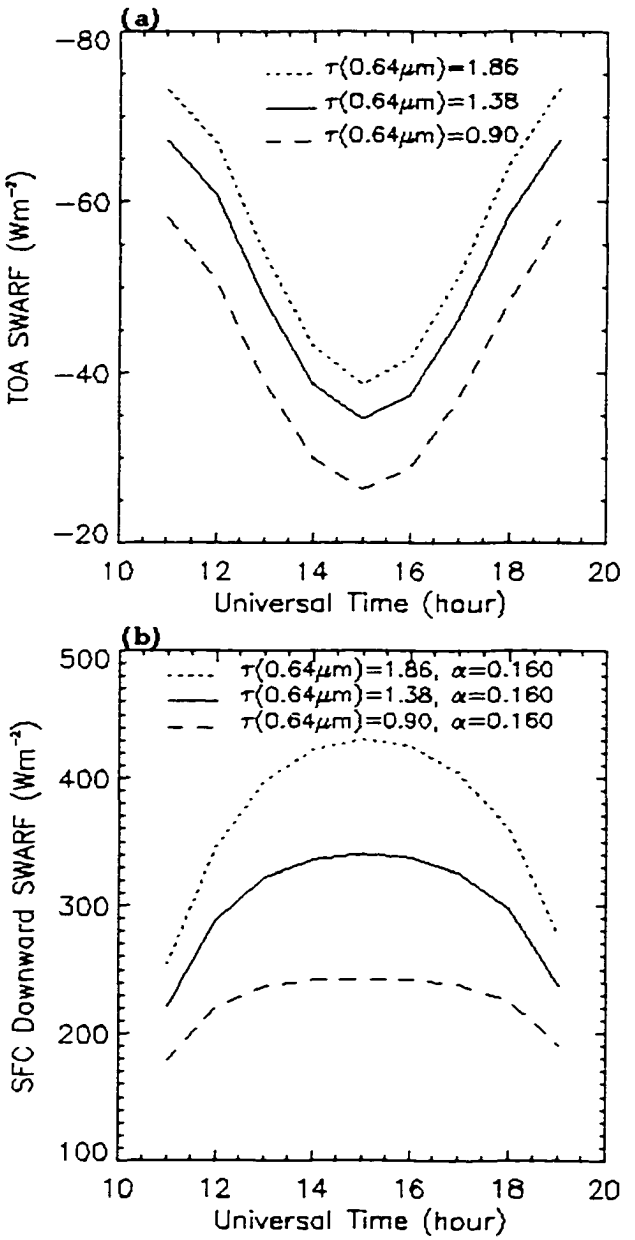

Figure 5.20 diurnal variation of (a) TOA SWARFs and (b) surface downward SWARFs as a function of universal time. $\omega_0(0.64\mu m)$ = 0.88 and TOA albedo =0.16.

thickness. Since the TOA SWARF increases with increasing solar zenith angle, the effect of variation of smoke τ on the TOA SWARF due to the change of solar zenith angle dominates over that of variation of incoming solar energy. Figure 5.20 (b) shows that the surface downward SWARF increases with decreasing solar zenith angle due to the increasing of incoming solar energy at smaller solar zenith angles. For the surface downward SWARF, variations of incoming solar energy on the surface SWARF due to the changes in solar zenith angle dominates variations of smoke optical depth. The daily-mean values of TOA SWARF are –15.7, –19.1, and –21.1 Wm^{-2}, respectively, for τ values of 0.90, 1.38 and 1.86. The corresponding daily-mean values of surface downward SWARFs are 84.0, 112.7 and 138.2 Wm^{-2}, respectively.

Figure 5.21 shows the daily-mean smoke optical thickness, TOA SWARF and surface SWARF on August 29 1998 over the study area in South America. The retrieved $\tau(0.64\mu m)$ values reach a maximum of 3.4, with most values between 0.5 and 2.0. The maximum values of TOA SWARF reach –44 Wm^{-2}, with most of the values between –10 and –30 Wm^{-2}. The maximum values of surface downward SWARF reach 223 Wm^{-2}, with most of the values between 60 and 180 Wm^{-2}. With the mean aerosol optical thickness of about 1.5, Figure 5.21 shows that the daily-mean TOA SWARFs are about –20 to –25 Wm^{-2} and the surface downward SWARFs are about 90 to 120 Wm^{-2}. Positive values of surface downward SWARF mean that under the smoky conditions, the shortwave fluxes reaching the surface decrease as compared to clear-sky conditions.

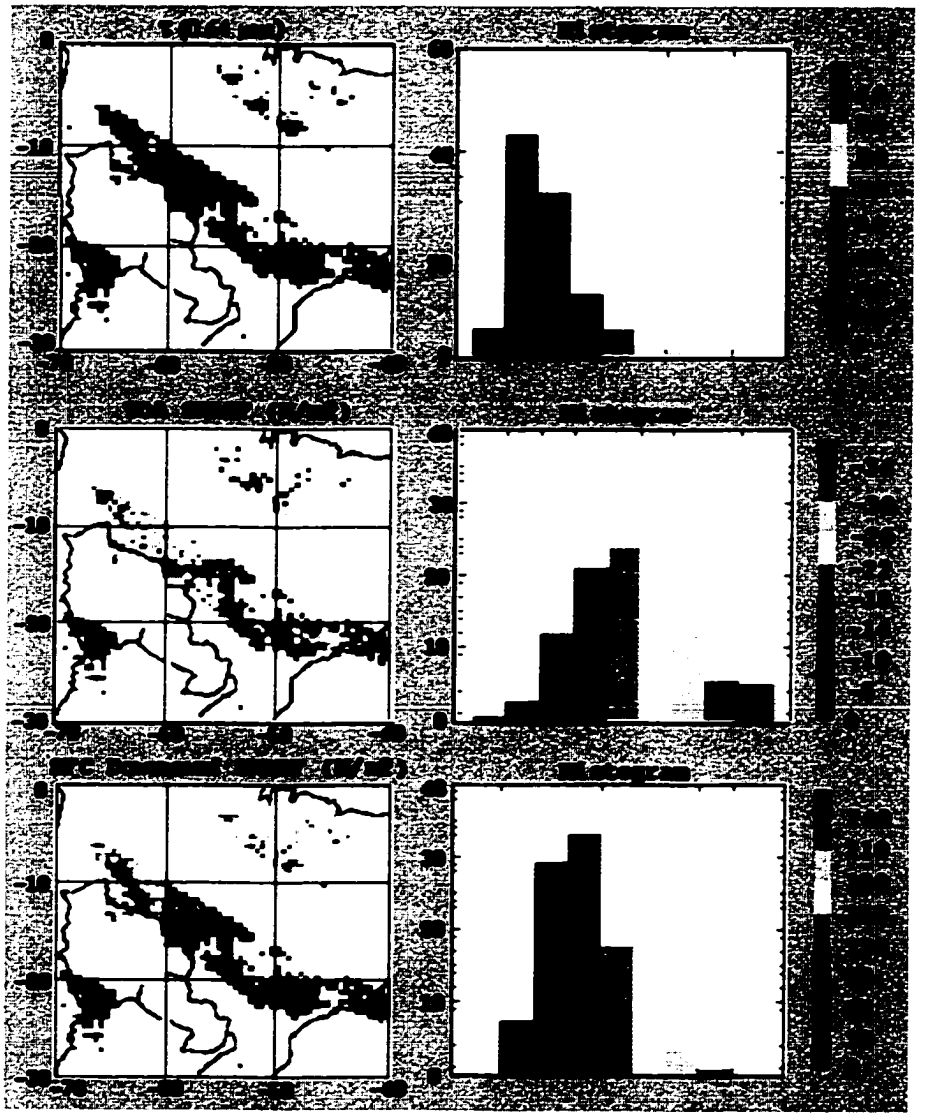

Figure 5.21 The daily-mean grid-averaged smoke optical thickness, TOA SWARF and surface downward SWARF as well as the frequency of occurrence of optical thickness, TOA SWARF and surface downward SWARF on August 29 1998 over South America.

Figure 5.22 shows the daily-mean smoke optical thickness, the TOA SWARF and the surface SWARF on August 10 1998 over the study area in Africa. The retrieved values of $\tau(0.64\mu m)$ range up to 3.53. Correspondingly, the TOA SWARFs range up to –44 Wm^{-2}, and the surface downward SWARFs range up to 216 Wm^{-2}. Since most of the retrieved τ values are within a value of 1.0, most of the TOA SWARFs are less than 18 Wm^{-2} and most of the surface downward SWARFs are less than 60 Wm^{-2}. Looking at the frequency of occurrence diagrams in both Figure 5.20 and 5.21, it is seen that the histogram of surface SWARF values is better correlated to the histogram for smoke optical thickness, while the histogram for TOA SWARF is less correlated to the histogram for smoke optical thickness. The reason is that the surface downward SWARFs are mainly determined by the smoke optical thickness, while the TOA SWARFs are a function of both smoke optical thickness and broadband surface albedo.

Figure 5.23 shows the model-calculated daily-mean TOA and surface SWARF values as function of τ (0.64 μm). The relationship between the SWARFs and aerosol optical thickness is shown for different combinations of ω_0 values and TOA clear-sky albedos, and two TOA clear-sky albedos are selected: 0.13, and 0.19. Two ω_0 values are selected: 0.85 and 0.90. Indeed, Figure 5.23(a) shows that the diurnally-mean TOA SWARF value is affected by τ, ω_0

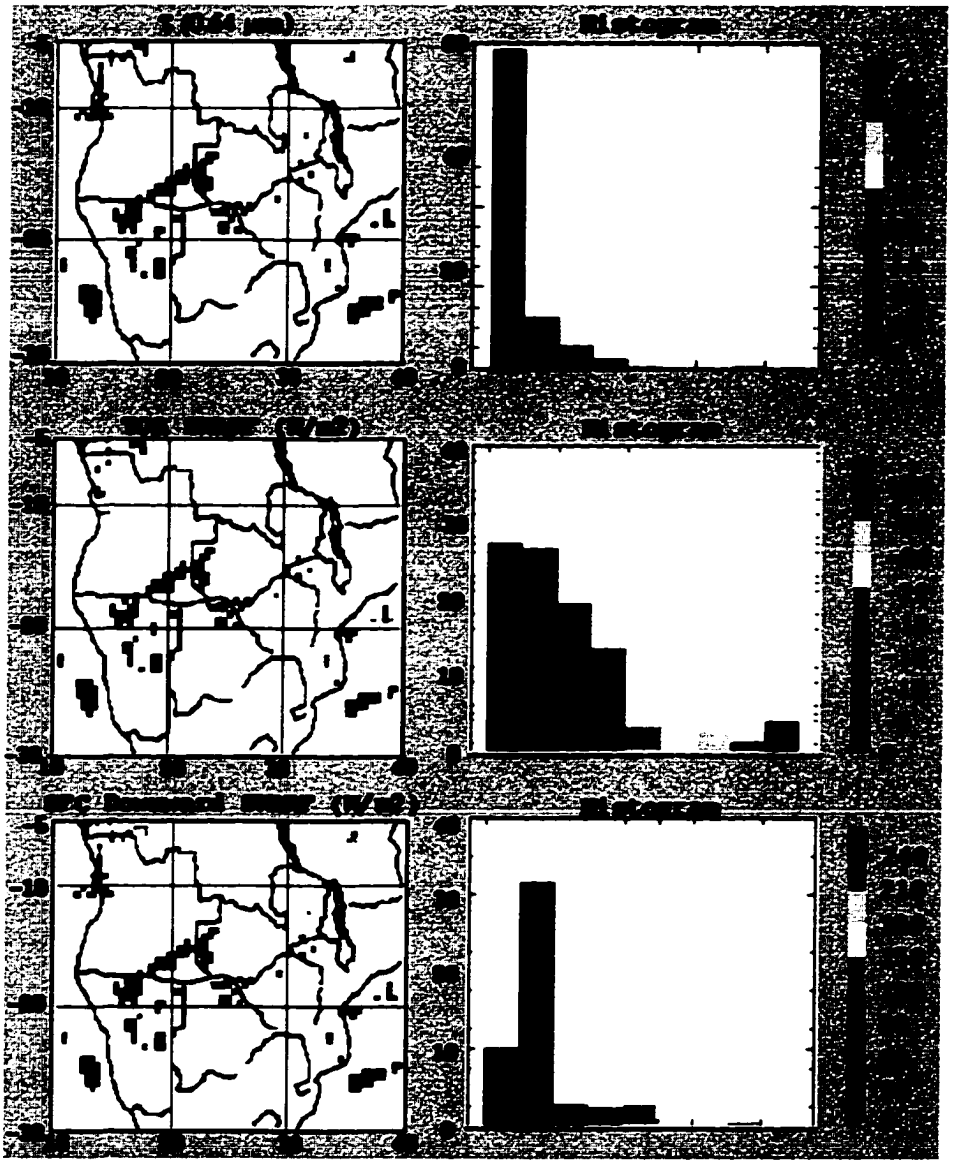

Figure 5.22 The daily-mean grid-averaged smoke optical thickness, TOA SWARF and surface downward SWARF as well as the frequency of occurrence of optical thickness, TOA SWARF and surface downward SWARF on August 10 1998 over Africa.

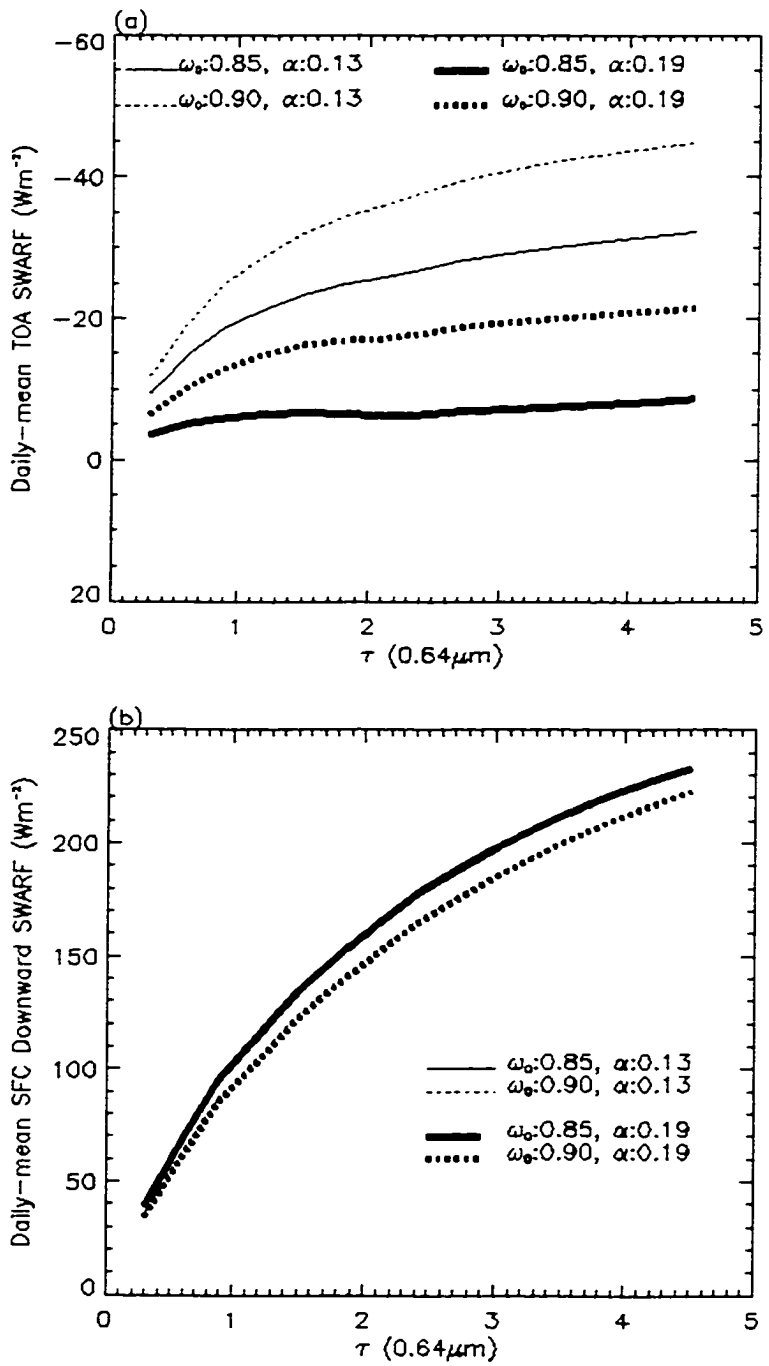

Figure 5.23 (a) The daily-mean TOA SWARF as function of smoke optical thickness and (b) the daily-mean surface downward SWARF as function of smoke optical thickness. The relationship is shown for aseries of combination of aerosol single scattering albedo and TOA clear-sky albedo.

and TOA clear-sky albedo (related to surface albedo). Fixing values of ω_0 and TOA clear-sky albedo, TOA SWARF values increase with increasing values of τ.

For a τ value of 0.9 and TOA clear-sky albedo of 0.13, the TOA SWARFs are –18.7, and –25.0 Wm^{-2} for ω_0 values of 0.85 and 0.90, respectively. When the τ value increases to 1.8, the TOA SWARFs are –24.8, and –34.3 Wm^{-2}, respectively. At a large ω_0 value of 0.90, the TOA SWARF value increases by about 9 Wm^{-2} as τ value increases from 0.9 to 1.8 due to the increase of smoke scattering. When the TOA clear-sky albedo increases to 0.19 and ω_0 value is 0.90, the daily-mean TOA SWARF value is –13.0 Wm^{-2}, a decrease of 12 Wm^{-2} compared to that for TOA clear-sky albefo of 0.13. From Figure 5.23, it is seen that fixing τ value, the TOA SWARF increases with increasing ω_0 and with decreasing TOA clear-sky albedo. This is expected since the larger the ω_0 value, the more reflective are the smoke aerosols. Also, the darker the surface (the smaller the TOA clear-sky albedo), the larger is the contribution of smoke aerosols on the reflected shortwave flux at the TOA and the larger is the smoke TOA SWARF.

Finally, Figure 5.23 (b) shows the relationship between smoke optical thickness and surface downward SWARF for smoke aerosols. Figure 5.23 (b) shows that the values of surface downward SWARF is basically not affected by the surface albedo (TOA clear-sky albedo). As expected, increasing τ values and decreasing ω_0 values increase the surface downward SWARF values. The

smaller the ω_0 value, the more absorptive the smoke aerosols and less SW flux reaches the surface. An increase of τ, in general, leads to greater reflection of SW energy back to space, and less solar energy reaches the ground. Note that positive values of surface downward SWARF indicates a cooling effect (reducing solar energy) of smoke aerosols on the surface radiation budget. When τ (0.64 μm) is 0.9, the surface downward SWARF values are about 80 to 100 Wm^{-2}, depending on the aerosol single scattering albedo. When the τ value increases to 1.8, the surface downward SWARF increases to about 140 Wm^{-2} for a ω_0 value of 0.90. The surface downward SWARF values increase with increasing value of τ, although the rate of change of surface SWARF becomes slower with increasing τ values.

CHAPTER 6

CONCLUSIONS AND SUMMARIES

The impact of biomass burning aerosols on the shortwave radiation budget at both the TOA and at surface has been investigated in this study. With the knowledge of microphysical and optical properties of smoke aerosols obtained during SCAR-B, three major issues involved in the estimation of smoke radiative forcings at the TOA and at surface using satellite measurements are addressed. First, a table look-up approach to retrieve the optical properties of smoke aerosols from the AVHRR and the VIRS images is developed. Second, the angular distribution model, used to convert the measured ERBE and CERES radiances into TOA shortwave fluxes, is estimated using a discrete-ordinate radiative transfer model. Third, a broadband δ-four stream radiative transfer model is modified to account for the smoke aerosols in the atmospheric radiative transfer process. This model is necessary to estimate the surface shortwave fluxes from the observed shortwave fluxes at the TOA. Finally, one month of VIRS and CERES data in August 1998 over the biomass burning regions both in South America and in Africa have been processed and analyzed to study the

radiative impact of smoke aerosols. The following are the conclusions and summaries of this study.

Using the look-up table approach developed in this study, the single scattering albedos of smoke aerosols have been retrieved using AVHRR channel 1 reflectances over nine sunphotometer sites in South America during SCAR-B. The retrieved mean ω_0 values at 0.64 μm are between 0.83 to 0.92, which is in good agreement (within 0.04) with the results from *in situ* and ground-based remote sensing measurements during SCAR-B, suggesting that this retrieval scheme is practical in estimating ω_0 values from AVHRR/VIRS observations. Using this approach, with the combination of ground-based sunphotometer measurements and satellite measurements such as AVHRR and GOES, the seasonally averaged single scattering albedo of smoke aerosols can be obtained.

Over Cuiaba Brazil, for a total of ten samples, the retrieved mean value of ω_0 at 0.64 μm is 0.84 (0.85 at 0.55 μm), in excellent agreement with the values obtained from the *in situ* measurements and retrieved from ground-based measurements, although the standard deviation of ω_0 from satellite retrieval is larger than that from the *in situ* measurements.

For ten out of fourteen cases, the RMS errors of DSWI between observations and model estimates using retrieved ω_0 values and the observed τ

values are within 30 Wm^{-2}, with maximum error of 51 Wm^{-2}. This indicates that the ω_0 values retrieved from AVHRR can be used to calculate the surface DSWIs over biomass burning regions.

The retrieval of ω_0 is sensitive to the accuracy of TOA clear sky albedo when aerosol optical thickness is smaller than 0.7. When τ is larger than 1.4, retrieval of ω_0 is much less sensitive to the TOA clear sky albedo. When τ is smaller than 0.5, one percent uncertainty in clear sky albedo can cause an error in retrieved ω_0 of 0.04. When τ is larger than 1.2, the error of retrieved ω_0 values is reduced to less than 0.01. On the other hand, in the retrieval of τ from the AVHRR visible channel, the results are less uncertain at the smaller values of τ.

The calculated smoke ADMs in this study are a function of aerosol τ and ω_0 values, surface albedo, solar zenith angle, satellite zenith angle, and the relative azimuth angle between sun and satellite. The smoke ADMs are relatively insensitive to the aerosol τ and ω_0 values and to the surface albedo. Uncertainties in the smoke ADM values due to uncertainties in these parameters are generally within 10%.

Comparisons of smoke ADMs with the ERBE clear-over-land and partly-cloudy-over-land ADMs show that although the range of the ADM values is similar between the two types of ADM models, the fine structures are different. The ERBE ADMs are more azimuth-angle sensitive compared to the smoke

ADMs. The relative differences of the ADM values between the two types of models is about 10% on average.

Using collocated VIRS and CERES ES8 data products over fourteen VIRS images in South America in August 1998, comparisons are made between the CERES ES8 ERBE-like TOA SW fluxes and those TOA SW fluxes converted from the observed TOA radiances using the smoke ADM. The correlation between the two data sets is about 96%, and the mean difference between the CERES TOA fluxes and model-estimated fluxes is 0.48 Wm^{-2}. However, the RMS error between the two data sets is 12.7 Wm^{-2}, showing that there exists discrepancies between CERES TOA SW fluxes and model-estimated TOA SW fluxes.

The TOA SWARF values for smoke aerosols are calculated, based on the surface types. The TOA SWARFs range from –32 Wm^{-2} to –55 Wm^{-2}, indicating that smoke aerosols have a cooling effect. The ratios of TOA SWARFs per unit optical thickness range from –29 Wm^{-2} to –57 Wm^{-2}, depending on surface albedos and aerosol optical thicknesses. The difference of estimated TOA SWARFs using CERES SW fluxes and SW fluxes from smoke ADMs are within 10 Wm^{-2}, and the relative differences are generally less than 10%. From this study, it is concluded that the smoke ADMs improve the accuracy of the TOA SW fluxes and smoke aerosol radiative forcing estimates.

Using the modified δ-four stream radiative transfer model, the downward shortwave irradiances are calculated for two days over Cuiaba and Pantanal, where near-coincident aircraft and sunphotometer measurements were available. The calculated DSWI values are then compared with broadband Eppley pyranometer DSWI measurements at the surface. For these two cases, it is shown that the RMS errors are less than 20 W/m^2. This indicates that the radiative effect of smoke aerosols have been properly characterized in the δ-four stream model. This model now can be used to calculate atmospheric radiative transfer for smoke aerosols.

When single scattering albedo values have to be assumed, the RMS errors for six other days range from 45-95 W/m^2. This indicates the importance of ω_o value in the surface shortwave flux estimation. It is concluded that ω_o must be known to within 0.05 and τ_s must be known within 0.1 to estimate DSWI values to within 20 W/m^2. When aerosol optical thickness data are available, a simple first-order tuning of ω_0 can reduce the RMS errors from 95 W/m^2 to within 15 W/m^2.

Analysis of one month of VIRS and CERES data in August 1998 over South America and Africa show that the biomass burning season over South America is stronger than that over Africa. This is indicated by both the detected number of smoke samples and by the retrieved values of smoke optical thicknesses. Over South America, there are two major regions where smoke

prevails: in the Amazon basin and over Bolivia-Argentina border regions. These satellite observations are also supported by the ground-based sunphotometer measurements during the month.

Analysis of one month of VIRS and CERES data also shows that smoke aerosols have "cooling effect" at both the TOA and at surface. This is in agreement with the previous studies. The instantaneous direct smoke shortwave radiative forcing at surface is much larger than that at the TOA. The smoke forcing at the TOA can reach over –100 Wm^{-2} and smoke forcing at the surface can be over 600 Wm^{-2}, depending on the smoke optical thickness, solar zenith angle and surface albedo. From the month of data, the TOA smoke forcing per $\tau(0.64\mu m)$ ranges from –35 Wm^{-2} to –50 Wm^{-2}, and surface downward smoke forcing per $\tau(0.64\mu m)$ is about 190 Wm^{-2}. The rate of change of smoke forcing with τ slightly decreases with increasing τ. When τ is larger than 2.0, the smoke SWARF does not increase as rapidly as that when τ is smaller than 1.0.

Analysis of data on August 29 over South America shows that most of the retrieved values of τ range between 0.5 and 2.0 and are located in Amazon, indicating strong aerosol loading in this area. Assuming that the aerosol loadings do not change during the day, the estimated daily-averaged smoke TOA forcings range from –5 to –48 Wm^{-2}, with most of the values between –19 and –25 Wm^{-2}. The estimated daily-averaged smoke surface downward forcing ranges from 0 to up to 220 Wm^{-2}, with most of the values between 60 to 150 Wm^{-2}. This analysis

shows that strong radiative impact of smoke aerosols on the radiation budget, especially at the surface.

Model simulations show that when τ(0.64 μm) is 1.0 and TOA clear-sky albedo is 0.16, the diurnally-mean TOA SWARF changes range from –13 to –20 Wm^{-2} when ω_o value ranges from 0.85 to 0.90. When τ increases to 2.0, the smoke forcing ranges from –15 to –25 Wm^{-2}. The TOA SWARF of smoke aerosols is the function of aerosol optical thickness, single scattering albedo, surface albedo and solar zenith angle. At the surface, the downward smoke forcing is about 80-100 Wm^{-2} when τ is 1.0, and the downward smoke forcing increases to 170 Wm^{-2} when τ is 2.0.

One of the limitations in the estimation of smoke radiative forcing over the two study areas is the assumption of single scattering albedo of smoke aerosols. Sensitivity studies show that an uncertainty in the ω_o value by 0.03 causes an error of surface SW flux estimation to be over 60 Wm^{-2}, thereby causing a significant error in surface radiative forcing estimation. This indicates the importance of obtaining accurate ω_o values. One limitation of the present study is that estimated surface downward shortwave forcings cannot be validated due to the lack of observational surface shortwave flux measurements over the study areas.

Based on the definition of smoke radiative forcing, the accuracy of TOA clear-sky albedo directly determines the accuracy of the estimated TOA SWARF. The other major uncertainty of smoke radiative forcing can be caused by the incorrect identification of smoke pixels from satellite images. Misidentification of cloud pixels for smoke pixels will over-estimate the smoke TOA and surface radiative forcings. The high spatial resolution and multi-channels in the visible spectrum will make the MODIS measurements a better satellite observational dataset in the estimation of smoke radiative impacts. The MODIS data are expected to improve smoke identification and to obtain a simultaneous retrieval of smoke optical thickness and single scattering albedo with multi-channel data. As a result, an improvement in the accuracy of the estimated smoke radiative forcings is expected.

CHAPTER 7

FUTURE WORK

The global radiative impact of biomass burning aerosols on the radiation budget at both the TOA and surface will be one of the promising areas in future research, and satellite measurements are the essential way to estimate the global smoke radiative forcings at both the TOA and at surface. This research work addresses several major issues for estimating the smoke radiative forcings using satellite measurements, including smoke identification using a multi-spectral thresholding technique, the retrieval of optical thicknesses of smoke aerosols, development of a smoke angular distribution model, and construction of a δ-four stream model to estimate surface shortwave fluxes. Several future studies are expected to improve our understanding of smoke optical properties and their radiative impact.

With higher spatial resolution and more spectral channels available in the visible and near-infrared spectrum, satellite measurements from the MODIS instrument on board the Terra satellite will improve the smoke identification

scheme and accuracy of the smoke optical property retrievals. Due to the spectral dependency of smoke optical thickness in the visible and near-infrared spectral interval, multi-channel observations from MODIS in these spectral intervals will be very helpful in separating the smoke from clouds whose optical thicknesses are very less spectrally dependent. With the available multiple channels in this spectral interval, the smoke optical thickness and other smoke optical and microphysical properties can be estimated simultaneously. This will improve the estimation of smoke radiative forcing at both the TOA and at surface.

Due to excellent temporal coverage, the GOES data provide a better opportunity to study the diurnally-averaged smoke radiative impact. The combination of the GOES data with the MODIS and the CERES data from Terra platform will improve both the instantaneous and diurnally-averaged smoke radiative forcings at both the TOA and at surface.

Due to the lack of CERES data in September 1998, only one month of VIRS and CERES data in August 1998 are used to investigate the smoke radiative impact over South America and Africa. With the availability of coincident CERES and MODIS data, more data can be analyzed in the future work. The study area can be extended to Indonesia and other biomass burning aeras.

REFERENCES

Ackerman, T. P., and O. B. Toon, 1981: Absorption of visible radiation in atmosphere containing mixtures of absorbing and nonabsorbing particles, *Applied Optics*, 20, 3,661-3,667

Andreae, M. O., 1991: Biomass burning: Its history, use, and its distribution and its impact on environmental quality and global climate, *Global Biomass Burning*, J. S. Levine, ed., 1-21

Barkstrom, B.R., 1984: The Earth Radiation Budget Experiment (ERBE), *Bull. Amer. Meteor. Soc.*, 65, 1,170-1,185

Belward, A. and T. Loveland, 1996: The DIS 1km land cover dataset, *Global Change, the IGBP news letter*, 27

Chang, H., and T. T. Charalampopoulos, 1990: Determination of the wavelength dependence of refractive indices of flame soot, *Proc. R. Soc. London, Ser.A*, 430, 577-591

Charlock, T.P., and T.L. Alberta, 1996: The CERES/ARM/GEWEX Experiment (CAGEX) for the retrieval of radiative fluxes with satellite data, *Bull. Am. Meteorol. Soc.*, 77, 2,673-2,683

Christopher, S.A., D.V. Vulcan, J. Chou, and R.M. Welch, 1996: First estimates of the radiative forcing of aerosols from biomass burning from satellite data, *J. Geophys. Res.*, 101, 21,256-21,273

Christopher, S.A., M. Wang, T.A. Berendes, R.M. Welch, and S.K. Yang, 1998: The 1985 biomass burning season in South America: Satellite resmote sensing of fires, smoke, and regional radiative energy budget, *J. Applied Meteor.* 37, 661-678

Christopher, S.A., X. Li, R. M. Welch, J. Reid, P. V. Hobbs, T. Eck, and B. Holben, 2000: Estimation of downward shortwave irradiances in the presence of biomass aerosols during SCAR-B, *J. Appl. Meteor.*, in press.

Chu, D.A., Y.J. kaufman, L.A. Remer, and B.N. Holben, 1998: Remote sensing of smoke from MODIS airborne simulator during the SCAR-B experiment, J. Geophys. Res., 103, D24, 31,979-31,988

Crutzen,P.J., L.E. Heidt, J.P. Kransec, W.H. Pollack, and W. Seiler, 1979: Biomass burning as a source of atmospheric gases CO, H_2 N_2, CH_3Cl, and COS, *Nature*, 282, 253-256

Dubovik, O., B. N. Holben, Y. J. Kaufman, M. Yamasoe, A. Smirnov, D. Tanre, and I. Slutsker, 1998: Single-scattering albedo of smoke retrieved from the sky radiance and solar transmittance measured from ground, *J. Geophys. Res.*, 103, 31,903-31,923

Eck, T.F., B. N. Holben, I. Slutsker, and A. Setzer, 1998: Measurements of irradiance attenuation and estimation of aerosol single scattering albedo for biomass burning aerosols in Amazonia, *J. Geophys. Res.* 103, 31,865-31,878

Fu, Q., and K.N. Liou, 1992: On the Correlated k-Distribution Method for Radiative Transfer in Nonhomogeneous Atmospheres, *J. of Applied Meteor.*, 49, No.22, 2,139-2,156

Fu, Q., and K.N. Liou, 1993: Parameterization of the radiative properties of cirrus clouds. *J. Atmos. Sci.*, 50, 2,008-2,025

Gautier, C., and M. Landsfeld, 1997: Surface solar radiation flux and cloud radiative forcing for the atmospheric radiation measurement (ARM) Southern Great Plains (SGP): a satellite, surface observations, and radiative transfer model study, *J. Atmos. Sci.*, 54, 1,289-1,307

Gilgen, H., C.H. Whitlock, F. Koch, G. Mueller, A. Ohmura, D. Steiger, and R. Wheeler, 1993: Technical plan for Baseline Surface Radiation Network (BSRN) data management, *World Climate Research Program*, WMO/TD 443, 49pp.

Green, R.N., 1987: Earth Radiation Budget Experiment (ERBE) Data Management System Processed Archival Tape S-8 PAT users's guide, NASA Langley Research Center

Green, R.N., B.A. Wielicki, J.A. Coakley III, L.L. Stowe, and P.O'R. Hinton, 1995: Clouds and the Earth's Radiant Energy System(CERES) Algorithm Theoretical Basis Document, Subsystem 4.5, *NASA reference Publication* 1376, Vol.III

Green, R.N., and B.A. Wielicki, 1995: Clouds and the Earth's Radiant Energy System(CERES) Algorithm Theoretical Basis Document, Subsystem 4.4, *NASA reference Publication* 1376, Vol.III

Hao, W. M., and M-H. Liu, 1994: Spatial and temporal distribution of biomass burning, *Global Biogeochemical Cycles*, 8, 495-503

Hartmann, D.L., V. Ramanathan, A. Berroir, and G.E. Hunt, 1986: Earth radiation budget data and climate research, *Rev. Geophys.*, 24, 439-468

Herman, J.R., P.K. Bhartia, O. Torres, C. Hsu, C. Seftor, and E. Celarier, 1997: Global distribution of UV-absorbing aerosols from Nimbus 7/TOMS data, *J. Geophys. Res.*, 102, 16,911-16,922

Hobbs, P.V., 1996: Overview of measurements obtained aboard the University of Washington's Convair C-131 research aircraft in the Smoke, Clouds And Radiation-Brazil (SCAR-B) project, *Proceedings Smoke/Sulfate, Clouds and Radiation-Brazil (SCAR-B)*, Fortaleza, Brazil, 4-8 November

Hobbs, P. V., J. S. Reid, R. A. Kotchenruther, R. J. Ferek, and R. Weiss, 1997: Optical parameters for smoke particles in Brazil and the direct radiative forcing of climate by smoke from biomass burning, *Science*, 275, 1,776-1,778.

Holben, B.N., A. Setzer, T. F. Eck, A. Pereira, and I. Slutsker, 1996: Effect of dry-season biomass burning on Amazon basin aerosol concentrations and optical properties, 1992-1994. *J. Geophys. Res.*, 101, 19,465-19,481

Holben, B.N., T.F. Eck, I. Slutsker, D. Tanre, J.P. Buis, A. Setzer, E. Vermote, J.A. Reagan, Y.J. Kaufman, T. Nakajima, F. Lavenu, I. Jankowiak, and A. Smirnov, 1998: AERONET-A federated instrument network and data archive for aerosol characterization, *Rem. Sens. of the Environ.*, 66, 1-16

Hsu, N.C., J.R. Herman, P.K. Bhartia, C.J. Seftor, O, Torres, A.M. Thompson, J.F. Gleason, T.F. Eck, and B.N. Holben, 1996: Detection of biomass burning smoke from TOMS measurements, *Geophys. Res. Lett.* 23, 745-748

Husar, R.B., J.M. Prospero, and L.L. Stowe, 1997: Characterization of tropospheric aerosols over the oceans with the NOAA advanced very high resolution radiometer optical thickness operational product, *J. Geophys. Res.*, 102, 16,889-16,909

Inoue, T., 1989: On the temperature and effective emissivity determination of semi-transparent cirrus clouds by bi-spectral measurements in the 10 μm window region, *J. Meteoro. Soc. of Japan*, 63, No.1, 621-637

Intergovernmental Panel on Climate Change (IPCC) 1995: *Climate Change 1995*, Cambridge University Press

Kaufman, Y.J., 1987: Satellite sensing of aerosol absorption, *J. Geophys. Res.*, 92, NO.D4, 4,307-4,317

Kaufman, Y.J., and C. Sendra, 1988: Algorithm for automatic atmospheric corrections to visible and near-IR satellite imagery, *Int. J. Remote Sens.*, 9, 1,357-1,381

Kaufman, Y. J., A. Setzer, D. Ward, D. Tanre, B. N. Holben, P. Menzel, M. C. Pereira, and R. Rasmussen, 1992: Biomass burning airborne and spaceborne experiment in the Amazonas(BASE-A), *J. Geophys. Res.* 97, 14,581-14,599

Kaufman, Y. J., and T. Nakajima, 1993: Effect of Amazon smoke on cloud microphysics and albedo – Analysis from satellite imagery, *J. Appl. Meteorol.*, 32, 729-744

Kaufman, Y.J., P.V. Hobbs, V.W.J.H. Kirchhoff, P. Artaxo, L.A. Remer, B.N. Holben, M.D. King, D.E. Ward, E.M. Prins, K.M. Longo, L.F. Mattos, C.A. Nobre, J.D. Spinhirne, Q. Ji, A.M. Thompson, J.F. Gleason, S.A. Christopher, and S.C. Tsay, 1998: Smoke, Clouds, and Radiation-Brazil(SCAR-B) experiment, *J. Geophys. Res.* 103, 31,783-31,808

Keiffer, H. H, and R. L. Wildey, 1996: Establishing the moon as aspectral radiance standard. *J. Atmos. Oceanic Technol.*, 13, 360-375

Kidwell, K.B., 1998: NOAA polar orbiter data (TIROS-N, NOAA-6, NOAA-7, NOAA-8, NOAA-9, NOAA-10, NOAA-11, NOAA-12, NOAA-13 and NOAA-14) user's guide

Kneizys, F.X., E.P. Shettle, W.O. Gallery, J.H. Chetwynd, L.W. Abreu, J.E.A. Selby, S.A. Clough, and R.W. Fenn, 1983: Atmospheric transmittance/radiance: Computer code LOWTRAN 6, Rep. AFGL-TR-83-0187, 200pp (available from Air Force Geophysical Laboratory, Hanscom Air Force base, MA 01731)

Konzelmann, T., D.R. Cahoon, and C.H. Whitlock, 1996: Inapt of biomass burning in equatorial Africa on the downward surface shortwave irradiance: Observations versus calculations. *J. Geophys. Res.*, 101, 22,833-22,844

Kotchenruther, R.A., and P. V. Hobbs, 1998: Humidification factors of aerosols from biomass burning in Brazil, *J. Geophys. Res.*, 103, 32,081-32,089

Kummerow, C., W. Barnes, T. Kozu, J. Shuie, and J. Simpson, 1998: TheTropical Rainfall Measring Mission (TRMM) Sensor package. *J. Atmos.Oceanic Tech.*, 15, 809-817

Lenoble, J, 1991: The particulate matter from biomass burning: A tutorial and critical review of its radiative impact. *Global biomass burning*, 381-386, Ed. J.S. Levine

Li, X., S.A. Christopher, J. Zhang, J. Chou, and R. M. Welch, 1999a: Aerosol single scattering albedo estimated from NOAA-14 AVHRR measurements: Case studies over Brazil, *Proceedings of SPIE*, Denver, CO July 18-23

Li, Z., and H.G. Leighton, 1991: Scene identification and its effect on cloud radiative forcing in the arctic, *J. Geophys. Res.*, 96, 9,175-9,188

Li, Z, H.G. Leighton, K. Masuda, and T. Takashima, 1993: Estimation of SW flux absorbed at the surface from TOA reflected flux, *J. Climate,* 317-330

Li, Z, C.H. Whitlock, T.P. Charlock, 1995: Assesment of the gloal monthly mean surface insolation estimated from satellite measurements using Global Energy Balance Archive data, *J. Climate*, 8, 315-328

Li, Z, 1998: Influence of absorbing aerosols on the inference of solar surface radiation budget and cloud absorption, *J. Climate*, 11, 5-17

Liao, H., and J. H. Seinfeld, 1998: Radiative forcing by mineral dust aerosols: sensitivity to key variables, *J. Geophys. Res.,* 103, D24, 31,637-31,645

Liou, K.N., 1980: An introduction to atmospheric radiation, Academic Press, 392pp

Liou, K.N., Q. Fu, and T.P. Ackerman, 1988: A simple formulation of the d-four-stream approximation for radiative transfer parameterizations, *J. Atmos. Sci.*, 45, 1,940-1,947

Liousse, C., F. Dulac, and H. Cachier, 1997: Remote sensing of carbonaceous aerosol production by African savanna biomass burning, *J. Geophys. Res.* 102, 5,895-5,911

Martins, J.V., P. Artaxo, C. Liousse, J. S. Reid, P. V. Hobbs, and Y. J. Kaufman, 1998: Effects of black carbon content, particle size, and mixing on light absorption by aerosols from biomass burning in Brazil, *J. Geophys. Res.* 103, 32,041-32,050

McClatchey, R.A., R.W. Fenn, J.E.A. Selby, F.E. Volz, J.S. Garing, 1972: Optical properties of the atmosphere, *Air Force Cambridge Research Laboratories Report* AFCRL-72-0497.

Minnis, P., E.F. Harrison, L.L. Stowe, G.G. Gibson, F.M. Denn, D.R. Doelling, and W.L. Smith Jr., 1993: Radiative climate forcing by the Mount Pinatubo eruption, *Science*, 259, 1,411-1,415

Minnis, P., W.L. Smith Jr., D.P. Garber, J.K. Ayers, and D.R. Doelling, 1995: Cloud properties derived from GOES-7 for spring 1994 ARM Intensive Observing Period using Version 1.0.0 of ARM satellite data analysis program, *NASA. Ref. Publ.* 1366, 58pp

Penndorf, R., 1957: Tables of the refractive index for standard air and the Rayleigh scattering coefficient for the spectral region between 0.2 and 20 μm and their application to atmospheric optics, *J. Opt. Soc. Amer.*, 47, 176-182

Penner, J.E., R.E. Dickinson, and C.A. O'Neill, 1992: Effects of aerosol from biomass burning on the global radiation budget. *Science*, 256, 1,432-1,434

Pierluissi, J.H., and C.E. Maragoudakis, 1986: Molecular transmission band models for LOWTRAN, *AFGL-TR-86-0272*, AD A180655

Pinker, R.T. and I. Laszlo, 1992: Modeling surface solar irradiance for satellite applications on a global scale. *J. Applied Meteor*, 31, 194-211

Prins, E.M. and W.P. Menzel, 1992: Geostationary satellite detection of biomass burning in South America, *Int. J. Rem. Sens.*, 13, 2,783-2,799

Prins, E.M., and W.P. Menzel, 1996a: Monitoring biomass burning and aerosol loading and transport from a geostationary satellite perspective, *Seventh Symposium on Global change Studies, Am. Meteorol. Soc.*, Atlanta, Ga.

Prins, E.M., and W.P. Menzel, Investigation of biomass burning and aerosol loading and transport utilizing geostationary satellite data, *in Biomass Burning and Global Change*, edited by J.S. Levine, pp 65-72, MIT Press, Cambridge, Mass.

Prins, E. M., J. M. Feltz, W. P. Menzel, D. E. Ward, 1998: An overview of GOES-8 diurnal fire and smoke results for SCAR-B and the 1995 fire season in South America, *J. Geophys. Res.*, 103, D24, 31,821-31,835

Ramanathan, V., R.D. Cess, E.F. Harrison, P. Minnis, B.R. Barkstrom, E. Ahmad, and D. Hartmann, 1989: Cloud radiative forcing and climate: results from the Earth Radiation Budget Experiment, *Science,* 243, 57-63

Rao, C.R.N., and J. Chen, 1996: Post-launch calibration of the visible and near-infrared channels of the Advanced Very High Resolution Radiometer (AVHRR) on the NOAA-14 spacecraft, *Int. J. Remote Sens.* 17, 2,743-2,747

Rao, C.R.N., and J. Chen, 1999: Revised post-launch calibration of the visible and near-infrared channels of the Advanced Very High Resolution Radiometer (AVHRR) on the NOAA-14 spacecraft, *Int. J. Remote Sens.* 20, 3,485-3,491

Reid, J.S., and P. V. Hobbs, 1998a: Physical and optical properties of young smoke from individual biomass fires in Brazil, *J. Geophys. Res.* 103, 32,013-32,030

Reid, J.S., P. V. Hobbs, R. J. Ferek, D. R. Blake, J. V. Martins, M. R. Dunlap, and C. Liousse, 1998b: Physical, chemical, and optical properties of regional hazes dominated by smoke in Brazil, *J. Geophys. Res.* 103, 32,059-32,080

Reid, J. S., P. V. Hobbs, C. Liousse, J. V. Martins, R. E. Weiss, and T. F. Eck, 1998c: Comparisons of techniques for measuring shortwave absorption and black carbon content of aerosols from biomass burning in Brazil, *J. Geophys. Res.* 103, 32,031-32,040

Reid, J.S., T.F. Eck, S.A. Christopher, P.V. Hobbs, B.R. Holben, 1999: Use of the Angstrom exponent to estimate the variability of optical and physical properties of aging smoke particles in Brazil, *J. Geophys. Res.,* 104, 27,473-27,489

Remer, L.A., Y. J. Kaufman, B. N. Holben, A. M. Thompson, and D. McNamara, 1998: Biomass burning aerosol size distribution and modeled optical properties, *J. Geophys. Res.*, 103, 31,879-31,891

Ricchiazzi, P., and C. Gautier, 1995: Cloud scattering optical depth and local surface albedo in the antarctic: simultaneous retrieval using ground-based radiometry, *J. Geophys. Res.*, 100, 21,091-21,104

Ricchiazzi, P. J., S. Yang, C. Gautier, and D. Sowle, 1998: SBDART: A practical tool for plane-parallel radiative transfer in the Earth's atmosphere, *Bull. Amer. Meteorol. Soc.* 79, 2,101-2,114

Roberts, R.E., J.E.A. Selby, and L.M. Biberman, 1976: Infrared continuum absorption by atmospheric water vapor in the 8-12 mm window, *Appl. Opt.,* 15, 2,085-2,090

Ross, J.L., P. V. Hobbs, and B. Holben, 1998: Radiative characteristics of regional hazes dominated by smoke from biomass burning in Brazil: Closure tests and direct radiative forcing, *J. Geophys. Res.,* 103, 31,925-31,941

Sailer, W., and P.J. Crutzen, 1980: Estimates of gross and net fluxes of carbon between the biosphere and atmosphere from biomass burning, *Climate Change*, 2, 207-247

Stamnes, K., S. Tsay, W. Wiscombe, and K. Jayaweera, 1988: Numerically stable algorithm for discrete-ordinate-method radiative transfer in multiple scattering and emitting layered media, *Appl. Opt.,* 27, 2,502-2,509

Stowe, L.L., and A.M. Ignatov, 1997: Development, validation, and potential enhancements to the second-generation operational aerosol product at the National Environmental Satellite,Data, and Information Service of the National Oceanic and Atmospheric Administration, *J. Geophys. Res.*, 102, 16,923-16,934

Suttles, J.T., R.N. Green, P. Minnis, G.L. Smith, W.F. Staylor, B.A. Wielicki, I.J.Walker, D.F. Young, V.R. Taylor, and L.L. Stowe, 1988: Angluar Radiation Models for Earth-Atmosphere System. I-Shortwave Radiation. *NASA RP-1184*

Suttles, J.T., R.N. Green, G.L. Smith, B.A. Wielicki, I.J.Walker, V.R. Taylor, and L.L. Stowe, 1989: Angluar Radiation Models for Earth-Atmosphere System. II-longwave Radiation. *NASA RP-1184*

Suttles, J.T., B.A. Wielicki, and V. Sastri, 1992: Top-of-Atmosphere radiative fluxes – validation of ERBE scanner inversion algorithm using Nimbus-7 ERB data, *J. Appl. Meteorol.*, 31, 784-796

Ward D.E., and C.C. Hardy, 1991: Smoke emissions from wildland fires, *Environ. Intern.*, 17, 117-134

Whitlock, C.H., T.P. Charlock, W.F. Staylor, R.T. Pinker, I. Laszlo, R.C. DiPasquale, and N.A. Ritchey, 1993: WCRP surface radiation budget shortwave data product description - version 1.1, *NASA Technical Memorandum* 107747.

Whitlock, C. H., T.P. Charlock, W.F. Staylor, R.T. Pinker, I. Laszlo, A. Ohmura, H. Gilgen, T. Konzelman, R.C. DiPasquale, C.D. Moats, S.R. LeCroy, and N.A. Ritchey, 1995: First global WCRP shortwave surface radiation budget data set, *Bull. Amer. Meteorol. Soc.*, 76, 905-922

Wielicki, B.A., R.N. Green, C.J. Tolson, and A. Fan, 1995: *Clouds and the Earth's Radiant Energy System(CERES) Algorithm Theoretical Basis Document, Subsystem 4.0*

Wielicki, B. A., B. R. Barkstrom, E. F. Harrison, R.B. Lee III, G. L. Smith and J. E. Cooper, 1996: Clouds and the Earth's Radiant Energy System (CERES): An Earth Observing System Experiment, *Bull. Amer. Meteor. Soc.*, 77, 853-868

Wiscombe, W.J., J.W. Evans, 1977: Exponential-sum fitting of radiative transmission functions, *J. Comp. Physics*, 24, 416-24,444

Zhang, Y.-C., and W.B. Rossow, 1995: Calculation of surface and top of atmosphere radiative fluxes from physical quantities based on ISCCP data sets, 1. Methods and sensitivity to input data uncertainties, *J. Geophys. Res.*, 100, 1,149-1,165

APPENDIX A

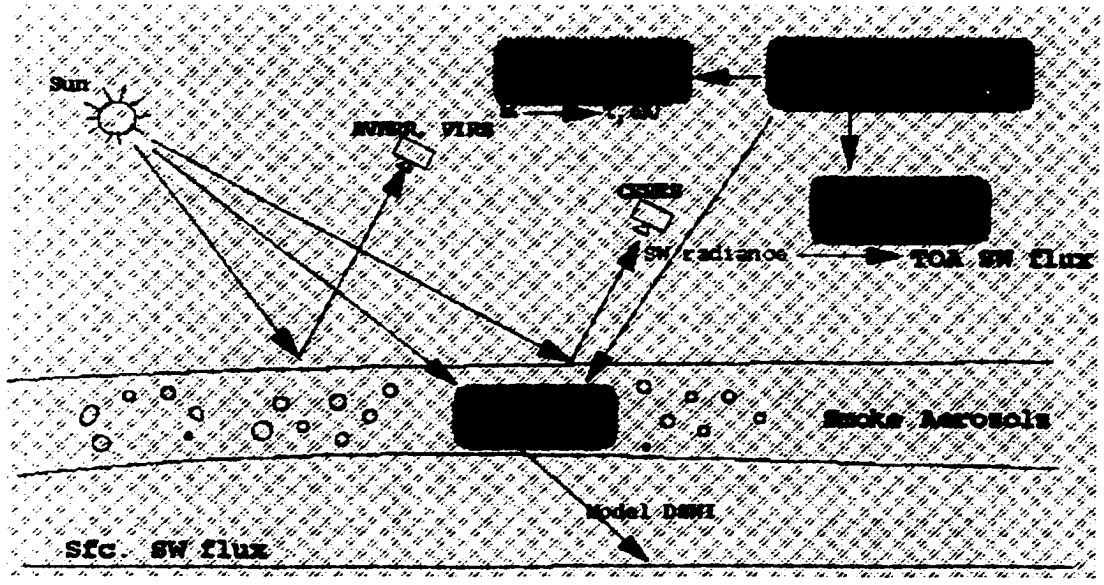

Figure A.1 Schematic diagram showing the objectives and models used in this research work. Mie model is used to calculate wavelength-dependent optical properties of smoke aerosols. SBDART model is used to produce a table look-up table for the satellite retrieval of smoke optical properties. SBDART model is also used to produce Angular Distribution Model for smoke aerosols which then is used to convert CERES SW radiances to CERES SW fluxes for smoke aerosols. 4-stream model is used to calculate surface downward SW irradiances at smoke condition.

Appendix B

When solar radiation propagates through an aerosol layer and interacts with aerosol particles, some amount of incident solar energy will be removed from its path due to the scattering and absorption effects of aerosols. For a single spherical aerosol particle with known refractive index, the extinction cross section (σ_{ext}) and scattering cross section (σ_{sca}) of the aerosol can be calculated using Mie theory (Liou 1980). Then, the extinction efficiency (Q_{ext}) and scattering efficiency (Q_{sca}) of the particle are defined as:

$$Q_{ext} = \frac{\sigma_{ext}}{\pi a^2}, \qquad \text{A.1}$$

and

$$Q_{sca} = \frac{\sigma_{sca}}{\pi a^2}, \qquad \text{A.2}$$

where a is the radius of the aerosol particle. The refractive index, extinction efficiency and scattering efficiency are wavelength dependent.

The extinction and scattering effects for a number of aerosol particles can be characterized by the bulk optical properties such as extinction coefficient (β_{ext}) and scattering coefficient (β_{sca}) given aerosol size distribution. β_{ext} and β_{sca}

at some wavelength λ, are defined as:

$$\beta_{ext,\lambda} = \int_0^{\infty} n(r)\pi r^2 Q_{ext}\, dr, \qquad \text{A.3}$$

and

$$\beta_{sca,\lambda} = \int_0^{\infty} n(r)\pi r^2 Q_{sca}\, dr, \qquad \text{A.4}$$

where n(r) is the particle size distribution and r is the radius of particles. These equations show how the bulk extinction and scattering coefficients are related to the extinction and scattering efficiencies for a single particle derived from the Mie theory.

The column aerosol optical thickness, τ, is then defined as the vertical integral of β_{ext} (Liou 1980):

$$\tau_{\lambda} = \int_0^{\infty} \beta_{ext,\lambda}\, dz \qquad \text{A.5}$$

The single scattering albedo, ω_0, which represents the percentage of radiation that will under go scattering in a single scattering event, is then defined as (Liou 1980):

$$\omega_{0,\lambda} = \frac{\beta_{sca,\lambda}}{\beta_{ext,\lambda}} \qquad \text{A.6}$$